Appendix D

Structural Analyses

Appendix D Abstract

The seals for the shafts at the WIPP are comprised of columns of compacted earthen fill, compacted clay, asphalt, and compacted crushed salt, separated by concrete seals. The structural behavior of these columns and the concrete components is the primary focus of the calculations presented in this appendix. The development (and subsequent healing) of the disturbed rock zone that forms in the rock mass surrounding the shafts is a significant concern in the seal design, and these issues are also addressed in this appendix. In addition, several structural calculations are included that were used as input to the hydrological calculations reported in Section 8 and Appendix C. Complexity of the calculations ranged from solving a simple equation to rigorous finite-element modeling encompassing both thermal and structural elements.

Page intentionally blank.

Contents

D1. INTRODUCTION 7
D2. ANALYSES METHODS 8
  D2.1 SPECTROM-32 9
  D2.2 SPECTROM-41 9
  D2.3. SALT_SUBSID 10
D3. MATERIAL CHARACTERIZATION 10
  D3.1 Shaft Seal Components 10
    D3.1.1 Salado Mass Concrete 10
    D3.1.2 Crushed Salt 14
    D3.1.3 Compacted Clay 19
    D3.1.4 Asphalt 19
  D3.2 In Situ Materials 21
    D3.2.1 Salado Salt 21
    D3.2.2 Salado Anhydrite and Polyhalite 26
    D3.2.3 Near Surface and Rustler Formations 28
  D3.3 Models for the Disturbed Rock Zone within Salt 29
    D3.3.1 Stress-Invariant Criterion 29
    D3.3.2 Damage-Stress Criterion 30
    D3.3.3 Evaluation of DRZ Models 30
D4. SHAFT SEAL COMPONENT ANALYSES 33
  D4.1 Salado Mass Concrete Seals 33
    D4.1.1 Thermal Analysis of Concrete Seals 33
    D4.1.2 Structural Analysis of Concrete Seals 33
    D4.1.3 Thermal Stress Analysis of Concrete Seals 42
    D4.1.4 Effect of Dynamic Compaction on Concrete Seals 43
    D4.1.5 Effect of Clay Swelling Pressures on Concrete Seals 44
  D4.2 Crushed Salt Seal 44
    D4.2.1 Structural Analysis of Crushed Salt Seal 44
    D4.2.2 Effect of Fluid Pressure on the Reconsolidation of Crushed Salt Seals 47
  D4.3 Compacted Clay Seals 51
    D4.3.1 Structural Analysis of Compacted Clay Seals 51
  D4.4 Asphalt Seals 51
    D4.4.1 Thermal Analysis of Asphalt Seals 51
    D4.4.2 Structural Analysis of Asphalt Seals 54
    D4.4.3 Shrinkage Analysis of Asphalt Seals 54
D5. DISTURBED ROCK ZONE CONSIDERATIONS 59
  D5.1 General Discussion 59
    D5.1.1 Salt Damage Models 60
    D5.1.2 Salt Healing Models 60
  D5.2 Disturbed Rock Zone Analyses 62
    D5.2.1 Analysis of the Disturbed Rock Zone in Salado Salt 62
    D5.2.2 Salado Anhydrite Beds 70

D5.2.3 Near Surface and Rustler Formations 73
D6. OTHER ANALYSES 74
D6.1 Asphalt Waterstops 74
D6.2 Shaft Pillar Backfilling 76
D7. REFERENCES 83

Figures

Figure D-1. Heat generation of Salado Mass Concrete mixture. 12
Figure D-2. Comparison of calculated results using damage-stress and stress-invariant DRZ models with measured AIS results. 32
Figure D-3. Axisymmetric model used in the SMC thermal analysis. 34
Figure D-4. Temperature histories of SMC center and SMC/salt interface. 35
Figure D-5. Isotherms surrounding SMC seal at 0.02 year. 36
Figure D-6. Seal system conceptual design for the WIPP air intake shaft. 38
Figure D-7. Axisymmetric model configuration of upper concrete shaft seal. 39
Figure D-8. Axisymmetric model configuration of middle concrete shaft seal. 40
Figure D-9. Axisymmetric model configuration of lower concrete shaft seal. 41
Figure D-10. Swelling pressures as a function of time for a brine-saturated bentonite specimen with a density of 1,800 kg/m^3. 45
Figure D-11. "Pineapple slice" axisymmetric models. 46
Figure D-12. Consolidation of crushed salt in a shaft at depths of 430, 515, and 600 m using the modified Sjaardema-Krieg, Spiers, and Zeuch models. 48
Figure D-13. Crushed-salt fractional density as a function of time for a fluid pressure of 2 MPa and using the modified Sjaardema-Krieg creep consolidation model. 50
Figure D-14. WIPP shaft seal design showing asphalt components. 52
Figure D-15. Models used in thermal analysis of asphalt seal. 53
Figure D-16. Temperature histories in asphalt (Point A, Figure D-15a) and salt (Point B, Figure D-15a). 55
Figure D-17. Comparison of asphalt center temperatures for different waterstop configurations. 56
Figure D-18. Pressure buildup in the upper, middle, and lower shaft seal waterstops. 57
Figure D-19. Normalized DRZ radius as a function of shaft seal stiffness at various depths within the Salado Formation at time = 0 year after emplacement. 64
Figure D-20. Normalized DRZ radius as a function of shaft seal stiffness at various depths within the Salado Formation at time = 10 years after emplacement. 65
Figure D-21. Normalized DRZ radius as a function of shaft seal stiffness at various depths within the Salado Formation at time = 25 years after emplacement. 66
Figure D-22. Normalized DRZ radius as a function of shaft seal stiffness at various depths within the Salado Formation at time = 50 years after emplacement. 67
Figure D-23. Normalized DRZ radius as a function of shaft seal stiffness at various depths within the Salado Formation at time = 100 years after emplacement. 68
Figure D-24. Factor of safety in polyhalite beds at 50 years. 71

Figure D-25. Factor of safety in anhydrite beds at 50 years. 72
Figure D-26. Normalized DRZ radius for strength reduction factor of 4 and horizontal stress factor of 1.5. 75
Figure D-27. Salt DRZ around the lower shaft seal at 50 years (prior to seal construction). 77
Figure D-28. Salt DRZ around the lower shaft seal at 50.1 years (after excavations but before seal construction). 78
Figure D-29. Salt DRZ around the lower shaft seal at 20 years after seal construction. 79
Figure D-30. Mining blocks used to represent WIPP underground workings. 81
Figure D-31. Surface subsidence profiles over shaft area 82

Tables

Table D-1. Salado Mass Concrete Thermal Properties 11
Table D-2. Heat of Hydration Model Parameters 13
Table D-3. Summary of Creep Data (from Wakeley et al., 1994) 13
Table D-4. Variation of Elastic Modulus of SMC as a Function of Time (from Wakeley et al., 1994) 13
Table D-5. Nonlinear Elastic Material Parameters for WIPP Crushed Salt 15
Table D-6. Creep Consolidation Parameters for Crushed Salt (after Sjaardema and Krieg, 1987) 16
Table D-7. Revised Sjaardema-Krieg, Zeuch, and Spiers Creep Consolidation Parameter Values 18
Table D-8. Nonlinear Elastic Material Parameters for Compacted Clay 20
Table D-9. Asphalt Thermal Properties 20
Table D-10. Asphalt Elastic Properties 20
Table D-11. Salado Salt Thermal Properties 21
Table D-12. Munson-Dawson Parameter Values for Argillaceous Salt (after Munson et al., 1989) 27
Table D-13. Damage Model Parameters for Argillaceous Salt 28
Table D-14. Anhydrite and Polyhalite Elastic and Drucker-Prager Parameter Values 28
Table D-15. Rock Types and Properties 29
Table D-16. Normalized DRZ Radius Surrounding the AIS 30
Table D-17. Initial Temperature and Stress Conditions within Salado Formation 42
Table D-18. Normalized DRZ Radius—Concrete 69
Table D-19. Normalized DRZ Radius—Crushed Salt 69
Table D-20. Normalized DRZ Radius—Compacted Clay 69
Table D-21. Normalized DRZ Radius—Asphalt 70

M

Page intentionally blank.

D1. INTRODUCTION

The seals for the shafts at the WIPP are comprised of columns of compacted earthen fill, compacted clay, asphalt, and compacted crushed salt, separated by concrete seals. Within the Salado Formation each shaft seal includes: (1) an asphalt column extending from above the Rustler/ Salado interface down into the Salado salt, (2) an upper Salado compacted clay column, (3) a long compacted crushed salt column, and (4) a lower Salado compacted clay column. Each of these columns is separated by specially designed salt-saturated concrete components. The structural behavior of the various columns and the concrete components is the initial focus of the calculations presented in this appendix.

The development (and subsequent healing) of a disturbed rock zone (DRZ) that forms in the rock mass surrounding the WIPP shafts is a significant concern in the seal design. It is well known that an initial DRZ will develop in the rock adjacent to the shaft immediately after excavation. Moreover, the DRZ within the Salado Formation continues to develop because of salt creep. Shaft seal emplacement will cause the DRZ to heal with time because of restraint to creep closure by the seal materials and the subsequent reduction in the stress differences in the surrounding intact salt. Within the formations above the Salado, the DRZ is assumed to be time-invariant, since the behavior of the rock masses encountered there is predominantly elastic. The calculation of the temporal and spatial extent of the DRZ along the entire shaft length is the second focus of this appendix.

This appendix provides a collection of calculations pertaining to the above mentioned structural concerns. The purpose of each calculation varied; however, the calculations generally addressed one or more of the following issues (1) stability of the component, (2) influences of the component on hydrological properties of the seal and surrounding rock, or (3) construction issues. Stability issues that were addressed in these calculations included:

- potential for thermal cracking of concrete seals, and.
- structural failure of concrete seal components because of loads resulting from (1) creep of surrounding salt, (2) dynamic compaction and gravity loads of overlying seal material, (3) repository generated gas pressures, and (4) clay swelling pressures.

Structural calculations were also used to define input conditions to the hydrological calculations reported in Section 8, including:

- spatial extent of the DRZ within the Salado Formation surrounding the shafts as a function of depth, time, and seal material type,
- fracturing and DRZ development within Salado Formation interbeds,
- compacted-salt fractional density as a function of depth and time,
- shaft-closure induced consolidation of compacted-salt seals, and
- impact of pore pressures on consolidation of compacted-salt seals.

The construction issues that were addressed included:

- emplacement and structural performance of asphalt waterstops, and
- potential benefits from backfilling shaft stations.

Complexity of the calculations ranged from solving a simple equation to rigorous finite-element modeling encompassing both thermal and structural elements. All calculations are presented in a similar format, having approximately the same detail. Each calculation is described in terms of its objectives, problem statement, assumptions, and results.

Calculations were performed concurrently with development of the shaft seal design. Consequently, in some instances calculations reported here do not exactly match particular component dimensions shown in the design drawings (Appendix E) because of later changes in the design. Conclusions drawn from the results of these earlier calculation would not, however, change simply because of dimensional changes or emplacement conditions. In some instances a single calculation (e.g., a finite-element analysis of the concrete seal) was used to evaluate the structural behavior of more than one seal component. For example, the finite-element analysis of the asphalt waterstops was used to calculate both the DRZ development in the Salado salt and the time-dependent stresses in the concrete seals. Additionally, some results are drawn from previous similar analyses that are still generally applicable to the current design.

For convenience, the presentation of structural analyses in this appendix is divided into five sections, describing:

- analyses methods,
- material models,
- structural behavior of the shaft seal components,
- DRZ development (and healing) in intact rock surrounding the shaft, and
- analyses related to construction issues.

More specifically, analyses methods and computer programs used in performing these analyses are presented in Section D2. The analyses methods include finite element modeling and analytical techniques. Section D3 describes the models used in characterizing material behavior of shaft seal components, the intact rock mass, and the DRZ. Material models included thermal properties, deformational behavior, and strength properties for the four shaft seal materials and the in situ materials. Also included is a description of the models used to characterize the DRZ. A summary of the structural analyses of the four shaft seal materials is presented in Section D4. Analyses of the shaft seal components are presented by material type, i.e., concrete, compacted crushed salt, compacted clay, and asphalt. The behavior of the DRZ within the intact rock mass surrounding the shaft is described in Section D5. The DRZ was evaluated within Salado salt, Salado interbeds, and overlying nonsalt formations. Finally, analyses of asphalt waterstops and shaft station backfilling are discussed in Section D6.

D2. ANALYSES METHODS

Finite-element modeling and subsidence modeling were the primary methodologies used in evaluating the structural performance of the shaft seals and the surrounding intact rock mass. The finite element programs SPECTROM-32 and SPECTROM-41 were used in the structural and thermal calculations, respectively. The program SALT_SUBSID was used in the subsidence modeling. These programs are described below.

D2.1 SPECTROM-32

The finite-element structural modeling program SPECTROM-32 (Callahan, 1994) was used in performing structural calculations. These calculations included creep deformation of the host rock, consolidation of shaft seal material, and development (and subsequent healing) of the DRZ within salt. This thermomechanical program was designed specifically for simulation of underground openings and structures. SPECTROM-32 has the capability to model the elastic-plastic response, commonly associated with brittle rock types, and has been used extensively to simulate the time-dependent viscoplastic behavior observed in intact salt. In addition, creep consolidation material behavior (e.g., crushed salt) can be modeled using SPECTROM-32. Specific features and capabilities of SPECTROM-32 required for numerical simulations include:

- capabilities for plane-strain and axisymmetric geometries,
- kinematic and traction boundary conditions,
- Multimechanism Deformation Coupled Fracture (MDCF) (Chan, 1993) constitutive model for modeling creep behavior of salt and estimating the DRZ in salt,
- creep consolidation models for time-dependent densification of crushed salt,
- nonlinear elastic behavior for modeling time-independent deformational behavior of crushed salt and compacted clay,
- capability to represent arbitrary in situ stress and temperature fields, and
- capability to simulate shaft excavation and seal material emplacements.

Most of the structural analyses were performed using Version 4.06 of this program. Analyses using recently developed creep consolidation models and for calculating the effects of pore pressure on consolidation of crushed-salt seal were performed using Version 4.08 of the program.

D2.2 SPECTROM-41

The finite-element program SPECTROM-41 (Svalstad, 1989) was used in performing thermal calculations. This program has been designed and used to solve heat transfer problems resulting from the storage of heat-generating material in geologic formations for the past 15 years. The program has been documented to satisfy the requirements and guidelines outlined in NUREG-0856 (Silling, 1983). Specific features and capabilities of SPECTROM-41 that were required for the numerical simulations include:

- capabilities for two-dimensional and axisymmetric geometries,
- multimaterial behavior,
- specified initial temperature conditions,
- specified temperature or flux boundary conditions,
- temperature-dependent thermal properties,
- time-dependent volumetric heat generation, and
- transient and/or steady-state solutions.

D2.3. SALT_SUBSID

SALT_SUBSID (Nieland, 1991) is a PC-based subsidence modeling software used to evaluate surface subsidence over underground openings in salt. The computer program has the capability of developing a site-specific subsidence model which can be used for predicting the future subsidence over a new or existing mining plan. The computer program can also predict stresses and strains along the shaft height resulting from subsidence. Subsidence calculations can be performed on either solution mines or dry mines in salt or potash. The analytical model is based on the solution for ground movement above a closing displacement discontinuity in an isotropic material and includes a time-dependent function to account for the viscoplastic nature of salt. SALT_SUBSID is commercially available software from the Solution Mining Research Institute (SMRI).

D3. MATERIAL CHARACTERIZATION

This section describes models used in characterizing material behavior of the WIPP shaft seal components, intact rock mass, and DRZ. Structural models used to characterize the four shaft seal materials are discussed in Section D3.1. The structural models include thermal properties, deformational behavior, and strength characteristics. Seal materials include concrete, crushed salt, compacted clay, and asphalt. Structural models for intact rock are presented in Section D3.2. These materials include Salado salt, Salado anhydrite and polyhalite, and the rock types encountered in the near-surface and Rustler Formations. Models used in characterizing the DRZ within the intact rock mass surrounding the shaft are presented in Section D3.3.

D3.1 Shaft Seal Components

The shaft seal components include Salado Mass Concrete (SMC), crushed salt, compacted clay, and asphalt. Thermal, deformational, and strength characteristics of these four materials that were required in the structural analyses are given in the following sections.

D3.1.1 Salado Mass Concrete

Thermal, deformational, and strength characteristics of SMC were required in these structural analyses. These properties are discussed in the following subsections.

Thermal Properties. Required thermal properties include thermal conductivity, specific heat, density, and volumetric heat generation rate (Table D-1). Values of thermal conductivity, specific heat, and density are based on laboratory tests performed at Waterways Experimental Station (WES) (Wakeley et al., 1994).

Heat of hydration of SMC is illustrated in Figure D-1 which shows heat generation ($\mathrm{Btu/lb_{cem}}$) as a function of time (hr), where the subscript "cem" refers to the total weight of cementitious material. The curve was digitized and fit to the functional form,

$$Q(t) = Q_\infty \exp\left[-(\tau_e / t)^\alpha\right] \tag{D-1}$$

which was suggested by the Andersen et al. (1992) for describing the heat of hydration for concrete pavements, where Q_∞, τ_e and α are the model parameters and t is time (hr).

These model parameters were determined using the statistical program BMDP/386 and are listed in Table D-2. The volumetric heat generation rate (*dQ/dt*) of the concrete is required in performing the thermal analyses. Differentiating Equation D-1 with respect to time results in:

$$dQ(t)/dt = Q(t)\left(\tau_e/t\right)^{\alpha}\left(\alpha/t\right) \tag{D-2}$$

The conversion of units from Btu/lb$_{cem}$ to W-hr/m$^3_{con}$, where m$^3_{con}$ refers to cubic meters of concrete, is given as follows:

[1 Btu/lb$_{cem}$] [1055 J/Btu] [2.2 lb/kg] [2280 kg/m^3] [1 W-s/J] [1 hr/3600 s] [0.16 lb$_{cem}$/lb$_{con}$]
= 235 W-hr/m$^3_{con}$.

Deformational Properties. SMC is assumed to behave as a viscoelastic material, based on experimental data for several mixes of SMC. The WES (Wakeley et al., 1994) creep data are summarized in Table D-3. An isothermal form of the Norton (power) creep law was fit to long-term laboratory creep-test data and resulted in the following:

$$\dot{\varepsilon}_{ss} = A\sigma^{n} \tag{D-3}$$

where:

$\dot{\varepsilon}_{ss}$ = steady-state strain rate

σ = deviatoric stress

A = fitted model parameter = $0.11(10^{-6})$/day

n = fitted model parameter = 0.54.

Table D-1. Salado Mass Concrete Thermal Properties

Property	**Units**	**Value**
Thermal Conductivity	W/m-K	2.145
Specific Heat	J/kg-K	971.
Density	kg/m^3	2,280
Heat of Hydration Rate	W/m^3	(Equation D-2)

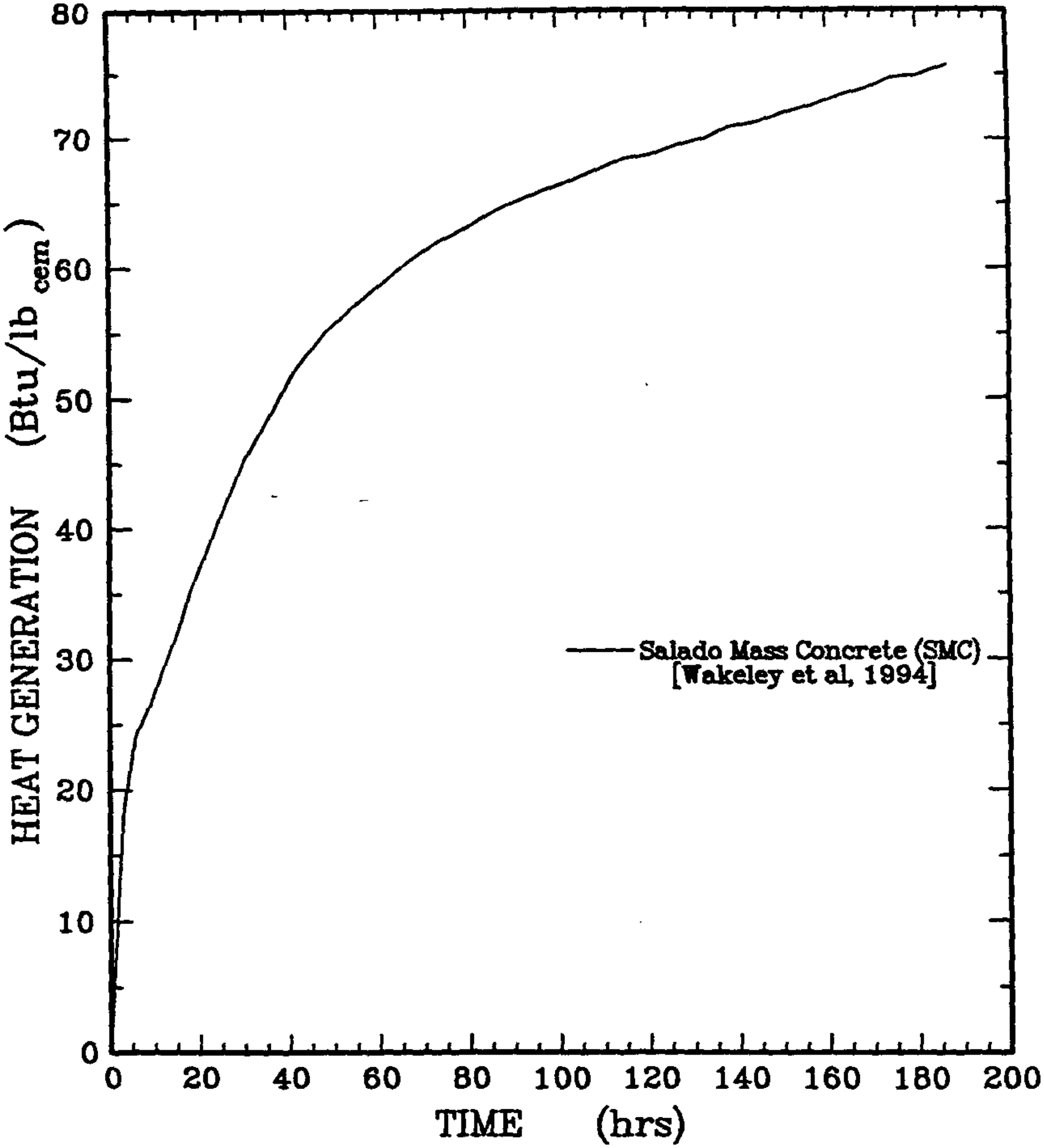

Figure D-1. Heat generation of Salado Mass Concrete mixture.

Table D-2. Heat of Hydration Model Parameters

Parameter	**Units**	**SMC**
Q_∞	$\text{Btu/lb}_{\text{cem}}$ ($\text{W-hr/m}^3{}_{\text{con}}$)	173.7 (40,837)
τ_e	hr	89.8
α	—	0.264

Table D-3. Summary of Creep Data (from Wakeley et al., 1994)

Test Number	**Uniaxial Stress (MPa)**	**Steady-State Strain Rate (10^{-6}/day)**
1	2.5	0.175
2	5.9	0.265
3	7.8	0.333

The elastic modulus of SMC is assumed to be age-dependent, based on experimental data reported by WES (Wakeley et al., 1994). These data are given in Table D-4. A functional form shown in Equation D-4 was used to represent the age-dependence of the elastic modulus of SMC as it sets (increases in stiffness):

$$E(t) = E_{max}\left(\frac{t}{t + t_0}\right) \qquad \text{(D-4)}$$

where:

$E(t)$ = modulus at time t

t = time (days)

$E_{\max}$ = ultimate stiffness.

Table D-4. Variation of Elastic Modulus of SMC as a Function of Time (from Wakeley et al., 1994)

Time (days)	**Elastic Modulus 10^6 (psi)**
0	0
28	4.00
90	5.77
230	6.34

The model parameters derived from experimental results given in Table D-4 are:

$E_{\max} = 6.7\ (10^6)$ psi

$t_0 = 16.75$ days.

Poisson's ratio of SMC was assumed to be 0.19 and is consistent with literature values for concretes. The thermal expansion of SMC is $11.9\ (10^{-6})$/°C based on test data from WES (Wakeley et al., 1994).

Strength Properties. The design specification for concrete is a 28-day unconfined compressive strength of 4,500 psi (31 MPa) (Appendix A). Recent laboratory tests indicate that SMC has an unconfined compressive strength of about 6,000 psi (40 MPa) (Wakeley et al., 1994).

D3.1.2 Crushed Salt

The total strain rate for the crushed-salt constitutive model is assumed to consist of three components. These components include nonlinear elastic ($\dot{\varepsilon}^e_{ij}$), creep consolidation ($\dot{\varepsilon}^c_{ij}$), and creep ($\dot{\varepsilon}^i_{ij}$) contributions, and the total strain rate ($\dot{\varepsilon}_{ij}$) can be written as:

$$\dot{\varepsilon}_{ij} = \dot{\varepsilon}^e_{ij} + \dot{\varepsilon}^c_{ij} + \dot{\varepsilon}^i_{ij} \tag{D-5}$$

Both the nonlinear elastic and creep consolidation portions of the model describe the material behavior in bulk (volumetric deformation) and in shear (deviatoric deformation). However, the creep portion of the crushed-salt model only describes deviatoric behavior. In fact, the creep portion of the crushed-salt model is the same as that of intact salt, i.e., the Munson-Dawson model described in Section D3.2.1. Nonlinear elastic and creep consolidation models used for crushed salt are described in the next sections.

Nonlinear Elastic Model for Crushed Salt. Elastic strain, ε^e_{ij}, is the contribution from the stress field given by Hooke's law, which, in terms of the bulk modulus and shear modulus, is written as:

$$\varepsilon^e_{ij} = \frac{\sigma_m}{3K}\delta_{ij} + \frac{S_{ij}}{2G} \tag{D-6}$$

where:

σ_m = $\frac{\sigma_{kk}}{3}$, mean stress

S_{ij} = $\sigma_{ij} - \sigma_m \delta_{ij}$, deviatoric stress

δ_{ij} = Kronecker delta

K = bulk modulus

G = shear modulus.

Sjaardema and Krieg (1987) propose bulk and shear moduli as exponential functions of the current density, ρ:

$$K = K_0 e^{K_1 \rho}$$
$$G = G_0 e^{G_1 \rho} \qquad \text{(D-7)}$$

where K_0, K_1, G_0, and G_1 are material constants. The current density (ρ) is written in terms of the total volumetric strain, ε_v, using the relation:

$$\rho = \frac{\rho_0}{1+\varepsilon_v} \qquad \text{(D-8)}$$

where ρ_0 is the density of the material before the volumetric strain is imposed. The moduli are capped at values consistent with moduli for intact salt when the current density equals intact salt's density.

Table D-5 lists material parameters of the nonlinear elastic model for WIPP crushed salt. The terms K_0 and G_0 are the leading coefficients defining the bulk and shear moduli, respectively as the density approaches zero. The terms K_1 and G_1 are identical in magnitude and describe the density dependence in Equation D-7. Exponential function parameters are from Sjaardema and Krieg (1987). Intact crushed-salt constants (K_f, G_f, and ρ_f) are based on recent measurements on WIPP salt.

Table D-5. Nonlinear Elastic Material Parameters for WIPP Crushed Salt

Parameter	**Units**	**Value**
K_0	MPa	0.01760
K_1	m^3/kg	0.00653
G_0	MPa	0.0106
G_1	m^3/kg	0.00653
K_f	MPa	23,504
G_f	MPa	14,156
ρ_f	kg/m^3	2,160

Creep Consolidation Models for Crushed Salt. Four constitutive laws were used to describe the creep consolidation portion of the crushed-salt model:

- Sjaardema-Krieg
- Revised Sjaardema-Krieg
- Zeuch
- Spiers.

The first model is based on the work of Sjaardema and Krieg (1987) with a deviatoric component added (Callahan and DeVries, 1991). In this study, this model is referred to as the original S-K model. This model can be expressed mathematically as:

$$\dot{\varepsilon}_{ij}^{c} = \frac{(1+\varepsilon_v)^2}{\rho_0} B_0\left(1-e^{-B_1\sigma_m}\right) e^{A\rho}\left\{\frac{\delta_{ij}}{3}-\frac{S_{ij}}{\sigma_e}\right\} \tag{D-9}$$

where:

ε_v = ε_{kk}, total volumetric strain

σ_e = average effective stress measure

B_0, B_1, A = material constants.

Because Equation D-9 allows for unlimited consolidation, a cap is introduced that eliminates further consolidation when the intact material density (ρ_f) is reached. Thus, when the condition

$$|\varepsilon_v| \geq \left| \frac{\rho_0}{\rho_f} - 1 \right| \tag{D-10}$$

is satisfied, no further creep consolidation occurs.

Table D-6 gives values of the crushed-salt parameters for the original S-K model.

Table D-6. Creep Consolidation Parameters for Crushed Salt (after Sjaardema and Krieg, 1987)

Parameter	Units	Value
B_0	$kg/m^3 \bullet s^{-1}$ $kg/m^3 \bullet yr^{-1}$	1.3×10^{8} 4.10×10^{15}
B_1	MPa^{-1}	0.82
A	m^3/kg	-1.73×10^{-2}

The second creep consolidation model used in this study is a revised Sjaardema-Krieg model, reported originally by Callahan et al. (1995) and recently updated to include a more general formulation and an updated database by Callahan et al. (1996). The mathematical form of this model is:

$$\dot{\varepsilon}_{ij}^{c} = \dot{\varepsilon}_{eq}^{c}\left(\sigma_{eq}^{f}\right)\frac{\partial\,\sigma_{eq}}{\partial\,\sigma_{ij}} \tag{D-11}$$

where $\dot{\varepsilon}_{eq}^{c}$ and σ_{eq}^{f} are the power-conjugate equivalent inelastic strain measure and equivalent stress measure for creep consolidation, respectively, and σ_{eq} is an equivalent stress measure that provides a nonassociative formulation in governing the magnitude of the volumetric strain.

With these considerations, the equivalent stress measures can be written as:

$$
\begin{aligned}
\sigma_{eq}^{f} &= \eta\left|\sigma_m\right|^{\eta_2} - \frac{\left|\sigma_1-\sigma_3\right|^{m_1}}{\sigma_{r_1}^{m_1-1}} \\
\sigma_{eq} &= \kappa\left|\sigma_m\right|^{\kappa_2} - \frac{\left|\sigma_1-\sigma_3\right|^{m_1}}{\sigma_{r_2}^{m_2-1}}
\end{aligned}
\qquad \text{(D-12)}
$$

where:

$\eta = \eta_0(1-\Omega)^{\eta_1}$

$\kappa = \kappa_0(1-\Omega)^{\kappa_1}$

$\Omega = \begin{Bmatrix} D_t, 0 < D < D_t \\ D, D_t < D < 1 \end{Bmatrix}$

D_t = transitional fractional density

D = fractional density

σ_1 and σ_3 = principal stresses

σ_{r_1} and σ_{r_2} = reference stresses

$\eta_0, \eta_1, \eta_2,$
$\kappa_0, \kappa_1, \kappa_2,$
m_1, m_2 = material parameters.

The kinetic equation as described by the revised Sjaardema-Krieg model can be written as:

$$
\dot{\varepsilon}_{eq}^{c} = \frac{B_0\ (1\ +\ \varepsilon_v)^2}{\rho_0\ d^p}\ \exp\left(\frac{A\rho_o}{1\ +\ \varepsilon_v}\right)\left[1+a_1\left(1-e^{-a_2 w}\right)\right]e^{\frac{-Q_c}{RT}} \qquad \text{(D-13)}
$$

where:

d = grain diameter

w = percent moisture by weight

T = absolute temperature

R = universal gas constant

$B_0, A, p,$
a_1, a_2, Q_c = material parameters.

The revised Sjaardema-Krieg creep consolidation model has a total of 17 parameters, which are listed in Table D-7.

Table D-7. Revised Sjaardema-Krieg, Zeuch, and Spiers Creep Consolidation Parameter Values

Parameter	**Units**	**Modified Material Models**			**Reference Values**
		Sjaardema-Krieg	**Zeuch**	**Spiers**	
η_0	$\mathrm{MPa}^{1-\eta_2}$	-1.437	-42.33	$-2.91(10^{-6})$	—
η_1	—	2.594	2.740	0.108	—
η_2	—	3.623	3.049	5.523	—
m_1	—	0.731	0.605	0.174	—
σ_{r_1}	MPa	3.535	18.33	0.019	—
D_t	—	0.867	0.888	0.881	—
a_1	—	17.00	20.10	71.10	—
a_2	—	47.50	96.60	0.626	—
Q_c/R	K	$4.01(10^3)$	$9.26(10^{-17})$	$1.8(10^2)$	—
p	—	0.564	0.396	$3.22(10^{-5})$	—
B_0	$\mathrm{kg} \bullet \mathrm{m}^{p-3}/(\mathrm{MPa} \bullet \mathrm{s})$	$6.459(10^7)$			—
A	m^3/kg	$-1.307(10^{-2})$			$-1.72(10^{-2})$
b_2	—		4.469		1/3
b_3	—		5.722		1/2
b_7	$\mathrm{m}^p/(\mathrm{MPa} \bullet \mathrm{s})$		$6.54(10^{-14})$		—
b_8	$\mathrm{m}^p/(\mathrm{MPa} \bullet \mathrm{s})$		$9.05(10^{-19})$		—
n	—		9.991		4.9
r_1	$\mathrm{m}^p/(\mathrm{MPa} \bullet \mathrm{s})$			$1.02(10^{-7})$	—
r_3	—			9.770	1/3
r_4	—			0.806	2
n	—			3.190	4.15

The third model used for the creep consolidation is the Zeuch model, which is based on the kinetics of isostatic pressing. Similar to the revised Sjaardema-Krieg model, the Zeuch model was modified to account for a more general formulation. The Zeuch model is divided into two stages, depending on the fractional density. The kinetic equation describing the modified Zeuch model is:

For Stage 1 ($D_0 \leq D \leq 0.9$):

$$\dot{\varepsilon}^{c}_{eq} = \frac{\rho_0 b_7}{\rho\, d^p} D_0^{b_2} D^{2(b_2-n)-1} \left(\frac{D - D_0}{1 - D_0} \right)^{b_3-n} \left[1 + a_1 (1 - e^{-a_2 w}) \right] \exp\left(-\frac{Q_c}{RT} \right) \qquad \text{(D-14)}$$

For Stage 2 ($0.9 < D \leq 1$):

$$\dot{\varepsilon}^{c}_{eq} = \frac{\rho_0 b_8}{\rho\, d^p} \frac{(1-D)}{\left\{1-(1-D)^{1/n}\right\}^n} \left[1 + a_1(1 - e^{-a_2 w})\right] \exp\left(e - \frac{Q_c}{RT}\right) \tag{D-15}$$

where $D = D_0/(1+\varepsilon_v)$ and b_2, b_3, b_7, b_8, n, a_1, a_2, and Q_c are model parameters (Table D-7).

The fourth model was developed by Spiers and coworkers based on pressure solutioning as the consolidation mechanism. The Spiers model was also modified to account for a more general formulation and an updated database by Callahan et al. (1996). The modified Spiers model is:

$$\dot{\varepsilon}^{c}_{eq} = \frac{r_1}{d^p}\left[1 + a_1(1 - e^{-a_2 w})\right] e^{\frac{-Q_c}{RT}} \left(\frac{(1+\varepsilon_v)^{r_2}}{|\varepsilon_v|^{r_3}}\right) \Gamma \tag{D-16}$$

where:

$$\Gamma = \begin{cases} 1 & \text{small strain } (\varepsilon_v > -15\%) \\ \left[\dfrac{\varepsilon_v + \phi_0}{\phi_0(\varepsilon_v + 1)}\right]^n & \text{large strain } (\varepsilon_v < -15\%) \end{cases} \tag{D-17}$$

and ϕ_0 is the initial porosity and r_1, r_2, r_3, n, a_1, a_2, p, and Q_c are material parameters (Table D-7).

D3.1.3 Compacted Clay

The clay used in the WIPP shaft seal design is assumed to behave according to a nonlinear elastic model. The form of this model is identical to the nonlinear elastic portion of the crushed-salt model, in which the bulk and shear moduli are expressed as exponential functions of the current density:

$$\begin{aligned} K &= K_0 e^{K_1 \rho} \\ G &= G_0 e^{G_1 \rho} \end{aligned} \tag{D-18}$$

The parameters for the volumetric (bulk) behavior of clay are based on consolidation data reported in Lambe and Whitman (1969). These parameters are listed in Table D-8. The intact shear modulus (G_f) was calculated from the bulk modulus, assuming a Poisson's ratio of 0.25.

D3.1.4 Asphalt

Thermal properties of solidified asphalt are given in Table D-9. These properties are taken from the literature (Yoder and Witczak, 1975). Asphalt was assumed to behave elastically. The elastic (primarily bulk) response of the asphalt is considered most important to seal application. Because the asphalt is emplaced in a confined volume and the expected stresses that develop (as a result of creep of the surrounding salt and weight of the overlying seal materials) are compressive in nature, the volumetric behavior of the material is important to characterize.

The shear and time-dependent behavior of the asphalt are secondary effects. Young's modulus and Poisson's ratio of asphalt are listed in Table D-10. These properties are taken from Yoder and Witczak (1975) and are highly sensitive to temperature. The values shown in Table D-10 are representative of the WIPP repository horizon temperature of 27°C. Asphalt stiffness is assumed to be zero before it solidifies; i.e., it behaves as a fluid.

Although it is recognized that the behavior of asphalt is certainly time-dependent, the creep effects of this material were not considered in this modeling effort. As noted above, the predominant structural behavior of the seals is highly dependent on the behavior of surrounding materials, primarily creep of surrounding salt. Elastic behavior is assumed to be the predominant behavior because the asphalt is confined and will be volumetrically compressed. Because of confinement, there is little opportunity for creep flow of asphalt. In addition, the primary mechanism for creep (shear stress) of the asphalt is not expected to occur.

Table D-8. Nonlinear Elastic Material Parameters for Compacted Clay

Parameter (Equation D-18)	Units	Value
K_0	MPa	$2.26(10^{-6})$
K_1	m^3/kg	0.0096
G_0	MPa	$1.36(10^{-8})$
G_1	m^3/kg	0.0096
K_f	MPa	20,824
G_f	MPa	12,494
ρ_f	kg/m^3	2,390

Table D-9. Asphalt Thermal Properties

Property	Units	Value
Thermal Conductivity	W/m-K	1.45
Specific Heat	J/kg-K	712
Density	kg/m^3	2000

Table D-10. Asphalt Elastic Properties

Property	Units	Value
Young's Modulus	MPa	3034
Poisson's Ratio	—	0.35

D3.2 In Situ Materials

The in situ materials include Salado salt, Salado interbeds (anhydrite and polyhalite), and rock types encountered in the near-surface and Rustler Formations. Thermal, deformational, and strength characteristics of these materials required for structural analyses are given in the following subsections.

D3.2.1 Salado Salt

Thermal Properties. Thermal properties of Salado salt are given in Table D-11. These values are reported by Krieg (1984). Thermal conductivity of Salado salt is temperature dependent, expressed mathematically as:

$$k(T) = k_{300}(300/T)^{\lambda} \tag{D-19}$$

where:

$k(T)$ = thermal conductivity of salt as a function of temperature

T = temperature (K)

k_{300} = thermal conductivity at reference temperature ($T = 300$ K) = 5.0 W/m-K

λ = exponent describing temperature dependence = 1.14.

Table D-11. Salado Salt Thermal Properties

Property	Units	Value
Thermal Conductivity	W/m-K	(Equation D-19)
Specific Heat	J/kg • K	971
Density	kg/m^3	2160

Deformational Characteristics. Intact salt was assumed to be argillaceous salt that is governed by the Multimechanism Deformation Coupled Fracture (MDCF) model (Chan et al., 1995a). This model is an extension of the well-documented Munson-Dawson (M-D) creep model (Munson et al., 1989) to include a calculation of damage. The evolutionary equations for the MDCF model are:

$$\dot{\varepsilon}^{i}_{ij} = \dot{\varepsilon}^{c}_{ij} + \dot{\varepsilon}^{d}_{ij} + \dot{\varepsilon}^{h}_{ij} \tag{D-20}$$

The first inelastic strain rate represents climb-controlled creep, which is described by the following kinetic equation:

$$\dot{\varepsilon}^{c}_{ij} = \dot{\varepsilon}^{c}_{eq} \frac{\partial \sigma^{c}_{eq}}{\partial \sigma_{ij}} \tag{D-21}$$

where σ^{c}_{eq} and $\dot{\varepsilon}^{c}_{eq}$ are power-conjugate equivalent stress measure and equivalent inelastic strain rate for the climb-controlled creep deformation mechanisms, respectively. The second inelastic strain rate represents damage accumulation in the model. Two kinetic equations describe the damage model, one for shear-induced damage and one for cleavage fracture. These kinetic equations are additive to give the total inelastic damage strain rate as follows:

$$\dot{\varepsilon}_{ij}^{d} = \dot{\varepsilon}_{eq}^{\omega_s}\,\frac{\partial\sigma_{eq}^{\omega_s}}{\partial\sigma_{ij}} + \dot{\varepsilon}_{eq}^{\omega_t}\,\frac{\partial\sigma_{eq}^{\omega_t}}{\partial\sigma_{ij}} \tag{D-22}$$

where $\left\{\sigma_{eq}^{\omega_s} \text{ and } \sigma_{eq}^{\omega_t}\right\}$ and $\left\{\dot{\varepsilon}_{eq}^{\omega_s} \text{ and } \dot{\varepsilon}_{eq}^{\omega_t}\right\}$ are power-conjugate equivalent stress measures and equivalent inelastic strain rates for the damage mechanisms, respectively. The third inelastic strain rate represents healing in the model. For calculations performed in support of the shaft seal design, healing was not operative, i.e., $\dot{\varepsilon}_{ij}^{h} = 0$.

Climb-Controlled Creep

The equivalent inelastic strain rate is assumed to consist of a multiplicative transient function on the steady-state creep rate, viz.:

$$\dot{\varepsilon}_{eq}^{c} = \mathrm{F}\dot{\varepsilon}_{s} \tag{D-23}$$

The steady-state strain rate consists of three mechanisms that describe dislocation climb, an undefined mechanism, and dislocation glide.

$$\dot{\varepsilon}_{s} = \sum_{i=1}^{3} \dot{\varepsilon}_{s_i} \tag{D-24}$$

$$\dot{\varepsilon}_{s_1} = A_1\left(\frac{\sigma_{eq}^{c}}{(1-\omega)\mu}\right)^{n_1} \exp\left(-\frac{Q_1}{RT}\right) \tag{D-25}$$

$$\dot{\varepsilon}_{s_2} = A_2\left(\frac{\sigma_{eq}^{c}}{(1-\omega)\mu}\right)^{n_2} \exp\left(-\frac{Q_2}{RT}\right) \tag{D-26}$$

$$\begin{aligned}\dot{\varepsilon}_{s_3} = {} & \left[B_1 \exp\left(-\frac{Q_1}{RT}\right) + B_2 \exp\left(-\frac{Q_2}{RT}\right)\right] \times \\ & \sinh\left[q\,\frac{\left(\dfrac{\sigma_{eq}^{c}}{(1-\omega)} - \sigma_0\right)}{\mu}\right] H\left(\frac{\sigma_{eq}^{c}}{(1-\omega)} - \sigma_0\right)\end{aligned} \tag{D-27}$$

The transient function, F, describes work-hardening, equilibrium, and recovery branches:

$$F = \begin{cases} \exp\left[\Delta\left(1-\dfrac{\zeta}{\varepsilon_t^*}\right)^2\right] & \zeta < \varepsilon_t^* \\ 1 & \zeta = \varepsilon_t^* \\ \exp\left[-\delta\left(1-\dfrac{\zeta}{\varepsilon_t^*}\right)^2\right] & \zeta > \varepsilon_t^* \end{cases} \tag{D-28}$$

with an internal variable, ξ, described in terms of an evolutionary equation as:

$$\dot{\zeta} = (F-1)\dot{\varepsilon}_s \tag{D-29}$$

and the transient strain limit is defined by:

$$\varepsilon_t^* = K_0 \exp(cT)\left(\frac{\sigma_{eq}^c}{(1-\omega)\mu}\right)^m \tag{D-30}$$

with the hardening parameter, Δ, given by:

$$\Delta = \alpha + \beta\ \log\left(\frac{\sigma_{eq}^c}{(1-\omega)\,\mu}\right) \tag{D-31}$$

where:

R = universal gas constant

μ = normalizing parameter

q = activation volume

σ_0 = stress limit of dislocation slip mechanism

A_1, A_2, B_1,
B_2, n_1, n_2,
Q_1, Q_2, q,
K_0, c, m,
α, β, δ = experimental constants

H(.) = Heaviside step function.

The maximum shear stress (Tresca) is chosen as the conjugate stress measure for climb-controlled creep:

$$\sigma_{eq}^c = 2\sqrt{J_2}\psi \tag{D-32}$$

where:

$$J_2 = \frac{1}{2}\ s_{ij}s_{ji}$$

$$s_{ij} = \sigma_{ij} - \sigma_m \delta_{ij}$$

$$\sigma_m = \frac{\sigma_{kk}}{3},\ \text{mean stress}$$

$$\delta_{ij} = \text{Kronecker delta}$$

$$\Psi = \frac{1}{3}\sin^{-1}\left[\frac{-3\sqrt{3}\,J_3}{2\,J_2^{3/2}}\right]\ \left(-\frac{\pi}{6} \le \Psi \le \frac{\pi}{6}\right) \tag{D-33}$$

$$J_3 = \frac{1}{3} s_{ij}s_{jk}s_{ki}$$

Damage Induced Flow

The damage strain rate in Equation D-22 is examined next with the two terms representing shear-induced damage and tension-induced damage considered separately (Chan et al., 1992; Chan, 1994a, 1994b; Chan et al., 1995b):

$$\dot{\varepsilon}_{ij}^{\omega_s} = \dot{\varepsilon}_{eq}^{\omega_s}\ \frac{\partial \sigma_{eq}^{\omega_s}}{\partial \sigma_{ij}},\ \text{and}\ \dot{\varepsilon}_{ij}^{\omega_t} = \dot{\varepsilon}_{eq}^{\omega_t}\ \frac{\partial \sigma_{eq}^{\omega_t}}{\partial \sigma_{ij}} \tag{D-34}$$

The equations describing the shear-induced (*s*) and tension-induced (*t*) damage are similar in form. Thus, the subscript *i* is used to represent *s* and *t*. The equivalent inelastic strain rate is given by:

$$\dot{\varepsilon}_{eq}^{\omega_i} = F^{\omega_i}\,\dot{\varepsilon}_s^{\omega_i} \tag{D-35}$$

with:

$$F^{\omega_s} = F\ \exp\left[\frac{c_4\left(\sigma_{eq}^{\omega_s} - c_5\right)}{\sigma_0(1-\rho)}\right] \tag{D-36}$$

$$F^{\omega_t} = F\ \exp\left[\frac{c_4\left(\sigma_{eq}^{\omega_t} - c_5\right)}{\sigma_0(1-\rho)}\right] \tag{D-37}$$

and:

$$\dot{\varepsilon}_s^{\omega_i} = c_1\omega_0 \exp\left(c_3\omega\right)\left[\sinh\left(\frac{c_2\sigma_{eq}^{\omega_i}\,H\left[\sigma_{eq}^{\omega_i}\right]}{[1-\omega][1-\rho]\,\mu}\right)\right]^{m_3} \tag{D-38}$$

and c_1 is defined by:

$$c_1 = c_0\left[B_1 \exp\left(-\frac{Q_1}{RT}\right) + B_2 \exp\left(-\frac{Q_2}{RT}\right)\right] \tag{D-39}$$

where c_0, c_2, c_3, c_4, c_5, and n_3 are material constants and ω_0 is the initial damage. The power-conjugate equivalent stress measures are given by:

$$\sigma_{eq}^{\omega_s} = |\sigma_1 - \sigma_3| + f_p\, x_2 x_7 \operatorname{sgn}(I_1 - \sigma_3)\left(\frac{I_1 - \sigma_3}{3x_7 \operatorname{sgn}(I_1 - \sigma_3)}\right)^{x_6} \tag{D-40}$$

$$\sigma_{eq}^{\omega_t} = x_1 \sigma_1 H(\sigma_1) \tag{D-41}$$

where x_1, x_2, x_6, and x_7 are material constants of the damage model, I_1 is the first stress invariant, and σ_1 and σ_3 are the maximum and minimum principal stresses, respectively, with compression assumed to be negative. The material parameter f_p is related to the impurity content by:

$$f_p = 1 - p_1\, \rho \tag{D-42}$$

where ρ is the impurity (clay) content and p_1 is a material parameter, which is analogous to a local stress intensity factor.

The preceding equations include the damage (ω), which is described in terms of an evolutionary equation. The damage evolution equation is taken as:

$$\dot{\omega} = \dot{\omega}_s + \dot{\omega}_t - h(\omega, \sigma_{eq}^{h}) \tag{D-43}$$

where the damage rate components for the shear-induced and tension-induced damage are given by:

$$\dot{\omega}_s = \frac{x_4}{t_0}\,\omega\left[\ln\left(\frac{1}{\omega}\right)\right]^{\frac{x_4+1}{x_4}}\left[\frac{\sigma_{eq}^{\omega_s} H(\sigma_{eq}^{\omega_s})}{(1-\rho)\xi_s}\right]^{x_{3_s}} \tag{D-44}$$

$$\dot{\omega}_t = \frac{x_4}{t_0}\,\omega\left[\ln\left(\frac{1}{\omega}\right)\right]^{\frac{x_4+1}{x_4}}\left[\frac{\sigma_{eq}^{\omega_t} H(\sigma_{eq}^{\omega_t})}{(1-\rho)\xi_t}\right]^{x_{3_t}} \tag{D-45}$$

where x_4, x_{3_s}, x_{3_t}, ξ_s, ξ_t, and t_0 are material constants. The parameter ξ_s may have different values according to the magnitude of the effective shear-induced damage stress; i.e.,:

$$\begin{aligned} \xi_s &= \xi_s^1 \text{ for } \sigma_{eq}^{\omega_s}/(1-\omega) > \sigma_0 \\ \xi_s &= \xi_s^2 \text{ for } \sigma_{eq}^{\omega_s}/(1-\omega) \le \sigma_0 \end{aligned} \tag{D-46}$$

The healing term in Equation D-43, $h(\omega, \sigma_{eq}^{h})$, was assumed to be zero for these calculations.

The shear-induced inelastic damage flow is assumed to be nonassociative. The flow potential power-conjugate stress measure for shear-induced damage is given by (cf. Equation D-42):

$$\sigma_{eq}^{\omega_s} = \left|\sigma_1 - \sigma_3\right| + \frac{x_2 x_8}{3}\left(I_1 - \sigma_3\right) \tag{D-47}$$

where x_8 is a material constant.

The flow potential power-conjugate stress measure for tension-induced damage is given by:

$$\sigma_{eq}^{\omega_t} = x_1 \sigma_1 H(\sigma_1) \tag{D-48}$$

where x_1 is a material constant.

The Munson-Dawson creep parameter values for argillaceous WIPP salt are listed in Table D-12. The damage parameters are given in Table D-13.

D3.2.2 Salado Anhydrite and Polyhalite

Salado anhydrite and polyhalite interbeds were assumed to behave elastically. Elastic constants for anhydrite and polyhalite are given in Table D-14. These values have been used in previous similar WIPP analyses (Morgan et al., 1987).

DRZ development was assessed using a Drucker-Prager strength criterion. Damage to the interbeds is assumed to occur when the peak material strength of the rock is exceeded. The material strength of brittle rocks can be described by a Drucker-Prager type yield:

$$F = aI_1 + \sqrt{J_2} - C \tag{D-49}$$

where:

I_1 = first invariant of the total stress tensor

J_2 = second invariant of the deviatoric stress tensor

a and C = material constants.

Values for the Drucker-Prager material constants presented by Morgan et al. (1987) for anhydrite and polyhalite are given in Table D-14. The material is elastic when $F < 0$ and will fracture and dilate if $F \geq 0$. The potential for fracture development can be expressed as a factor of safety given by the ratio of the strength measure to the stress measure. The factor of safety as used in this appendix is based on the following equation:

$$\text{Factor of Safety} = \frac{\left|aI_1 - C\right|}{\sqrt{J_2}} \tag{D-50}$$

Table D-12. Munson-Dawson Parameter Values for Argillaceous Salt
(after Munson et al., 1989)

Parameter	Units	Value
Elastic Parameter Values		
E	MPa	31,000
ν	—	0.25
Munson-Dawson Creep Parameter Values		
A_1	yr^{-1} s^{-1}	4.437×10^{30} 1.407×10^{23}
A_2	yr^{-1} s^{-1}	4.144×10^{20} 1.314×10^{13}
Q_1/R Q_1	K cal/mol	12,581 25,000
Q_2/R Q_2	K cal/mol	5032 10,000
n_1	—	5.5
n_2	—	5.0
B_1	yr^{-1} s^{-1}	2.838×10^{14} 8.998×10^{6}
B_2	yr^{-1} s^{-1}	1.353×10^{6} 4.289×10^{-2}
q	—	5.335×10^{3}
σ_0	MPa	20.57
m	—	3
K_0	—	2.47×10^{6}
c	K^{-1}	9.198×10^{-03}
α	—	-14.96
β	—	-7.738
δ	—	0.58

Table D-13. Damage Model Parameters for Argillaceous Salt

Parameter	Units	Value
x_1	—	0.0
x_2	—	9.0
x_3	—	5.5
x_4	—	3.0
x_5	$(\text{MPa})^{x_3}$-s	10^{13}; $\sigma_1 - \sigma_3 > \sigma_0$ 10^{14}; $\sigma_1 - \sigma_3 < \sigma_0$
x_6	—	0.75
x_7	MPa	1
x_8	—	0.1
c_0	—	34.0
c_2	—	850.0
c_3	—	10.0
c_4	—	6.0
n_3	—	3
ω_0	—	10^{-4}
p_1	—	28
ρ_0	—	0.029

Table D-14. Anhydrite and Polyhalite Elastic and Drucker-Prager Parameter Values

Material	E (MPa)	ν	C (MPa)	a
Anhydrite	75,100	0.35	1.35	0.450
Polyhalite	55,300	0.36	1.42	0.473

D3.2.3 Near Surface and Rustler Formations

Failure of the rock within the near-surface and Rustler formations is assumed to be time independent and can be estimated according to two common failure criteria: Tresca and Coulomb criteria. The Tresca criterion for failure is based strictly on the difference between minimum and maximum principal stresses:

$$\sigma_3 - \sigma_1 \geq C_0 \tag{D-51}$$

where C_0 is uniaxial compressive strength. The von Mises criterion is a modification of the Tresca criterion wherein C_0 is replaced by $2C_0/\sqrt{3}$.

The Coulomb criterion accounts for the beneficial effect of confinement and says failure occurs whenever:

$$\begin{aligned}\sigma_1 - \sigma_3 &\geq C_0 + \sigma_3(\tan\beta - 1)\\ \tan\beta &= \frac{1+\sin\phi}{1-\sin\phi}\end{aligned} \tag{D-52}$$

where ϕ is the angle of internal friction.

Strength parameters of rock types encountered in near-surface and Rustler formations are given in Table D-15.

Table D-15. Rock Types and Properties

Rock Type	**Depth (m)**	**Strength Properties**		
		C_0 (MPa)	**T_0 (MPa)**	**ϕ (Deg)**
Mudstone	0-165, 223-260	16.8	1	34.4
Anhydrite	165-183, 192-213	92.6	5.72	44.8
Dolomite	183-192, 213-223	107.3	4	41.9

D3.3 Models for the Disturbed Rock Zone within Salt

Two different models were used to evaluate the development and extent of the DRZ within the intact salt. The first approach is based on the ratio between two stress invariants: i.e., $\sqrt{J_2}/I_1$. This criterion has been used to characterize the potential of salt damage or healing in related WIPP studies. The second approach uses the damage stress (σ_{eq}^{ω}) according to the MDCF constitutive model for WIPP salt. These criteria are discussed in the following subsections.

D3.3.1 Stress-Invariant Criterion

The stress-invariant criterion is based on the separation of stress conditions that do or do not cause dilatancy in WIPP salt when plotted in I_1 - $\sqrt{J_2}$ stress space. I_1 is the first invariant of the stress tensor and represents the mean stress. $\sqrt{J_2}$ is the second invariant of the deviatoric stress tensor and represents the shear stress. Taken together, I_1 and $\sqrt{J_2}$ provide a damage factor that indicates the potential for dilatancy and fracture. The functional form of the stress-invariant criterion is:

$$\frac{\sqrt{J_2}}{I_1}\begin{cases}\geq 0.27;\text{damage occurs}\\ < 0.27;\text{remains intact}\end{cases} \tag{D-53}$$

where:

$$\sqrt{J_2}=\sqrt{\frac{1}{6}\left[(\sigma_1-\sigma_2)^2+(\sigma_2-\sigma_3)^2+(\sigma_3-\sigma_1)^2\right]}$$

$$I_1=\sigma_1+\sigma_2+\sigma_3$$

$\sigma_1,\sigma_2,\sigma_3$ = principal stresses

This criterion is based on experimental evidence of dilation in tested samples of WIPP salt. Other investigators have observed similar stress-invariant criteria for dilatancy in other salts as documented by Van Sambeek et al. (1993b).

D3.3.2 Damage-Stress Criterion

Using the MDCF model (Chan, 1993), the potential level of damage can be evaluated by the power-conjugate equivalent stress measure (the damage stress, σ_{eq}^{ω}). The damage stress for shear-induced damage is given by Chan (1993):

$$\sigma_{eq}^{\omega}=|\sigma_1-\sigma_3|+(1-p_1\,\rho)\;x_2x_7\,\text{sgn}(I_1-\sigma_3)\left[\frac{I_1-\sigma_3}{3x_7\,\text{sgn}(I_1-\sigma_3)}\right]^{x_6}. \tag{D-54}$$

The MDCF damage model constants are given in Table D-13 for argillaceous halite.

D3.3.3 Evaluation of DRZ Models

An evaluation of the stress-invariant (Equation D-53) and damage-stress (Equation D-54) models was performed using the air intake shaft (AIS) permeability testing results reported in Section 3.5 of Appendix C. In this testing, permeability was measured as a function of radius into the surrounding intact salt at two depths (346 m and 626 m) within the Salado Formation. The results of this testing are shown in Figure C-1 of Appendix C. This figure was used to estimate the range in the radial extent of the DRZ. The minimum and maximum normalized DRZ radii at the two depths are given in Table D-16. The term "normalized DRZ radius" is defined as the radial extent of the DRZ into the Salado Formation divided by the AIS shaft radius.

Table D-16. Normalized DRZ Radius Surrounding the AIS

Depth (m)	Minimum	Maximum
346	1.31	1.77
626	1.45	1.92

An estimation of the state of stress surrounding the AIS can be made using the steady-state analytical solution for a circular opening in an infinite domain that has an initial lithostatic stress state (Van Sambeek, 1986). The material is assumed to be governed by a simple Norton creep law and a von Mises flow rule. The solution is given in terms of the radial (σ_{rr}) tangential ($\sigma_{\theta\theta}$), and axial (σ_{zz}) stresses as:

$$
\begin{aligned}
\sigma_1 = \sigma_{rr} &= P_0\left[\left(a/r\right)^{2/n} - 1\right] \\
\sigma_3 = \sigma_{\theta\theta} &= P_0\left[\left(1-2/n\right)\left(a/r\right)^{2/n} - 1\right] \\
\sigma_2 = \sigma_{zz} &= \left(\sigma_{rr} + \sigma_{\theta\theta}\right)/2 \\
&= P_0\left(a/r\right)^{2/n}\left[\left(1-1/n\right) - 1\right]
\end{aligned}
\qquad \text{(D-55)}
$$

where:

$\sigma_1, \sigma_2, \sigma_3$ = maximum, intermediate, and minimum principal stresses, respectively

a = radius of AIS = 3.05 [m]

r = arbitrary raduis (note: $r \geq a$)

P_0 = magnitude of preesixting stress in surrounding salt
= 5.8+0.0225 (d-250) [MPa]

d = depth [m]

n = exponent of effective stress in Norton creep law
= 5.0 (steady-state, time = ∞)
= 1.0 (elastic, time = 0).

The normalized DRZ radius (*r/a*) was calculated as a function of depth by substituting Equation D-55 into Equation D-53 (stress-invariant model) and Equation D-54 (damage-stress model). The results of these calculations are shown in Figure D-2. Superposed on this figure are the AIS field test results (Table D-16). The following conclusions can be made regarding this calculation:

- The stress-invariant model (Equation D-53) substantially underpredicts the measured DRZ.
- The damage-stress model (Equation D-54) provides a conservative estimate (overprediction) of the measured DRZ.

Based on the results of this simple exercise, the damage-stress model was used to estimate the behavior of the DRZ in all subsequent structural calculations.

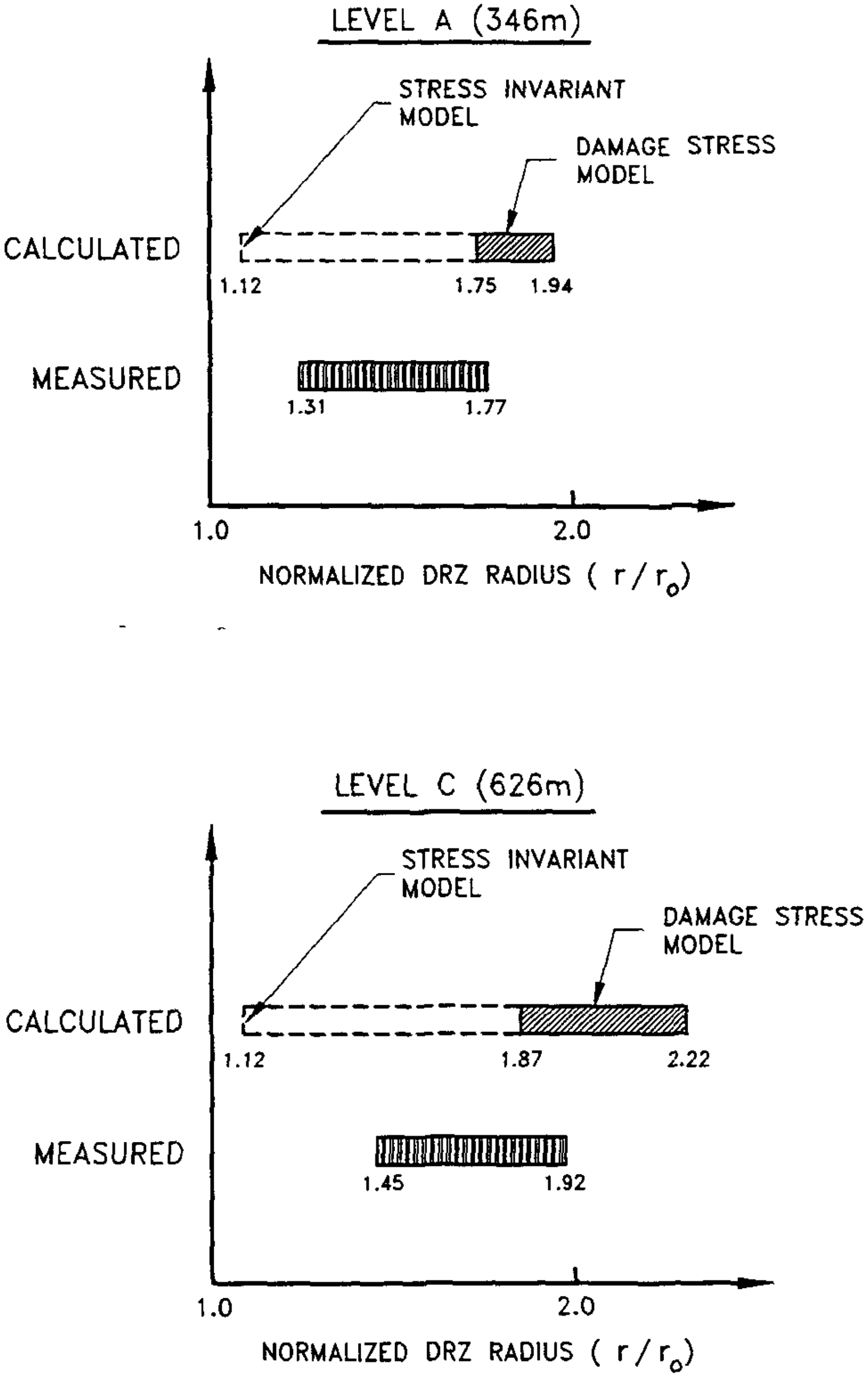

Figure D-2. Comparison of calculated results using damage-stress and stress-invariant DRZ models with measured AIS results.

D4. SHAFT SEAL COMPONENT ANALYSES

D4.1 Salado Mass Concrete Seals

D4.1.1 Thermal Analysis of Concrete Seals

Objective

The objective of this calculation was to determine the expected temperatures within (and surrounding) an SMC emplacement attributable to its heat of hydration.

Problem Description

An axisymmetric representation of the SMC seal, the open shaft, and the surrounding Salado salt is shown in Figure D-3. The left vertical boundary is the centerline of the shaft and is a line of symmetry. The lower horizontal boundary is a plane of symmetry located at the midheight of the SMC seal. The upper horizontal and right vertical boundaries are beyond the thermal influence of the heat-generating SMC seal throughout the simulation period of 1 year. The modeled height of the SMC seal was 6.08 m (20 ft). The radius of the shaft was modeled as 3.04 m. A simulation period of 1 year was determined to be of sufficient duration for the SMC and Salado salt temperatures to reach maximums.

Assumptions

- The SMC seal is placed instantaneously at time = 0 year and generates heat in accordance with Equation D-2.
- The initial temperature of the surrounding salt is 27°C.
- The variations in stratigraphy within the Salado Formation are ignored in this calculation. The in situ material surrounding the shaft was assumed to be entirely Salado salt.
- The seal and shaft are thermally isolated from other seals and other shafts; i.e., the domain surrounding the seal is assumed to be infinite in extent.

Results

Calculated temperatures from this analysis are shown in Figures D-4 and D-5. Figure D-4 shows that locations in the SMC increase in temperature from ambient (27°C) to a maximum of 53°C at 0.02 year after SMC placement. The maximum temperature in the surrounding salt is 38°C at approximately the same time. Figure D-5 shows isotherms within and surrounding the seal at 0.02 year. The thermal gradient within the concrete is approximately 1.5°C/m. This figure also shows that at a radial distance of 2.0 m into the surrounding salt, the temperature rise is less than 1°C.

D4.1.2 Structural Analysis of Concrete Seals

Objective

The objective of this calculation was to determine stresses within the concrete seals resulting from creep of the surrounding salt and the weight of the overlying seal material.

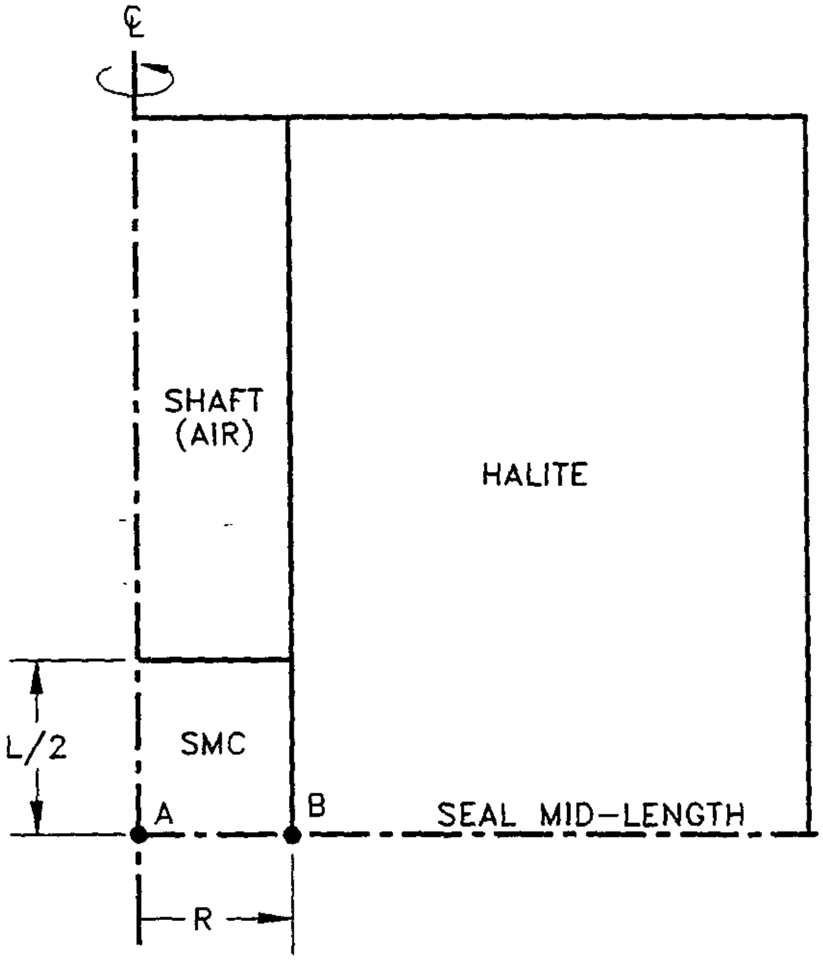

POINT A = SMC Midpoint
POINT B = SMC/Salt Interface
L = Seal Length (20 ft)
R = Shaft Radius = (10 ft)

Figure D-3. Axisymmetric model used in the SMC thermal analysis.

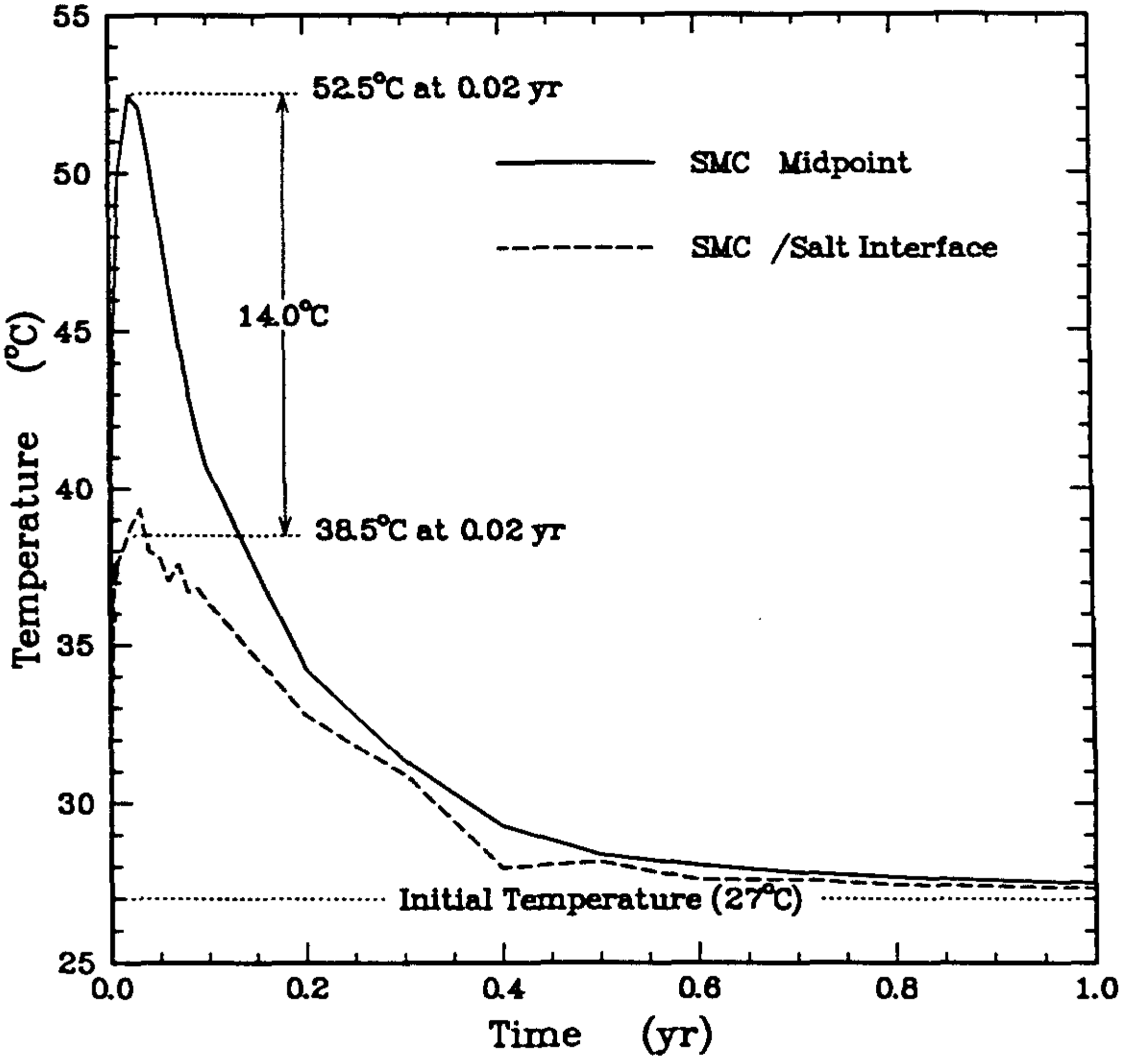

Figure D-4. Temperature histories of SMC center and SMC/salt interface.

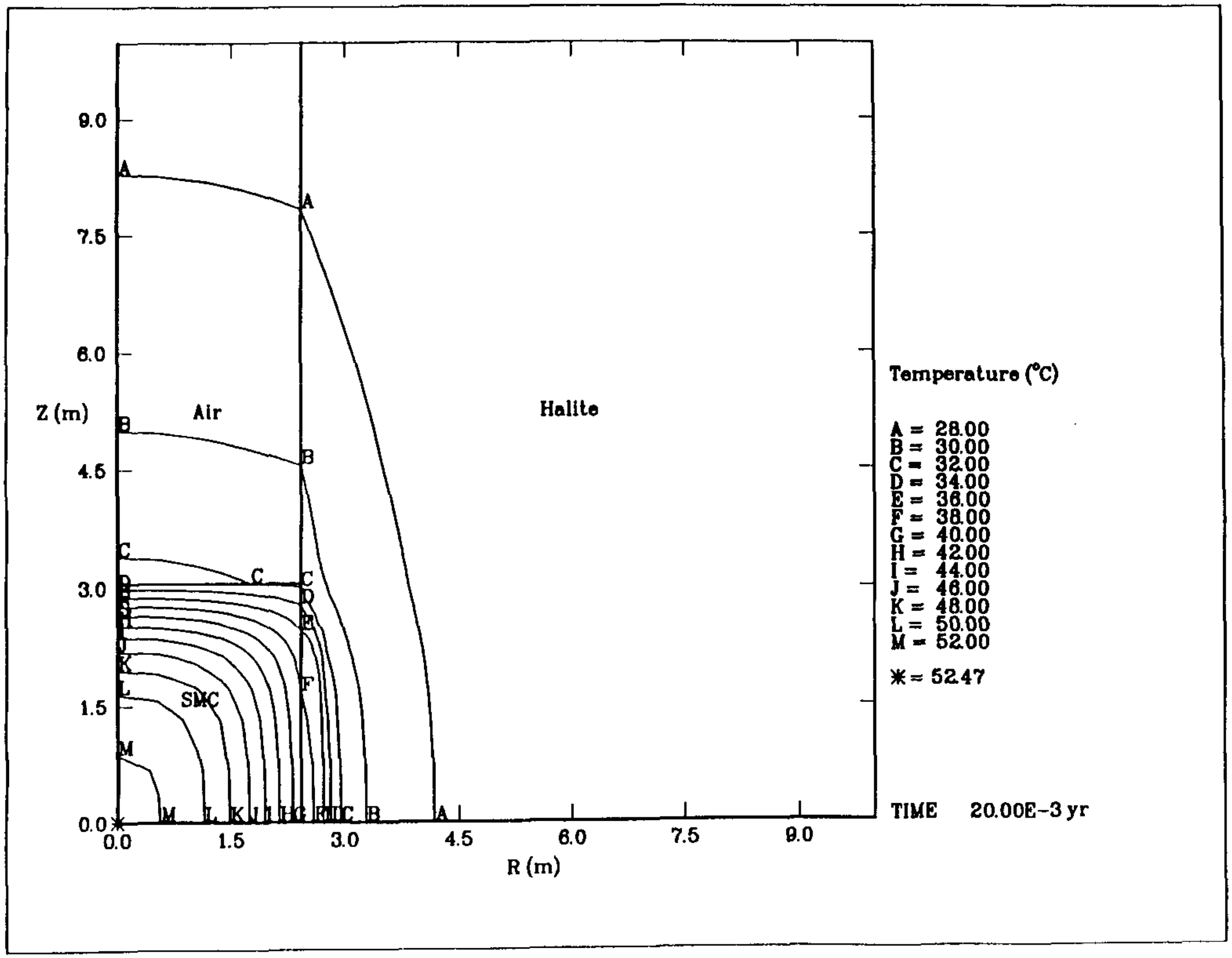

Figure D-5. Isotherms surrounding SMC seal at 0.02 year.

Problem Description

The concrete seal components in the shaft seal were modeled using the Air Intake Shaft (AIS) geometry (see Figure D-6). The bottoms of the concrete components are located in good quality halite at depths of 308 m, 429 m, and 616 m for the upper, middle, and lower concrete seals, respectively. Each of the three concrete components was analyzed independently.

As shown in Figures D-7 through D-9, sealing of the shaft and installation of seal system components were simulated from bottom to top of the modeled region in arbitrary increments of 0.1 year for each stage. The response of the seal components and extent of the DRZ were simulated to 100 years. The following marker beds (MBs) were included in the calculation model: MB101, MB103, MB115, MB116, MB117, MB134, MB136, and the Vaca Triste.

Assumptions

- Axisymmetric conditions are applicable, and a condition of axially restrained displacements exists with respect to the vertical direction at a moderate distance from the seal system.
- The shaft is instantaneously excavated at time $t = 0$. Excavations for the concrete seal wings and waterstop occur instantaneously at time $t = 50$ years.
- Each seal emplacement operation occurs instantaneously.
- The shaft has a uniform initial diameter of 6.1 m.
- The shaft is sufficiently isolated from other excavations that the response of the shaft is unaffected by other underground workings at the WIPP.
- Anhydrite, siltstone, and polyhalite beds exhibit elastic behavior only. Marker beds MB104, MB105, MB118, and MB137 were not modeled in this study because these relatively thin members are not structurally important and would not significantly affect the results.
- Beds comprised predominately of halite are assumed to be argillaceous salt, as defined by the MDCF model, with a clay content of 2.9%.
- Elastic properties of all materials are independent of temperature within the range of interest.
- Inelastic behavior, such as creep, yielding, or cracking, was not modeled for concrete.
- Tension-induced creep damage of salt is ignored.
- Damage stress can be used to indicate if a region within the salt is accumulating damage or healing.
- Initial temperature and stress conditions are listed in Table D-17.

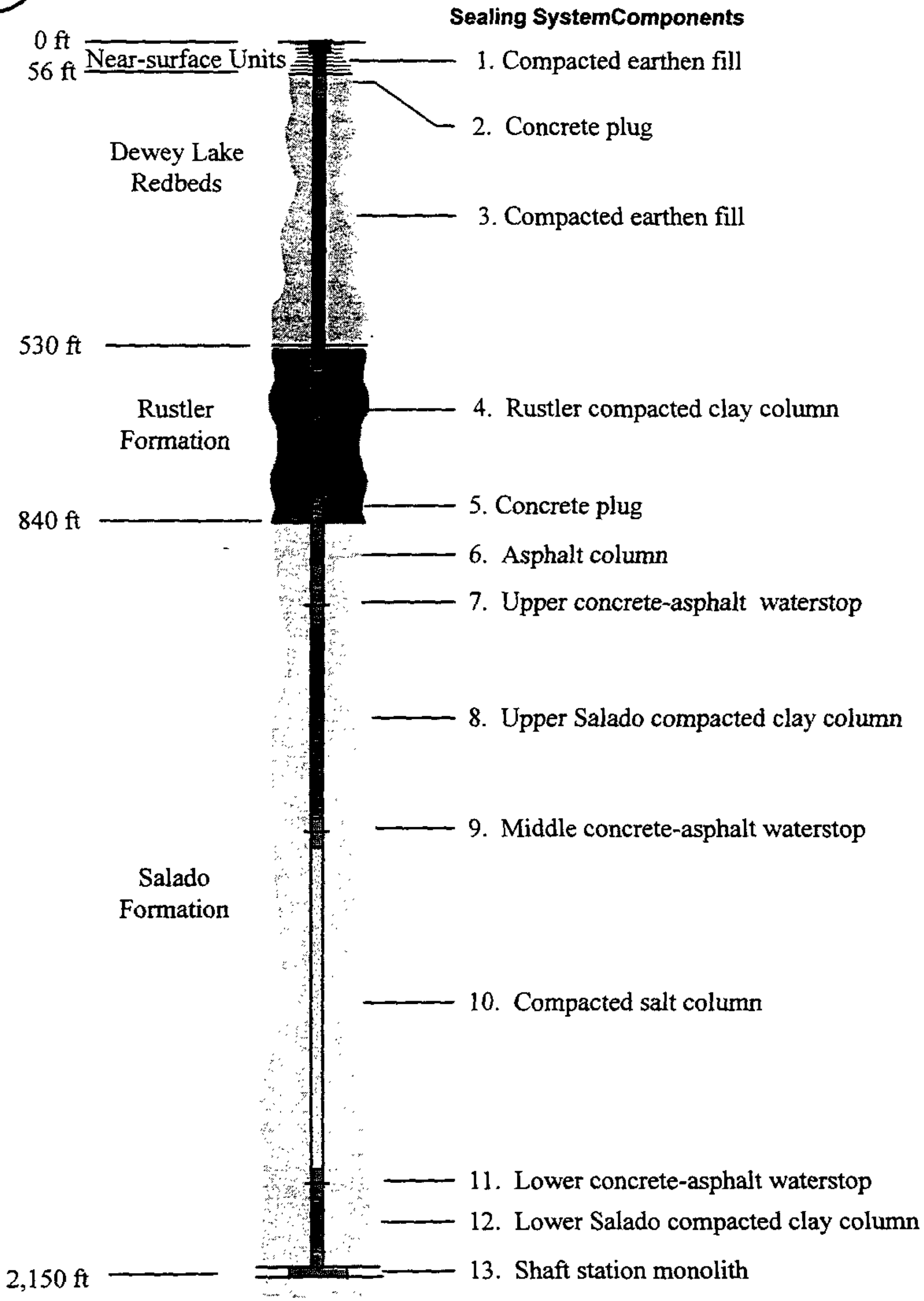

Figure D-6. Seal system conceptual design for the WIPP Air Intake Shaft (DOE, 1995).

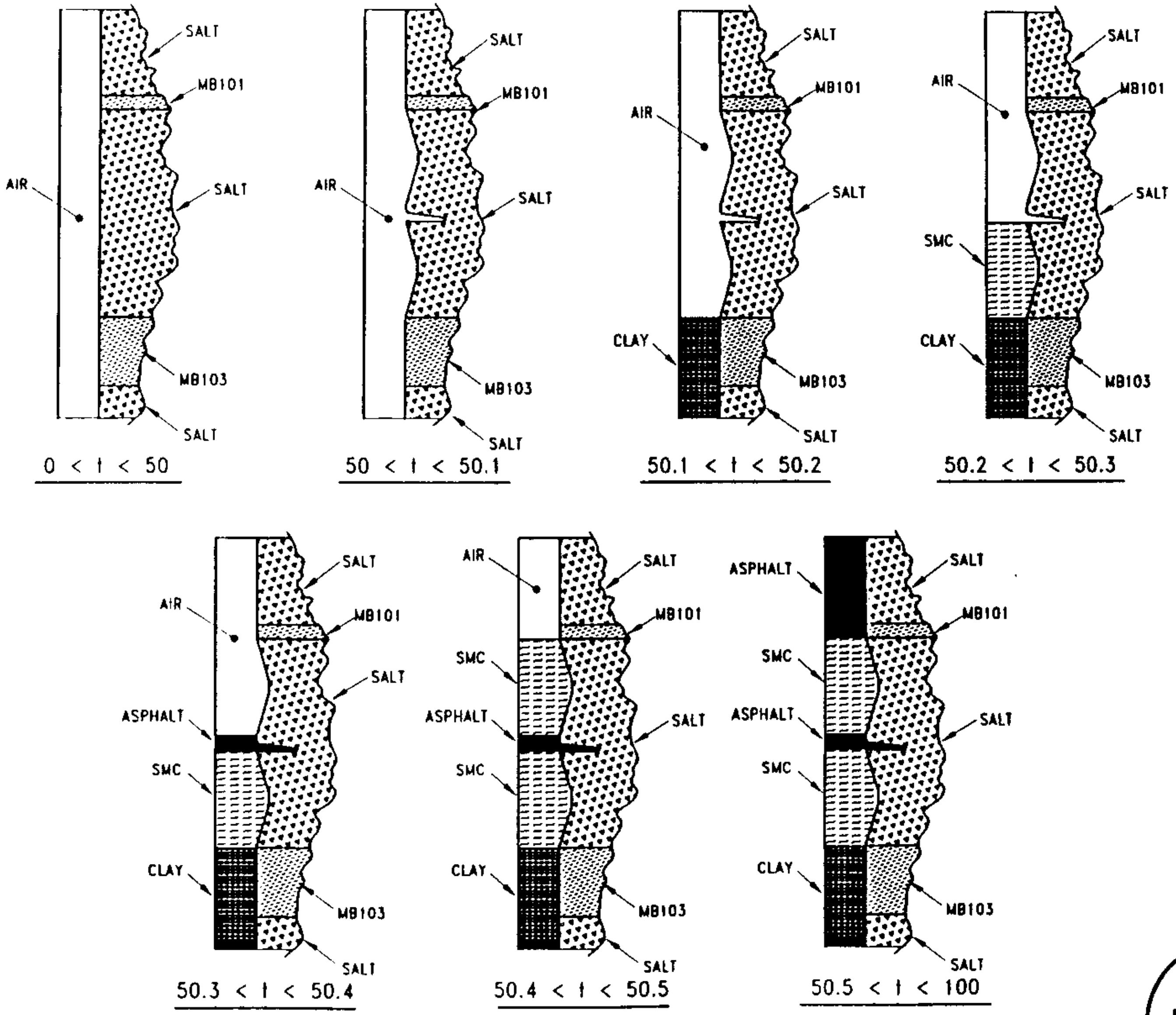

$0 < t < 50$

$50 < t < 50.1$

$50.1 < t < 50.2$

$50.2 < t < 50.3$

$50.3 < t < 50.4$

$50.4 < t < 50.5$

$50.5 < t < 100$

Figure D-7. Axisymmetric model configuration of upper concrete shaft seal.

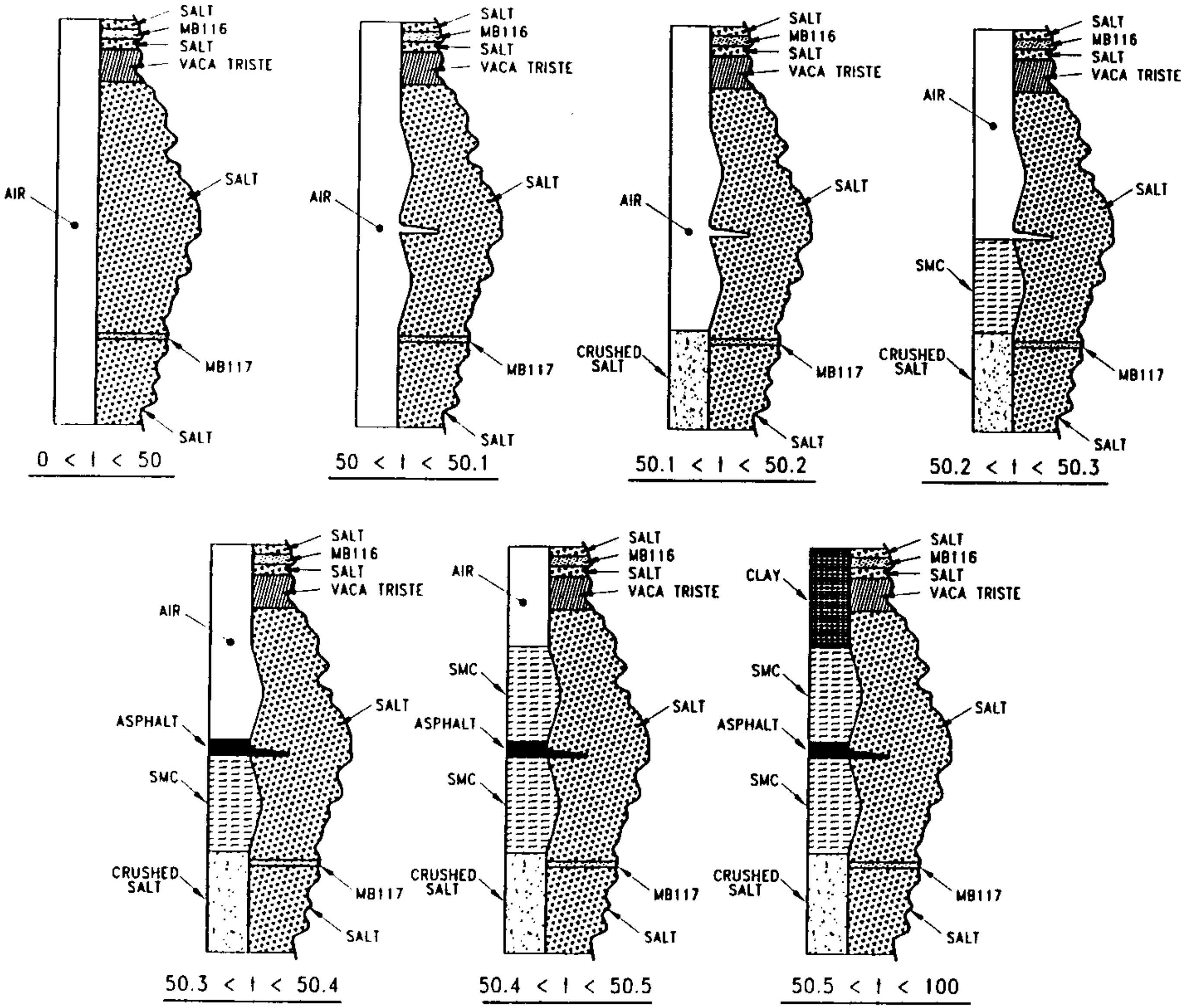

Figure D-8. Axisymmetric model configuration of middle concrete shaft seal.

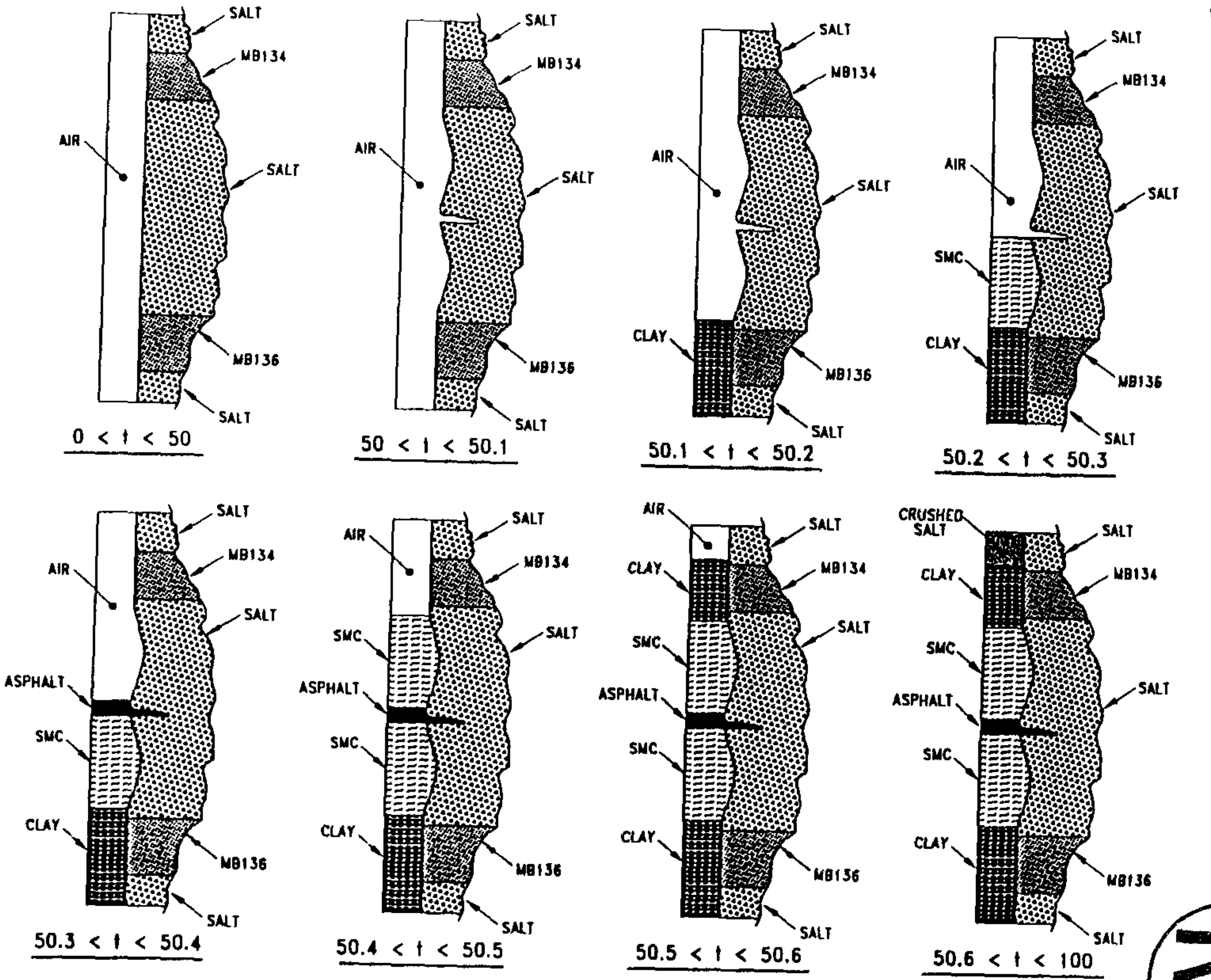

Figure D-9. Axisymmetric model configuration of lower concrete shaft seal.

Table D-17. Initial Temperature and Stress Conditions within Salado Formation

Location Within Salado Formation	**Depth (m)**	**Initial Conditions**	
		Temperature(1) (°C)	Stress(2) (MPa)
Upper	301	23.5	6.95
Middle	421	24.7	9.65
Lower	608	26.6	13.86

(1) Based on temperature of 27°C at 650-m depth and a geothermal gradient of 10°C/km (Sass et al., 1971).
(2) Based on in situ stress of 14.8 MPa at 650-m depth and an average overburden density of 2,300 kg/m^3 (Krieg, 1984, p. 14).

Results

Throughout the calculations, the salt surrounding the shaft creeps toward and into the shafts. This creep causes radial loading on the shaft components when the creep is restrained. In turn, the radial loading induces radial stress in the components. In the upper concrete component, the average radial stress increases from zero at time of emplacement ($t = 0$) to 2.5 MPa at $t = 50$ years. Similarly, the radial stress in the middle concrete component ranges from 3.5 to 4.5 MPa and in the lower concrete component the radial stress ranges from 4.5 to 5.5 MPa at $t = 50$ years.

To determine the axial loading on the shaft components, it was assumed that each concrete component must support the weight of the overlying seal material between it and the next concrete component. Using an average vertical stress gradient of 0.02 MPa/m, the calculated vertical stresses on the upper, middle, and lower concrete components from the weight of the overlying seal material are 7.0, 2.4, and 3.8 MPa, respectively. The specified design strength of the concrete material is 31.0 MPa.

D4.1.3 Thermal Stress Analysis of Concrete Seals

Objectives

The objectives of this calculation were (1) to determine the stresses in the concrete as a result of its heat of hydration and (2) to determine the thermal impact on the creep of the surrounding salt.

Problem Description

Compressive stresses develop within the concrete as a result of thermal expansion of the concrete and restrained creep of the surrounding salt. Thermal stresses within the concrete were calculated using the formula:

$$\sigma_T = \mathrm{E}\,\alpha\,\Delta T \qquad \text{(D-56)}$$

where:

σ_T = thermal stress (for a fully confined condition)

E = Young's modulus

α = linear coefficient of thermal expansion

ΔT = temperature increase.

Thermal results indicate that the concrete will heat to approximately 53°C at approximately 0.02 year after placement (see Section D4.1.1) from an ambient temperature of 27°C. The surrounding salt heats to a maximum of 38°C at approximately the same time.

Results

The thermoelastic stresses in the concrete were calculated based on a maximum temperature increase of 26°C (Figure D-4) and assuming a fully confined condition. The calculation results indicate that short-term thermal stresses in the concrete are less than 9.2 MPa.

As shown in Figure D-4, the maximum salt temperature will be approximately 38°C at 0.02 year of the emplacement. While it is understood that elevated temperatures do increase the creep rate of salt, the small magnitude and short duration of the thermal pulse in the salt had negligible effect on increasing stresses in concrete through enhanced salt creep.

D4.1.4 Effect of Dynamic Compaction on Concrete Seals

Objective

The objective of this simple calculation was to determine a thickness of seal layer above each of the concrete components to reduce the impact of dynamic compaction.

Problem Description

As shown in Figure D-6, compacted clay and salt columns are included in the shaft seal design directly above the three concrete components. These seal materials may be dynamically compacted as they are emplaced.

The compacted depth (D) was calculated using the equation:

$$D = n\left(WH\right)^{1/2} \tag{D-57}$$

where:

W = tamper weight = 5.14 (metric tons)

H = drop height = 6.1 (m)

n = material coefficient.

This equation is taken from a construction reference manual and is based on a functional fit to field measurements. The material coefficient (n) is given as 0.5 for all soil deposits and was used in the calculation for crushed salt. For clay, this coefficient ranges from 0.35 to 0.40 for decreasing moisture content. A higher value of n results in a larger compactive depth.

Results

Using Equation D-57 and the design inputs, the compacted depths for crushed salt and clay are 9.2 feet and 7.2 feet, respectively. The calculations indicate that the provided thickness for crushed salt (12 ft) and clay (10 ft) are greater than the compacted depth.

D4.1.5 Effect of Clay Swelling Pressures on Concrete Seals

Objectives

The objectives of this analysis were to determine the potential for failing the concrete components as a result of clay swelling pressures and the potential for fracturing the salt where the swelling pressure acts directly on the shaft wall.

Problem Description and Results

In order to fail the concrete seals, the applied swelling pressures must exceed the compressive strength of the concrete (4,500 psi = 31.0 MPa). Test measurements on confined bentonite at a density of 1.8 g/c^3 (Pfeifle and Brodsky, 1991) indicate that the maximum swelling pressures are on the order of 3.5 MPa (Figure D-10). These test results were used to approximate the induced stresses on the concrete seals from clay swelling pressures.

D4.2 Crushed Salt Seal

D4.2.1 Structural Analysis of Crushed Salt Seal

Objective

The objective of this calculation was to determine the fractional density of the crushed salt seal as a function of time and depth within the shaft.

Problem Description

The analysis performed is illustrated schematically in Figure D-11, which also shows the model geometry. The model is an axisymmetric representation of the shaft and host rock at a prescribed depth. For time $t < -50$ years, the shaft is not present and a self-equilibrating initial lithostatic (hydrostatic) stress field exists in the salt such that the three principal stresses are identical. At time $t = -50$ years, the cylindrical shaft is "excavated," and the surrounding salt is allowed to creep for 50 years, i.e., the operational period. At time $t = 0$, crushed salt is compacted in the shaft with an initial density of 1.944 Mg/m^3 (90% of the intact salt density). Salt surrounding the shaft continues to creep inward and consolidates the crushed salt until the crushed-salt seal reaches the intact density of salt. At that time, the model describing crushed salt is changed to the model for intact salt. Crushed salt was modeled using the candidate models discussed in Section D3.1.2. A simulation time of 450 years after emplacement was used, which is sufficient to allow the compacted crushed salt, even at the shallowest depth, to achieve a fractional density greater than 99% of the density of intact salt for each of the three crushed-salt models.

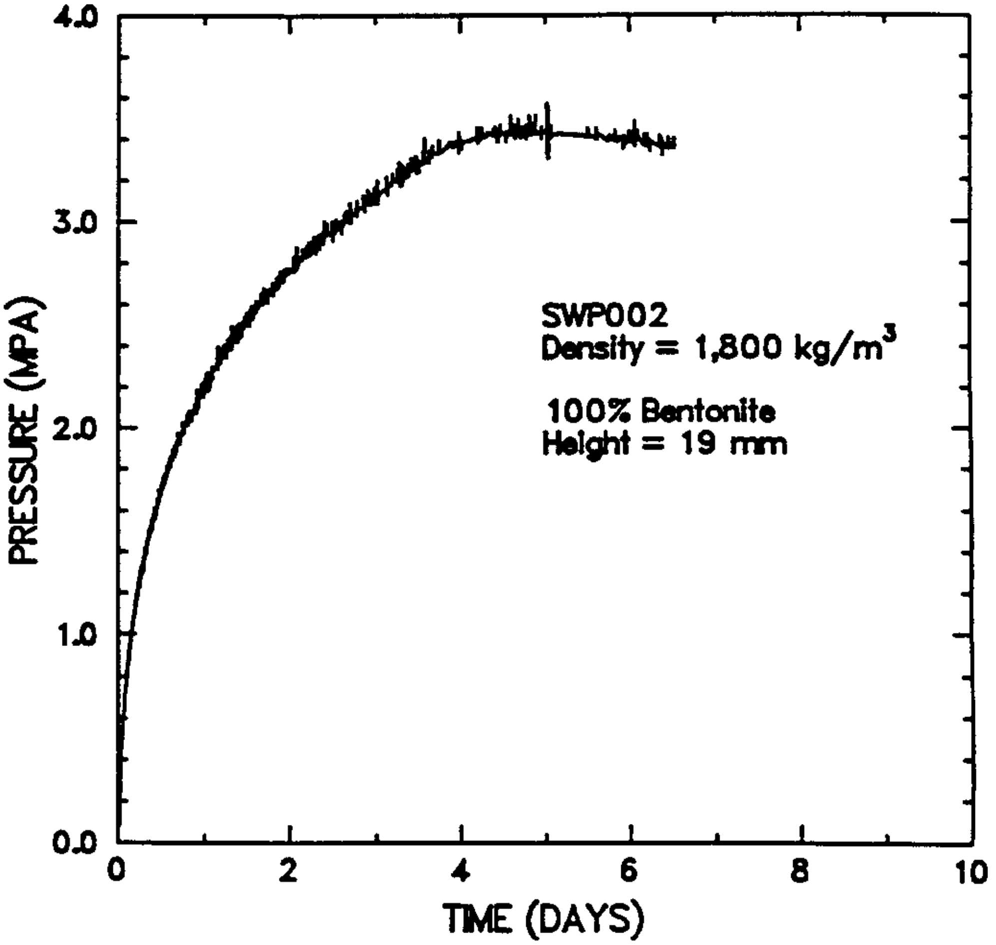

Figure D-10. Swelling pressures as a function of time for a brine-saturated bentonite specimen with a density of 1,800 kg/m^3.

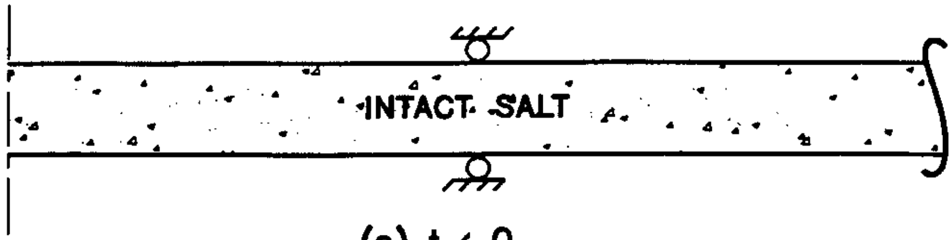

(a) $t < 0$

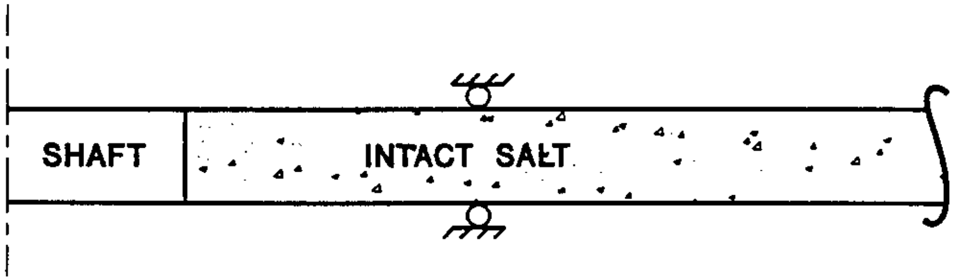

(b) 0 years $< t \leq$ 50 years

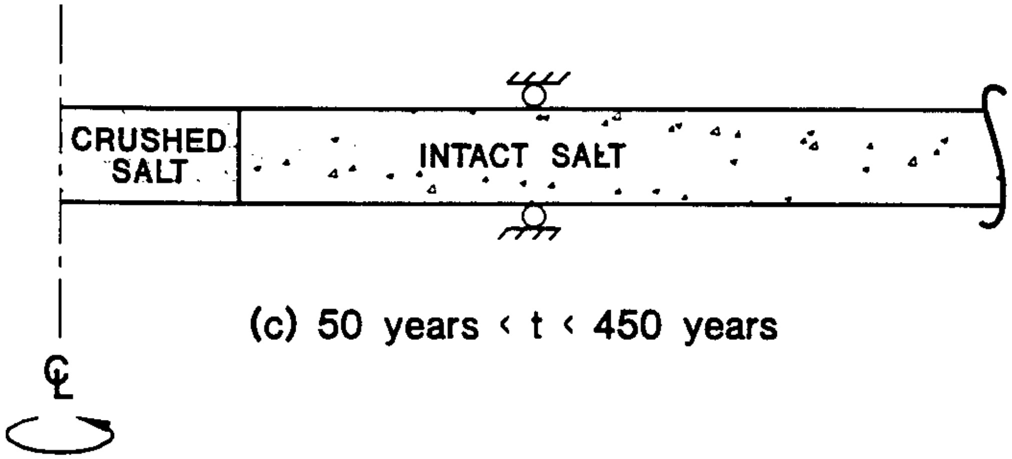

(c) 50 years $< t <$ 450 years

Figure D-11. "Pineapple slice" axisymmetric models.

Assumptions

- Axisymmetric conditions exist around the shaft, and plane-strain conditions are appropriate with respect to the axial (vertical) direction.
- Vertical variations in stratigraphy are ignored. Intact salt is modeled exclusively as argillaceous salt governed by the MDCF model.
- The initial stress state and temperature vary with depth within the Salado Formation as given in Table D-17.
- The modified creep consolidation models of Zeuch, Spiers, and Sjaardema-Krieg were used. These models include the development of mean stresses in the crushed salt and restraint to creep closure.

Results

The fractional densities of crushed-salt seal at the top (depth = 430 m), middle (depth = 515 m), and bottom (depth = 600 m) of the salt column are shown in Figure D-12 as a function of time for the three consolidation models. The models predict essentially the same behavior for fractional densities ranging from 90 to 95%. The times required to achieve a fractional density of 95% are approximately 40, 80, and 120 years at the bottom, middle, and top of the seal, respectively. Only the modified Sjaardema-Krieg creep consolidation model mathematically allows full consolidation. The times required to theoretically reconsolidate the crushed salt to 100% fractional density are 70 years, 140 years, and 325 years at the bottom, middle, and top of the salt column, respectively.

D4.2.2 Effect of Fluid Pressure on the Reconsolidation of Crushed Salt Seals

Objective

The objective of this calculation was to determine the effect of fluid pressure on the reconsolidation of the crushed-salt seal. The results of this calculation were used as input conditions to the fluid-flow analyses described in Appendix C. Because creep of intact salt is an exponential function of stress, fluid pressure applied to the shaft wall would significantly reduce the closure rate of the shaft and, consequently, the reconsolidation rate of the crushed salt.

Problem Description

In this analysis, three models representative of different depths were used. These models are axisymmetric representations of the AIS and the surrounding intact salt. The reconsolidation rate depends on the depth, fluid pressure, time, and creep rate of the surrounding intact salt. Representative models used in this analysis are shown schematically in Figure D-11. The initial stress and temperature conditions were obtained as described in the notes to Table D-17.

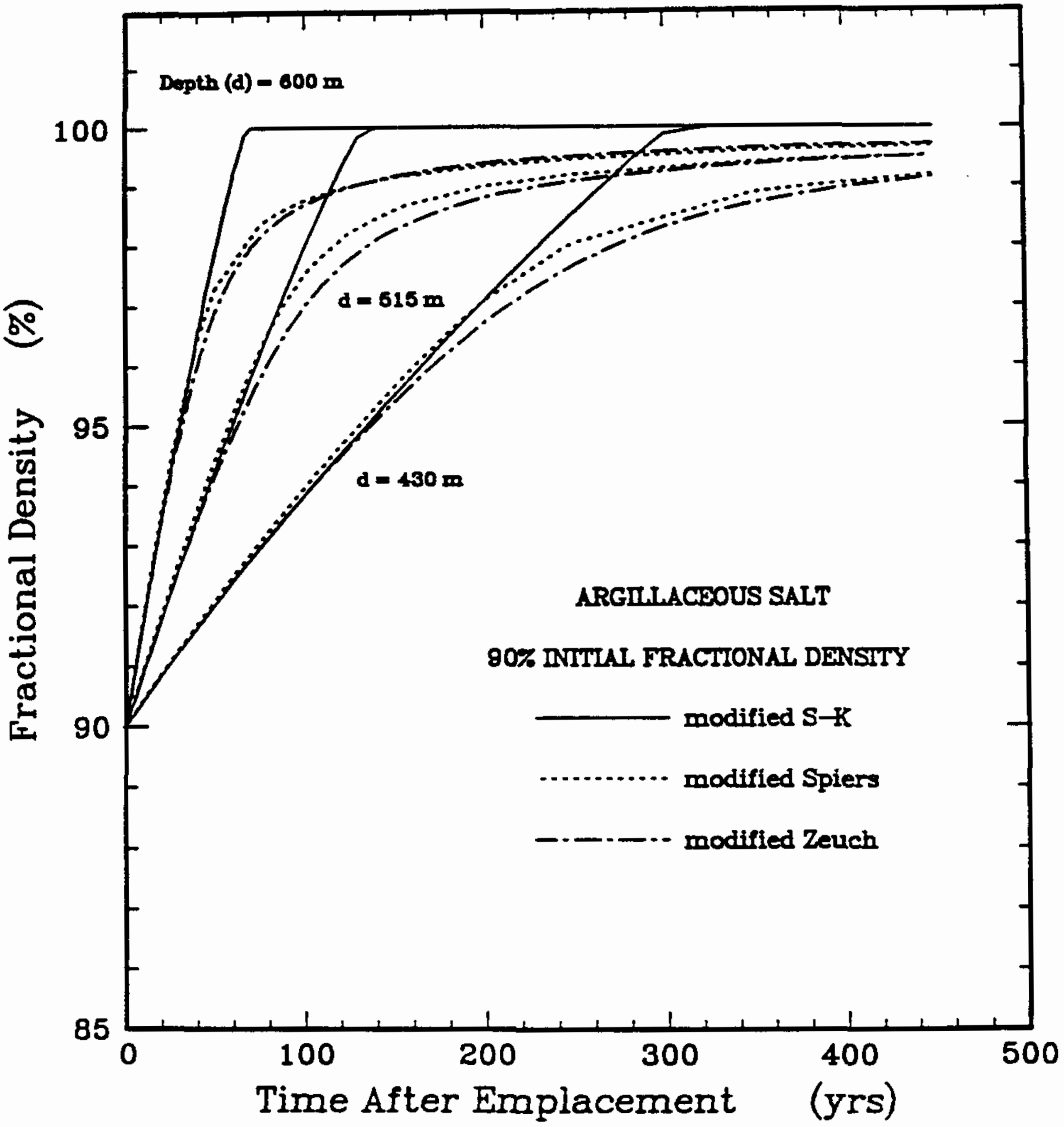

Figure D-12. Consolidation of crushed salt in a shaft at depths of 430, 515, and 600 m using the modified Sjaardema-Krieg, Spiers, and Zeuch models.

Three depths were considered: 430 m, 515 m, and 600 m, which are representative of the top, middle, and bottom of the compacted-salt seal. The fluid in the crushed salt was assumed to behave as a linear elastic material, in which the fluid pressure is related to the volumetric strain through the bulk modulus as:

$$P = MIN\left\{P_0 + K\left(1 - V / V_0\right), P_{\max}\right\} \tag{D-58}$$

where:

P = fluid pressure
P_0 = initial fluid pressure
K = fluid bulk modulus
V = current volume of crushed salt
V_0 = initial volume (based on 90% fractional density)
$P_{\max}$ = maximum fluid pressure.

Maximum fluid pressures ($P_{\max}$) considered are 0, 2, and 4 MPa. These values encompass the allowable range in fluid pressures in terms of salt reconsolidation. Based on the results of this calculation, fluid pressures greater than 4 MPa effectively prevent reconsolidation over a 1000-year time frame.

Assumptions

- The fractional densities of the crushed-salt seal were calculated through 500 years using the modified Sjaardema-Krieg consolidation model.
- The fractional density of the crushed salt after compaction is 90%, i.e., $\rho_0 = 0.90$.
- The shaft remains open for 50 years, then is instantaneously filled with compacted crushed salt.
- The initial fluid pressures are applied instantaneously at time = 50 years. This is a conservative assumption because it provides an immediate restraint to creep closure and results in longer reconsolidation times.
- Vertical variations in stratigraphy and material properties are neglected. Intact salt is modeled exclusively as argillaceous salt governed by the MDCF model.

Results

Results for 0 MPa are shown in Figure D-12; results for 2 MPa are shown in Figure D-13. These results indicate that, as expected, the time required to consolidate the crushed salt increases substantially as the fluid pore pressure increases. For fluid pressures of 4 MPa or greater, reconsolidation times are increased to the point where the crushed salt does not achieve a fractional density of 96% until substantially beyond 1000 years. For zero fluid pressure, times of about 40 years, 70 years, and more than 150 years are required. For a fluid pressure of 2 MPa, the times required to achieve a fractional density of 96% are about 90 years, 200 years, and 560 years at the bottom, middle, and top of the crushed-salt column, respectively.

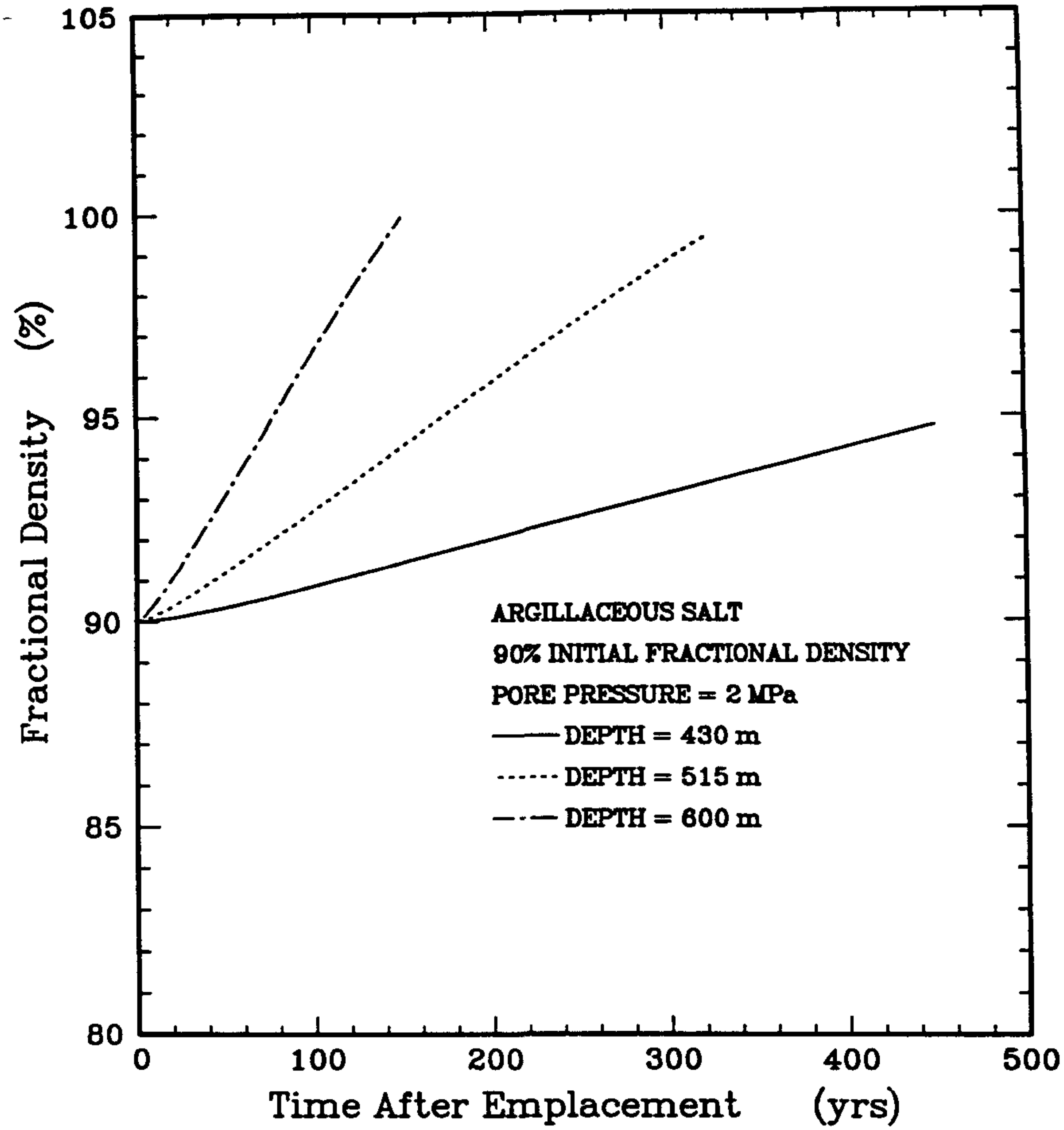

Figure D-13. Crushed-salt fractional density as a function of time for a fluid pressure of 2 MPa and using the modified Sjaardema-Krieg creep consolidation model.

D4.3 Compacted Clay Seals

D4.3.1 Structural Analysis of Compacted Clay Seals

Objective

The objective of this calculation was to determine the stresses in the upper and lower Salado compacted clay columns as a result of creep of the surrounding salt. These stresses may increase the loads imposed on the concrete seal components. The problem description and assumptions used in performing this calculation are the same as those presented in Section 4.1.2. The results of this calculation indicate that after 50 years the compressive stress in the upper Salado compacted clay column ranges from 0.6 MPa at the top to 0.8 MPa at the bottom of the column. Similarly, after 50 years, the mean stresses in the lower Salado compacted clay column are approximately 2.6 MPa.

D4.4 Asphalt Seals

D4.4.1 Thermal Analysis of Asphalt Seals

Objectives

The objectives of this calculation were (1) to determine the temperature histories within the asphalt seal and the surrounding salt and (2) to determine the thermal effects which depend on the length of the waterstop.

Problem Description

A schematic diagram of the AIS seal showing the asphalt components is given in Figure D-14. The AIS is approximately 6.1 m (20 feet) in diameter. The asphalt seal through the Rustler/Salado interface is more than 36 m (119 feet) in height (Figure D-6). The waterstops are 1.22 m (4 feet) in height and, as shown in Figure D-14, extend radially 3.05 m (10 feet) into the surrounding salt.

Two geometrical models were used to calculate thermal results. The first model, shown in Figure D-15(a), represents an asphalt seal of infinite length and can be used to approximate thermal conditions within the asphalt at the Rustler/Salado interface. This model was used to calculate the maximum asphalt (Point A) and salt (Point B) temperatures. The right boundary was extended laterally (100 shaft radii) to be beyond the thermal influence of the asphalt for 10 years. The left vertical boundary represents the shaft centerline and is a line of symmetry. The second model, shown in Figure D-15(b), is referred to as a "quarter-symmetry model." It is used to represent thermal conditions near the asphalt waterstops and to calculate the thermal effects of the radial extent of the waterstop into the salt. The left and lower boundaries are lines of symmetry located at the shaft centerlines and waterstop midheight, respectively. The modeled height of the asphalt is 0.61 m (2 ft). The radial extent of the waterstop as shown in Figure D-15(b) is 3.05 m (10 ft) or equivalently 1 shaft radius into the salt. The right and upper boundaries are extended 100 m from the waterstop center; beyond the thermal influence of the asphalt through 10 years following emplacement. The temperatures at the asphalt center (Point A in Figure D-15) were calculated as a function of time for two cases: (1) no waterstop and (2) full waterstop.

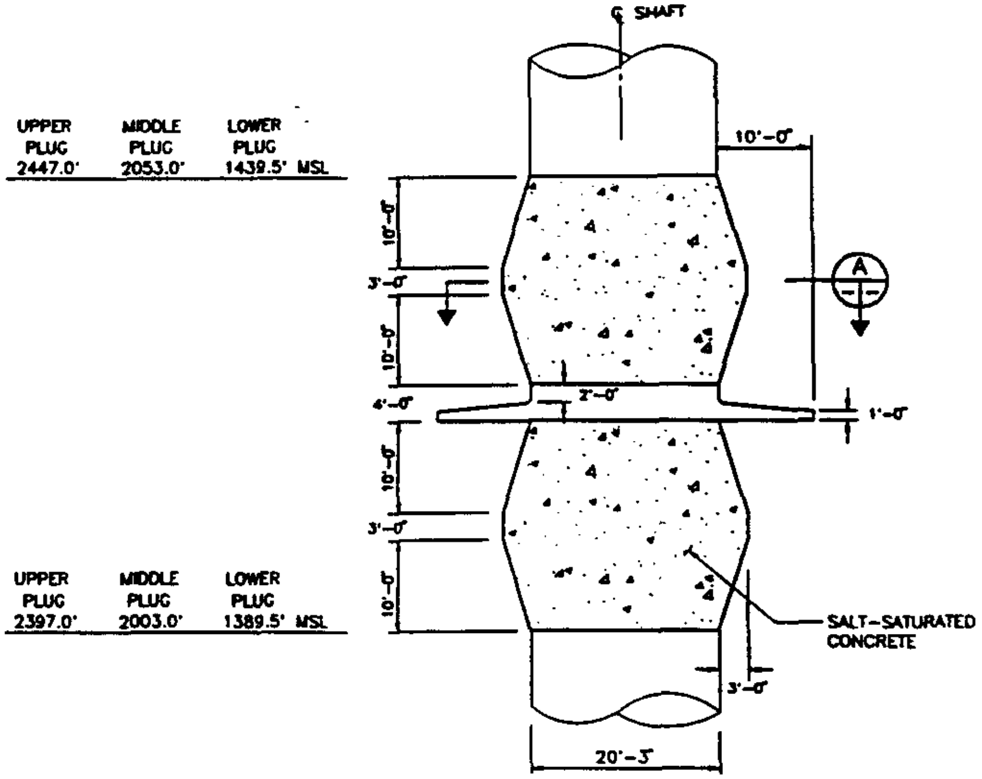

DETAIL 1
SHEET 2 | SHEET 3

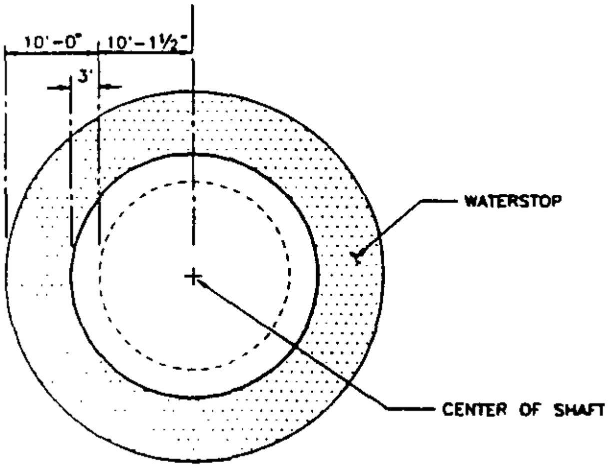

SECTION A

TYPICAL SALADO MASS CONCRETE PLUG
WITH WATERSTOP (3 LOCATIONS)

Figure D-14. WIPP shaft seal design showing asphalt components.

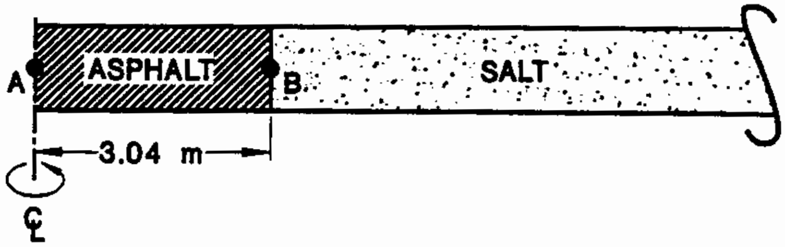

(a) Pineapple-Slice Model

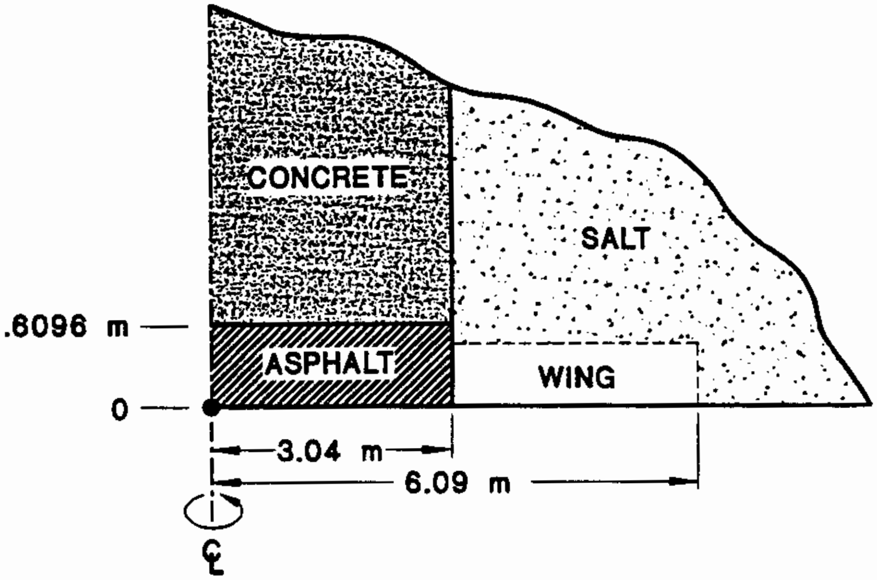

(b) Quarter-Symmetry Model

Figure D-15. Models used in thermal analysis of asphalt seal.

Assumptions

- The initial formation temperature is 23°C everywhere along the length of the seal.
- The AIS is thermally isolated from the remaining shafts; i.e., the domain surrounding the AIS is assumed to be infinite in extent.
- The stratigraphy can be neglected; i.e., the domain is assumed to be homogeneous (salt).
- The heat of hydration of the concrete is ignored.
- All seal materials are emplaced simultaneously at time = 0.
- All boundaries are adiabatic.
- The asphalt is emplaced at 180°C.

Results

The results of this analysis are shown in Figures D-16 through D-18. Figure D-16 shows temperature histories of the asphalt and surrounding salt near the seal midheight. These results indicate that the asphalt center cools from its emplaced temperature of 180°C to 83°C, 49°C, 31°C, and 26°C at times 0.1 year, 0.2 year, 0.5 year, and 1.0 year, respectively. Similarly, the asphalt/salt interface temperatures at the same times are 47°C, 38°C, 29°C, and 26°C.

Figure D-17 shows the temperature histories in the asphalt waterstop. The time required to cool the waterstop is significantly less than that required to cool the asphalt column. Specifically, the waterstop center has cooled to temperatures of 38°C, 29°C, 24°C, and 23°C at times 0.1 year, 0.2 year, 0.5 year, and 1.0 year, respectively.

D4.4.2 Structural Analysis of Asphalt Seals

The objective of this analysis was to calculate the pressures in the asphalt as a result of creep of surrounding salt to evaluate stresses induced on concrete seal components. The problem description and assumptions used in performing this calculation are the same as those presented in Section 4.1.2. The results of this calculation are shown in Figure D-19, which shows the calculated pressure in the upper, middle, and lower asphalt waterstops as a function of time after emplacement. These results indicate that after 100 years, the pressures in the waterstop are 1.8 MPa, 2.5 MPa, and 3.2 MPa for the upper, middle, and lower waterstops, respectively.

D4.4.3 Shrinkage Analysis of Asphalt Seals

Objective

The objective of this analysis was to determine the shrinkage of the asphalt column as it cools from its emplaced temperature to an acceptable working environment temperature.

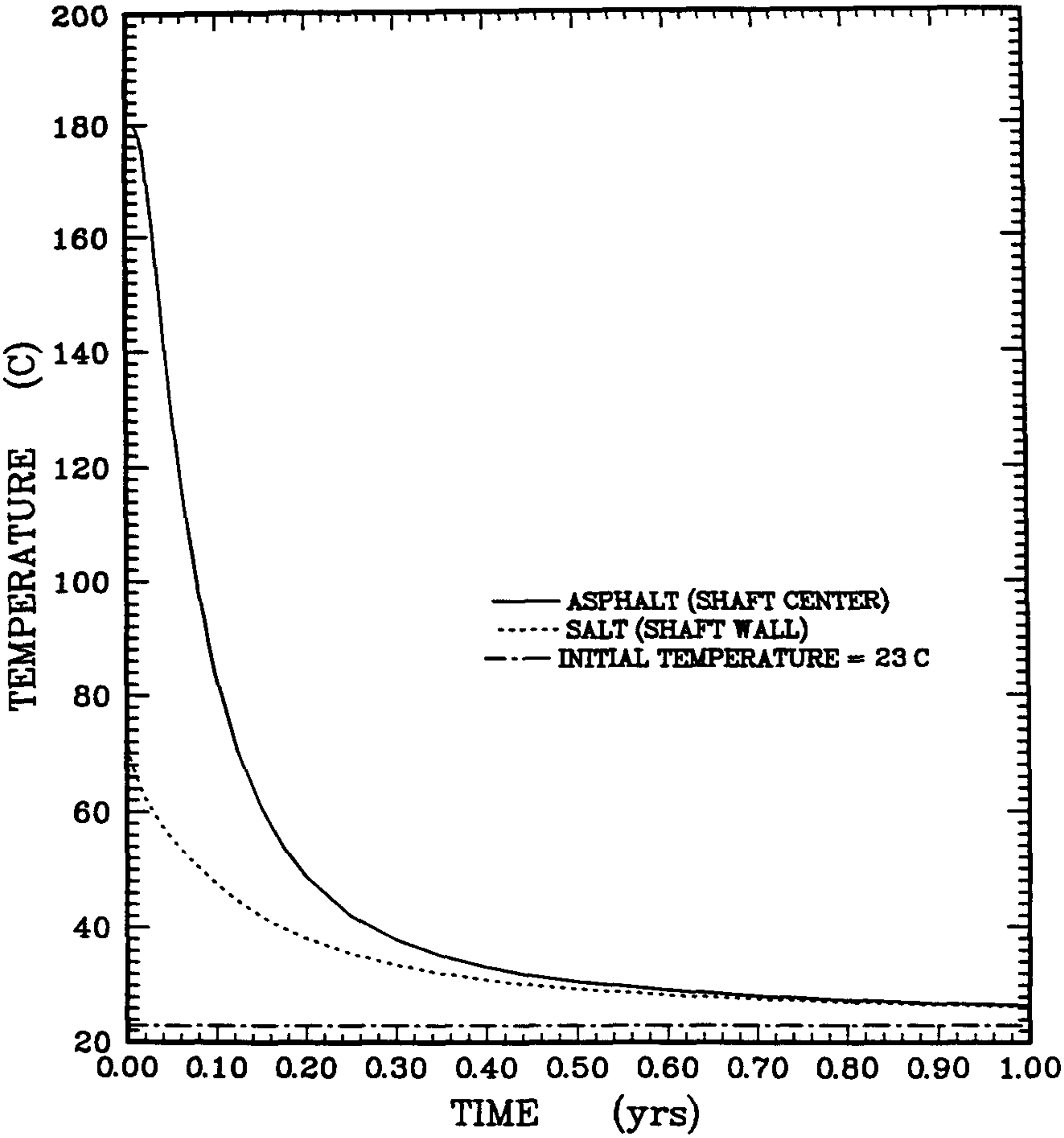

Figure D-16. Temperature histories in asphalt (Point A, Figure D-15a) and salt (Point B, Figure D-15a).

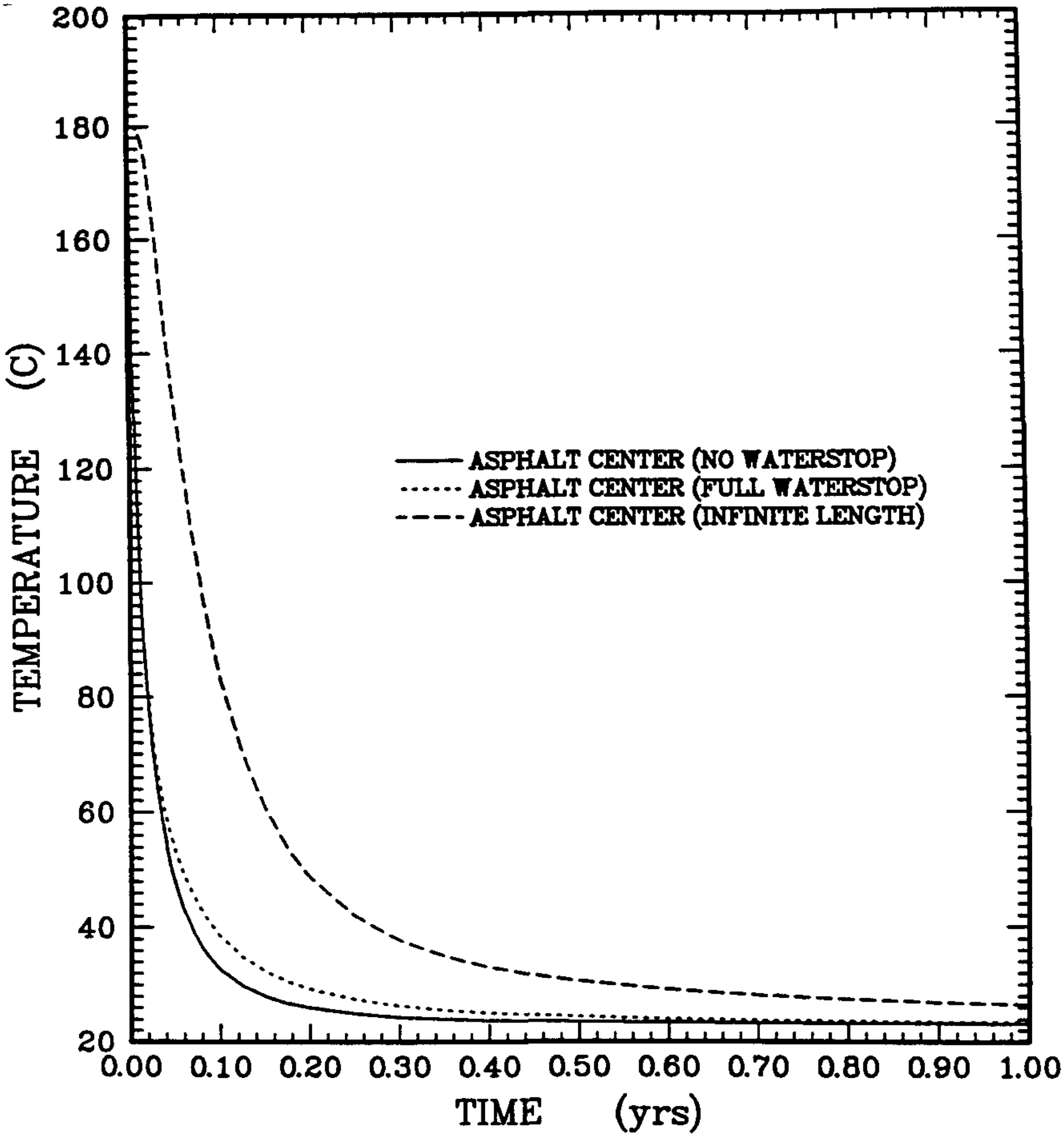

Figure D-17. Comparison of asphalt center temperatures for different waterstop configurations.

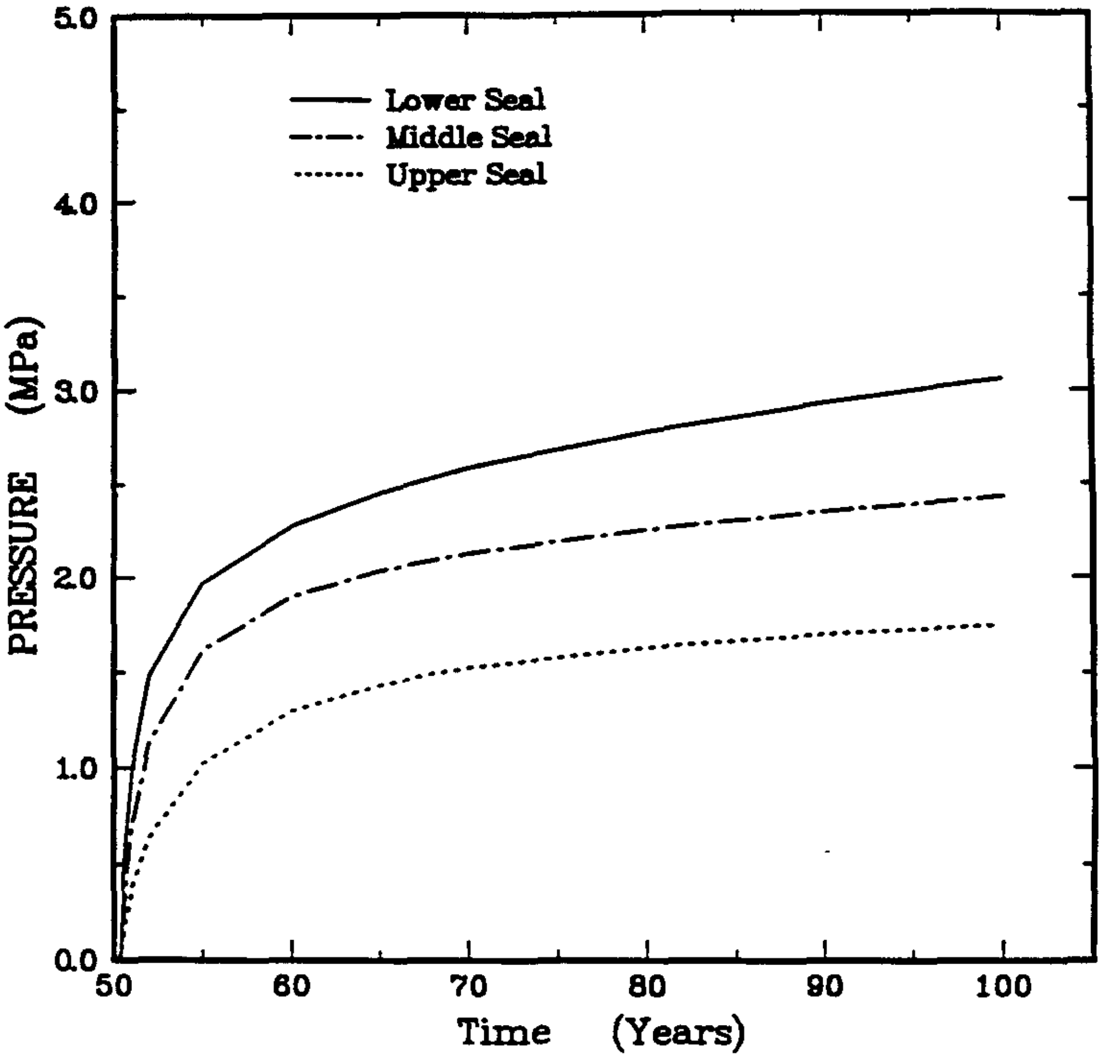

Figure D-18. Pressure buildup in the upper, middle, and lower shaft seal waterstops.

Problem Description

The height of the asphalt column is 138 ft. The volumetric coefficient of thermal expansion for asphalt is 0.00035/°F.[1] The linear coefficient of thermal expansion for sandstone aggregate is 0.000005/°F; the corresponding volume coefficient is about three times the linear coefficient, or 0.000015/°F. Within the column, sand and lime comprise 80% of the volume and asphalt comprises 20%. Thermal contraction can be calculated for each constituent or an equivalent coefficient can be calculated. The equivalent coefficient is:

$$\begin{aligned}\alpha_{\text{mix}} &= 0.8\alpha_{\text{sand}} + 0.2\alpha_{\text{asphalt}} \\ &= 0.8(0.000015) + 0.2(0.00035) \\ &= 0.00008/\text{[illegible]}\end{aligned} \tag{D-59}$$

Assumptions

It is assumed that the asphalt mastic mixture will retain enough mobility that all "voids" caused by shrinkage will occur at the top of the emplacement only. That is, the mixture will flow downward as it shrinks. Accelerated creep closure of the shaft because of heating is ignored in calculating the shaft volume.

Results

The change in height of the asphalt column is given by:

$$\begin{aligned}\Delta h &= \frac{\Delta V}{\pi r^2} = \frac{V\alpha\Delta T}{\pi r^2} = \frac{H\pi r^2\alpha\Delta T}{\pi r^2} = h\alpha\Delta T \\ &= (42.09\,\text{m} \text{ [illegible] } 10^{-4}/^\circ\text{C})(180 - 37.78^\circ\text{C}) \\ &= 0.89\,\text{m}\end{aligned} \tag{D-60}$$

where:

Δh = change in height of asphalt column (m)

ΔV = change in volume of asphalt column (m^3)

r = shaft radius (m)

α = volumetric coefficient of thermal expansion (/°C)

ΔT = temperature change from emplacement (T = 180°F) to cooled state (T = 37.78°C).

---

[1] *Standard Practice for Determining Asphalt Volume Correction to a Base Temperature*, ASTM Designation: D 4311-83, Section 3.3.

D5. DISTURBED ROCK ZONE CONSIDERATIONS

D5.1 General Discussion

A DRZ develops around virtually every underground excavation. The DRZ can be defined as that region near an excavation (in salt or nonsalt rock) that experiences a change in hydrological or mechanical properties. The DRZ is generally assumed to have the following characteristics:

1. dilational deformation resulting from micro- or macrofracturing,
2. decreased load-bearing capacity (loss of strength), and
3. increased fluid permeability (increase in interconnected porosity).

Characterization of the DRZ in salt requires both spatial and temporal considerations. For that purpose, the DRZ can be divided into four regimes: (1) initial creation of the DRZ resulting from stress perturbations brought on by the excavation, (2) changes in rock properties caused by "weathering" of exposed rock, (3) later changes in the DRZ extent that may occur with time as the salt creeps, and (4) a decrease in the DRZ extent (and eventual elimination) that occurs through healing of the micro- and macrofracturing when salt creep is restrained. Remediation of the DRZ may also be possible by engineering fixes such as grouting.

In situ fluid flow and permeability measurements performed in boreholes drilled from excavations in the WIPP provide a geometrical delineation of the DRZ and a measure of the hydrological properties for the DRZ. In general, the disturbance, as reflected by enhanced permeability, is restricted to about one-half the effective radius of the excavation. Within this region the permeability will increase from 10^{-22} to 10^{-23} m^2 (undisturbed permeability) at the edge of the DRZ to about 10^{-14} to 10^{-15} m^2 near the excavation surface (Knowles et al., 1996). Although this discussion relates to underground measurements in the WIPP drifts, a similar delineation of the DRZ around the AIS was observed by Dale and Hurtado (1996).

Underground observations and measurements are consistent with the description of the DRZ extending to less than one excavation radius and having permeabilities that are largest near the excavation boundary and lowest (decreasing by several orders of magnitude to salt's undamaged value) at the edge of the DRZ. Stress states around excavations, whether the instantaneous elastic distributions or the creep-induced stationary distributions, follow a similar trend. Shear stresses are largest near the excavation and become smaller at greater distances from the excavation. This similarity in trends suggests a conclusion that the DRZ can be defined in terms of the stress states existing in the salt. Laboratory testing data from independent laboratories using three different test types also support a conclusion that the onset of damage in salt (dilatant behavior) is predictable based on the stress state imposed on the salt (Van Sambeek et al., 1993a). Other laboratory testing data support a conclusion that damage within a salt specimen can be healed (in fact, healed quite rapidly) by applying favorable stress states to the damaged specimen (e.g., Costin and Wawersik, 1980; Brodsky, 1990). From these results, a conceptual model for the DRZ is developed where (1) the maximum extent of the DRZ is strictly a function of the most severe stress state ever to exist around the excavation and (2) the current extent of the DRZ is defined by the current stress state around the excavation. Implicit is that the disturbed salt will heal "instantaneously" as the stress state is slowly changed from unfavorable (damage inducing) to favorable.

D5.1.1 Salt Damage Models

Two salt damage models are used to define the DRZ for the WIPP seals design: the stress-invariant ratio and the damage stress criterion (Section D.3.2) model. The stress-invariant ratio states that salt will incur damage whenever the ratio between the shear stress (as measured by the second invariant of the deviatoric stress tensor) and the confining pressure (as measured by the first invariant of the stress tensor) exceeds a critical value of 0.27. Mathematically, this is:

$$\frac{\sqrt{J_2}}{I_1} \geq 0.27 \tag{D-61}$$

where $\sqrt{J_2}$ is the shear stress measure and I_1 is the confining stress measure. The relationship is based on laboratory testing data from numerous creep and quasi-static tests on WIPP and Avery Island salts. In general, the relationship seems to represent both different salts and different test types as described by Van Sambeek et al. (1993b).

The MDCF model tracks the development of porosity as result of strain-induced damage within the salt, as described in Section D3.2.1. The dominant deformation mechanism governing the dilational behavior of salt is the time-dependent microfracturing mechanism (Chan et al., 1992). This mechanism is operable for a limited range in stress states (i.e., high shear stresses relative to a low mean stress). The stress states causing microfracturing are typically most severe in the salt immediately adjacent the excavation and less severe deeper into the salt. At some depth, the mean stress increases enough and the shear stresses decrease enough that microfracturing stops; this depth defines the DRZ boundary.

Definition of the DRZ by the MDCF model is preferred over the stress-invariant ratio from a scientific viewpoint because it directly connects the variables of stress, strain, and damage (including damage reversal or healing) in one relationship, albeit a complex relationship. The stress-invariant ratio can only indicate where damage is likely to occur and when healing can begin based on changes in the stress-invariant ratio. The stress-invariant ratio provides no quantitative information about the degree of damage or the significance of the damage in terms of enhanced permeability. The stress-invariant ratio is, however, simpler to apply to engineering problems.

D5.1.2 Salt Healing Models

Healing of damaged salt within the DRZ will occur whenever stress states no longer cause damage. This condition is reached by (1) reducing shear stress, (2) increasing the mean stress, or (3) doing both. The most practical way to achieve a more favorable stress state is to restrain the natural creep of salt by forming a barrier to closure at the free surface of the shaft. By doing so, the stress parallel to the creep deformation direction will increase in compressive magnitude. As this stress increases, the shear stress decreases and the mean stress increases, which is the situation required to reverse the damaging stress condition. Once the damaging stress state is reversed, healing of damage can begin.

Evidence for reversing damaging stress states into healing stress states can be found in (1) natural analogues, (2) laboratory tests (Costin and Wawersik, 1980), (3) in situ seal tests in the WIPP (Knowles et al., 1996), and (4) bulkheads in salt and potash mines. The physical process for healing the microfracture-damaged salt is primarily fluid-assisted pressure solution and redeposition. In addition, dislocation motion of the solid state allows further deformation of crystals to occupy space. Both mechanisms operate effectively at stresses and temperatures applicable to the DRZ around the WIPP shafts.

Natural Analogues. Salt formations are universally considered to have very low permeabilities, which is why salt formations are an ideal storage medium. The Salado salt formation originated as precipitate in oversaturated brines. The original porosity was huge because the salt mass was comprised of loose hopper crystals. With time and superincumbent pressure from additional salts and other sediments, the salt became impermeable, possessing essentially no voids. From this analog, suturing of grain boundaries under natural conditions is demonstrated. The geologic time available for healing is admittedly long; however, the natural stresses and temperatures for the healing process are similar to conditions expected around the WIPP shaft.

Laboratory Test Evidence. Brodsky (1990) and Brodsky and Munson (1994) present test results for the healing of damaged salt under isostatic stress. This work is particularly significant because the salt specimens used in the healing tests had been intentionally damaged in constant-strain-rate tests where the dilatant behavior (volumetric strain) was measured. Thus damage was quantified before the healing phase of the test. The ultrasonic velocity degradation and recovery were monitored during the damage and healing phases. The healing rate, as reflected by ultrasonic velocity recovery, depends on the original damage level, applied pressure, and temperature. The times to full recovery are short, based on the 20-day tests at a 20°C to 70°C range of test temperatures. Therefore, once the seal components restrain the creep of salt and cause confining stresses to develop in the salt, crack closure and healing in the DRZ will be rapid.

In Situ Seal Tests. Tests at the WIPP known as Small-Scale Seal Performance Tests (SSSPTs) have shown that large-diameter borehole seals constructed of bentonite and concrete provide nearly impermeable barriers to fluid flow. These seals were emplaced in boreholes drilled into the ribs and floor of a 5.5-m-square room. Thus the boreholes were drilled into a DRZ surrounding the room, and the borehole created a supplementary DRZ around itself. The time lapse between drilling the borehole and emplacing the seal was several months, so ample time was allowed for the DRZ to develop. Testing of the borehole seals 9 years after emplacement revealed no leakage through the DRZ. The DRZ must therefore have been healed because the borehole seal caused a stress state to reestablish that was conducive to healing.

Bulkheads in Salt and Potash Mines. The Rocanville potash mine in Saskatchewan provides one compelling case history for healing of a salt DRZ. An exploratory drift in the mine entered a barren salt zone (devoid of sylvite, so the surrounding rock was halite) and sustained a brine inflow. Within about a month, a concrete bulkhead was built in the drift, including construction grouting of the interface between the bulkhead and the salt. After sealing the drift, the brine pressure behind the bulkhead reached a near hydrostatic pressure greater than 8 MPa and remained at that pressure for more than 10 years. There is no evidence of leakage through either the bulkhead or the salt DRZ surrounding the drift. Although the drift was blocked at an early age, a DRZ must have formed instantaneously with the excavation of the drift. To be consistent with the observations, this DRZ must have been healed to avoid leakage during a 10-year time span. This bulkhead remains accessible and continues to function perfectly.

D5.2 Disturbed Rock Zone Analyses

D5.2.1 Analysis of the Disturbed Rock Zone in Salado Salt

Objective

The objective of this calculation was to determine the spatial extent of the DRZ in the intact salt surrounding the shaft for each of the four shaft seal materials (i.e., concrete, crushed salt, compacted clay, and asphalt). This information was used to define the input parameters to the fluid-flow calculations reported in Section 8 of the main report.

Problem Description

The radial extent of the DRZ within the intact salt was determined using a series of "pineapple-slice" models. Each model corresponds to a depth (and its associated initial temperature and stress conditions). Figure D-11 shows the schematic model geometry, which includes an axisymmetric representation of the shaft and surrounding host rock at a fixed depth. The outer (right) boundary is located 50 shaft radii from the axis of symmetry, the shaft centerline. The boundary condition at the outer boundary is maintained at the initial stress magnitude, i.e., the lithostatic stress.

Five depths were chosen to be representative of conditions along the length of the shaft within the Salado Formation. Specifically, depths of 250, 350, 450, 550, and 650 m were considered in this analysis. The initial stress and temperature conditions for these depths were determined as shown by the notes to Table D-17. Four moduli of elasticity were considered to approximate the seal materials of asphalt, compacted clay, crushed salt, and salt-saturated concrete. Five depths are considered adequate to determine a functional relationship between the DRZ radial extent and depth for each seal material type.

In the analysis for times $t < 0$ year, the shaft is not present, and an initial lithostatic stress field exists in the salt. At time $t = 0$ year, the cylindrical shaft is excavated, and the surrounding salt is allowed to creep for 50 years, i.e., the operational period. At time $t = 50$ years, the shaft is sealed. In the analyses, salt surrounding the shaft continues to creep against the seal material and consolidates the seal material (if applicable) for an additional 100 years. The time-dependent radial extent of the DRZ was calculated for each model (depth) and seal material-type. The damage-stress criterion for argillaceous salt (see Section D3.3.2) was used to estimate the spatial extent of the DRZ as a function of time for each of the models considered.

Assumptions

- The stratigraphy surrounding the AIS is modeled as being entirely argillaceous salt.
- The initial stress state prior to excavation is lithostatic.
- The modeled region remains isothermal.

- The shaft excavation and seal material emplacement are performed instantaneously at times of 0 and 50 years, respectively.
- The shaft is sufficiently isolated from other excavations so that only the shaft is considered in the analysis. Axisymmetric conditions are, therefore, applicable and a condition of plane strain exists with respect to the axial (vertical) direction.
- The calculations are based on finite deformation solutions.
- The damage stress criterion can be used to define the spatial extent of the DRZ.
- Short-term thermally enhanced salt creep is ignored.
- Pore pressure effects are not incorporated.
- A Tresca flow rule was used for intact salt.

Results

The results of this calculation are shown in Figures D-19 through D-23 in terms of the normalized DRZ radius as a function of backfill stiffness (i.e., elastic modulus) at various depths within the Salado Formation at times 0, 10, 25, 50, and 100 years after emplacement, respectively. The normalized DRZ radius is defined as the ratio of the radius to the DRZ boundary and the shaft radius. The radius to the DRZ boundary is defined as the location where the damage stress (Equation D-54) is equal to zero. For all backfill types, the most conservative (i.e., largest) estimate of the extent of the DRZ was calculated using the minimum value of the material's stiffness.

The concrete seals are located at approximate depths of 301, 420, and 608 m. An elastic modulus of 30 GPa was used for concrete, corresponding to the 28-day stiffness according to Equation D-4. Using the results shown in Figures D-19 through D-23, the normalized DRZ radii surrounding the three concrete seals are summarized in Table D-18 for times of 0, 10, 25, 50, and 100 years after emplacement.

The compacted-salt column is located at depths ranging from 420 to 600 m. A minimum elastic modulus of 7.5 GPa was used for compacted crushed salt, corresponding to the emplaced fractional density of 90% using Equation D-7. Using the results shown in Figures D-19 through D-23, the normalized DRZ radii surrounding the compacted crushed salt seal are summarized in Table D-19 at the top (429 m), middle (515 m), and bottom (600 m) of the column at times 0, 10, 25, 50, and 100 years following emplacment.

Compacted clay is used as a shaft seal in two locations within the Salado Formation. The upper Salado compacted clay column is located at depths between 307 and 413 m. The lower Salado compacted clay column is located at depths between 617 and 643 m. An elastic modulus of 1.2 GPa was assumed for compacted clay, corresponding to a fractional density of 90% according to Equation D-18. Using the results shown in Figures D-19 through D-23, the normalized DRZ radii surrounding the compacted clay seals are summarized in Table D-20 at the top and bottom of the upper and lower Salado compacted clay columns at times 0, 10, 25, 50, and 100 years following emplacement.

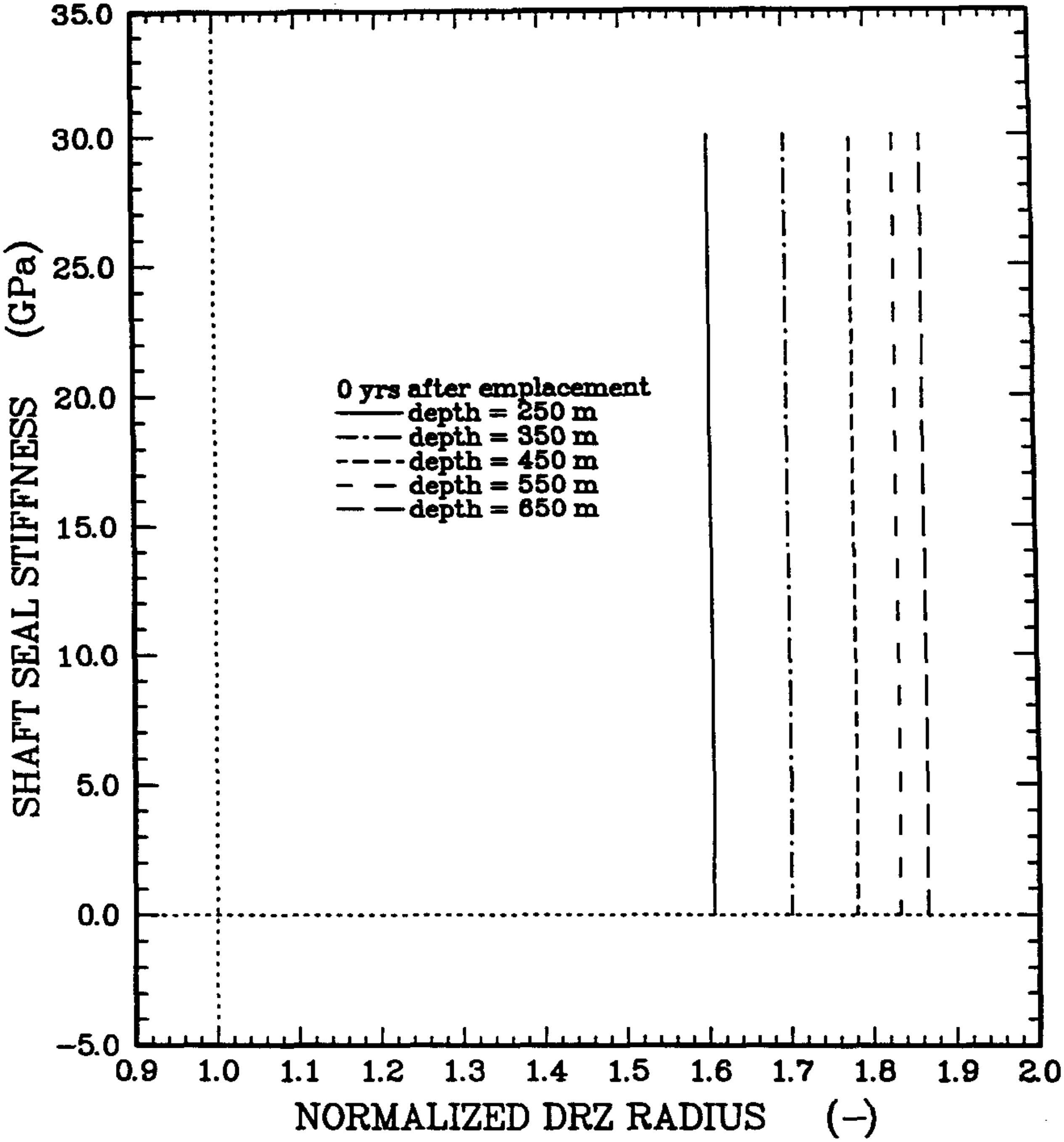

Figure D-19. Normalized DRZ radius as a function of shaft seal stiffness at various depths within the Salado Formation at time = 0 year after emplacement.

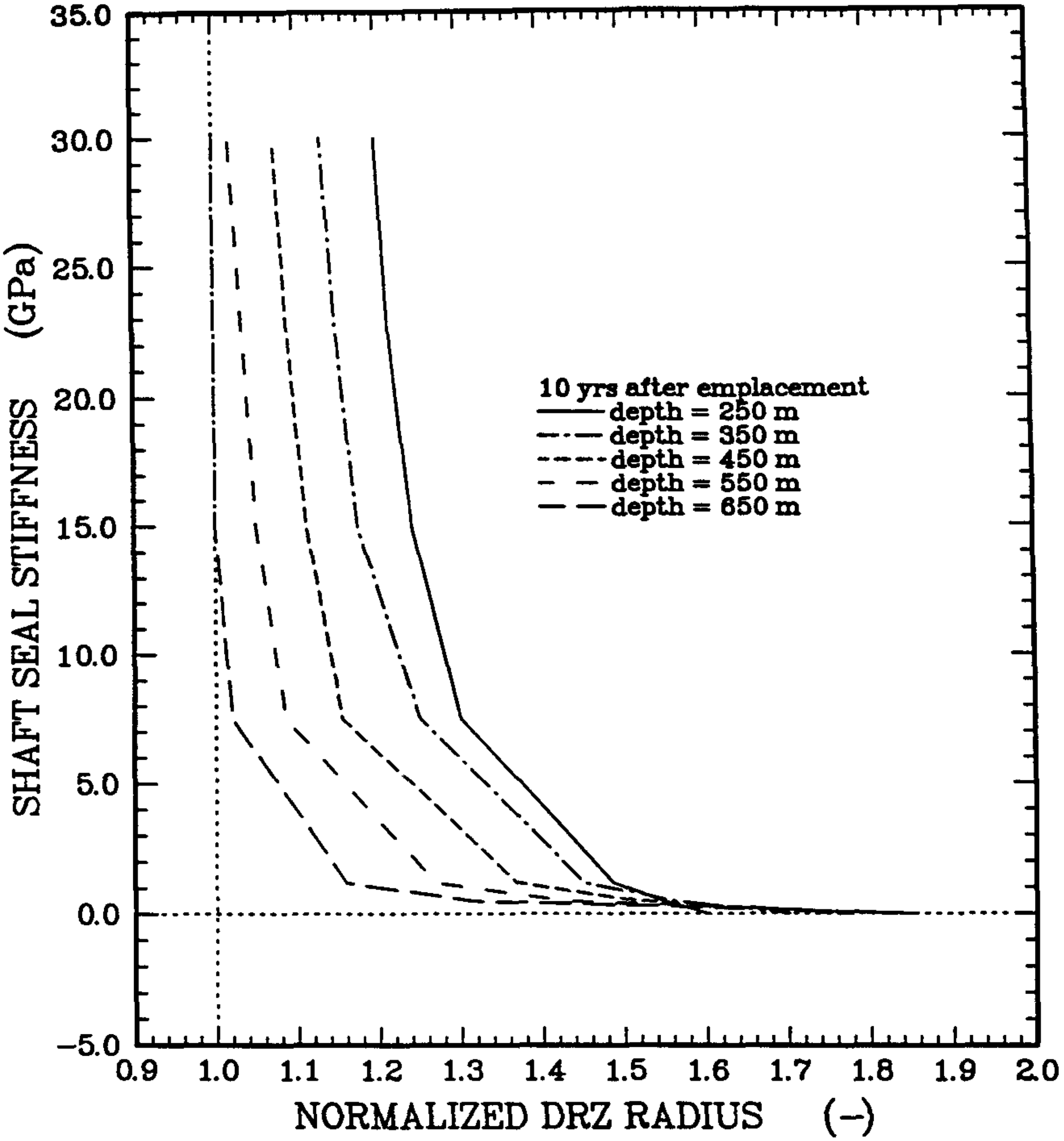

Figure D-20. Normalized DRZ radius as a function of shaft seal stiffness at various depths within the Salado Formation at time = 10 years after emplacement.

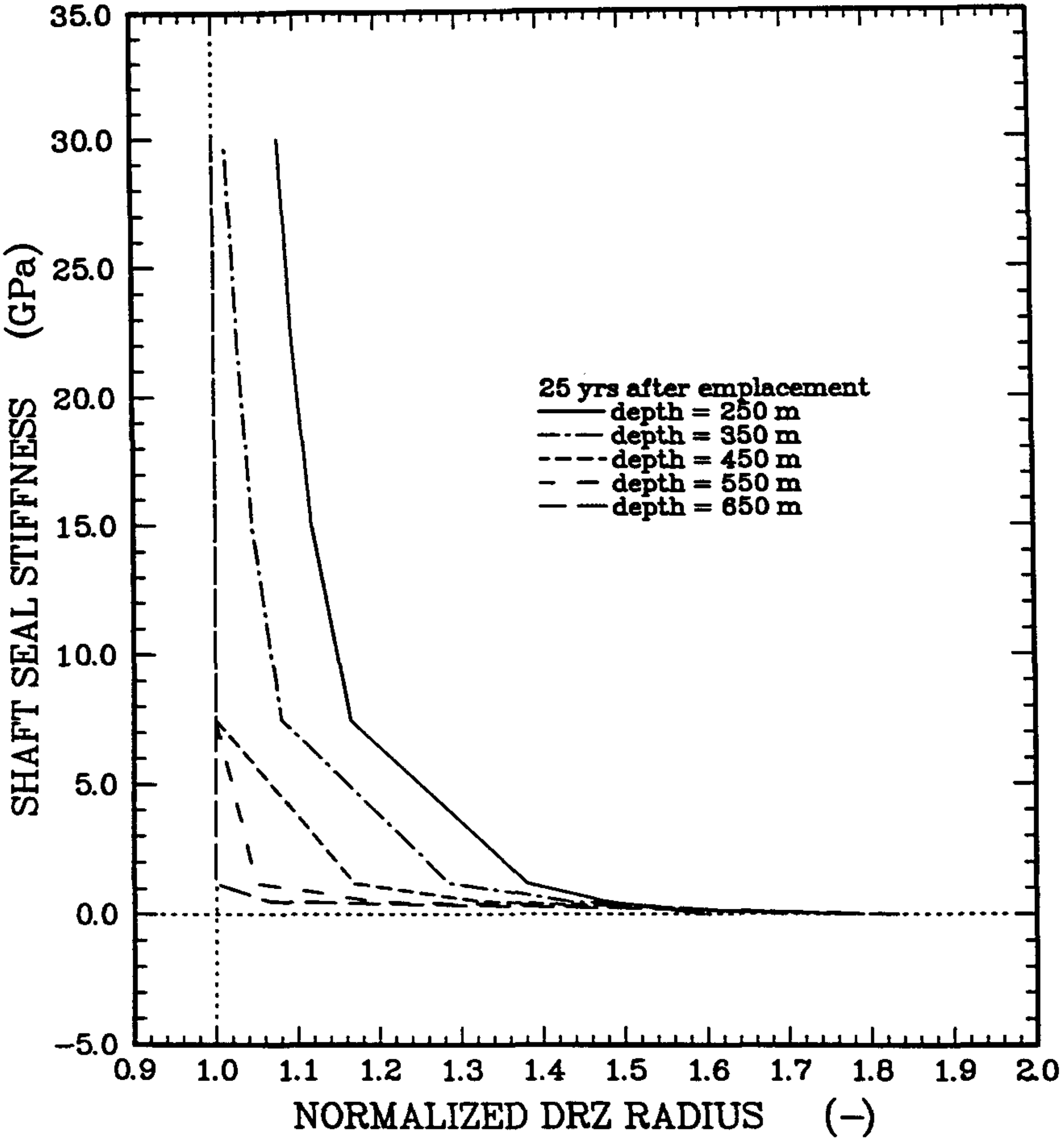

Figure D-21. Normalized DRZ radius as a function of shaft seal stiffness at various depths within the Salado Formation at time = 25 years after emplacement.

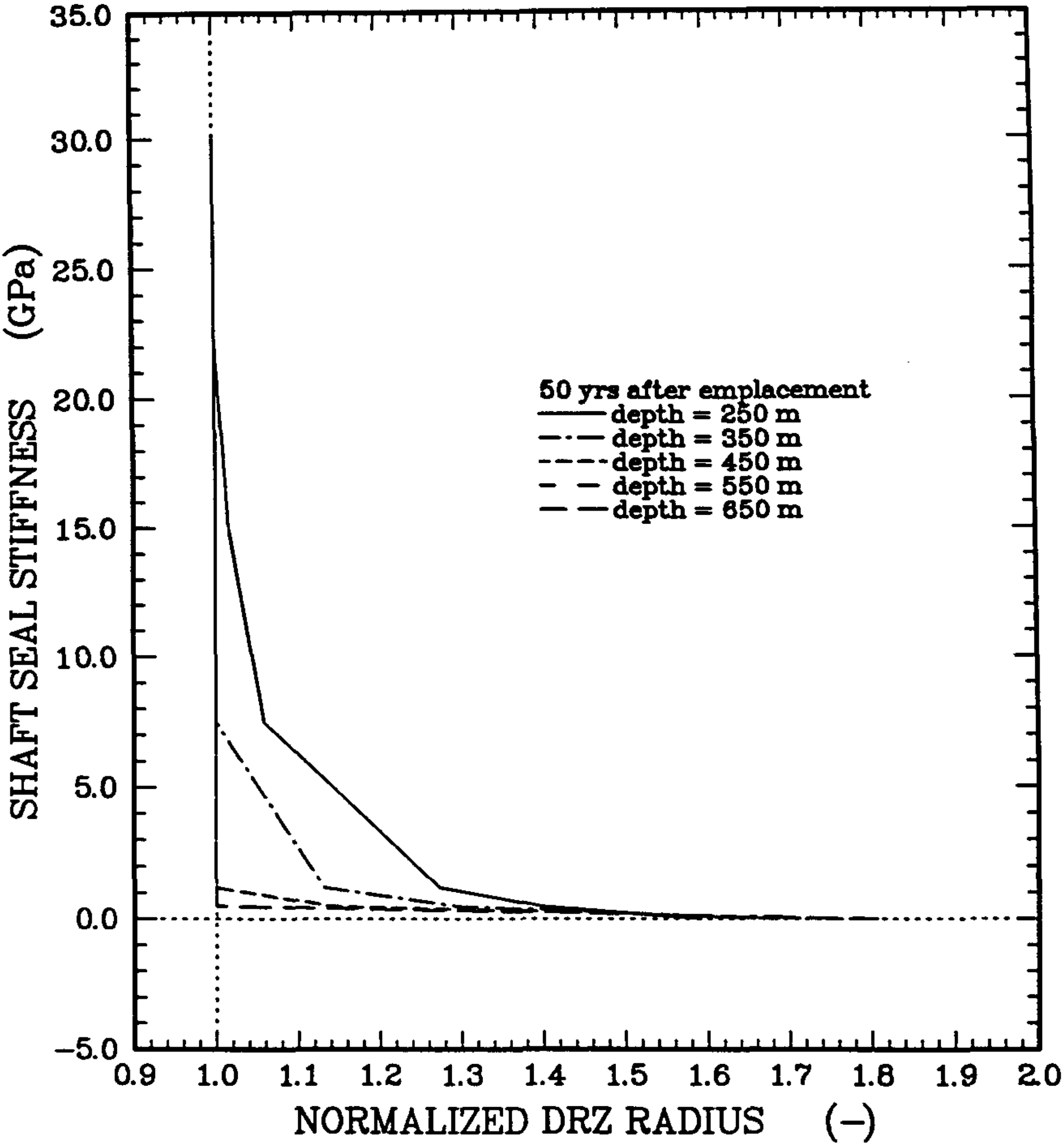

Figure D-22. Normalized DRZ radius as a function of shaft seal stiffness at various depths within the Salado Formation at time = 50 years after emplacement.

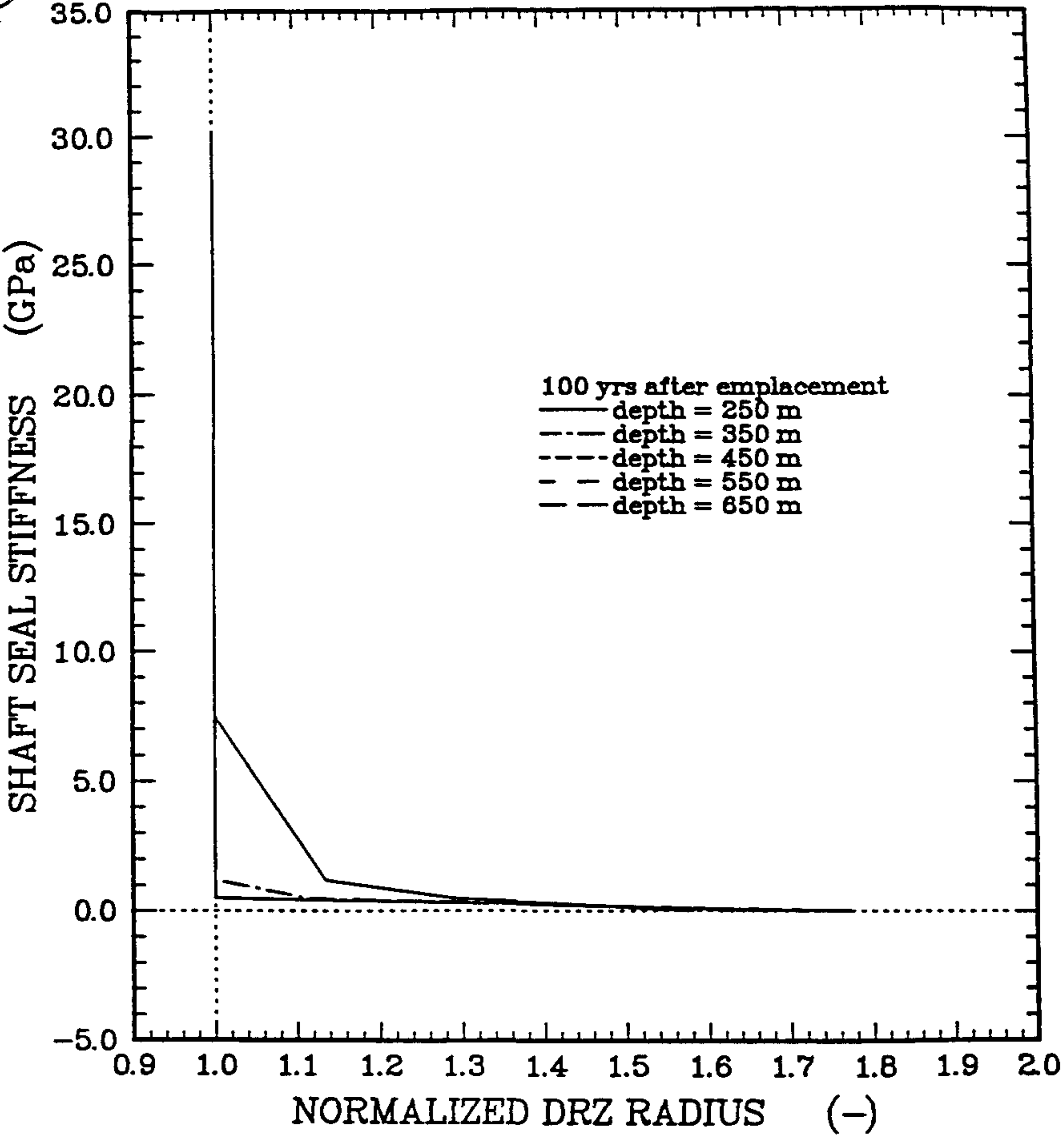

Figure D-23. Normalized DRZ radius as a function of shaft seal stiffness at various depths within the Salado Formation at time = 100 years after emplacement.

Table D-18. Normalized DRZ Radius—Concrete

Concrete Component	**Time After Emplacement (yrs)**				
	0	10	25	50	100
Upper (d = 301 m)	1.65	1.16	1.05	1.00	1.00
Middle (d = 421 m)	1.76	1.09	1.01	1.00	1.00
Lower (d = 608 m)	1.85	1.01	1.00	1.00	1.00

Table D-19. Normalized DRZ Radius—Crushed Salt

Depth	**Time After Emplacement (yrs)**				
	0	10	25	50	100
Upper (d = 429 m)	1.77	1.20	1.02	1.00	1.00
Middle (d = 510 m)	1.82	1.11	1.01	1.00	1.00
Lower (d = 600 m)	1.85	1.05	1.00	1.00	1.00

Table D-20. Normalized DRZ Radius—Compacted Clay

Depth	**Time After Emplacement (yrs)**				
	0	10	25	50	100
Top of USCCC (d = 308 m)	1.66	1.47	1.32	1.19	1.06
Bottom of USCCC (d = 413 m)	1.75	1.40	1.21	1.05	1.00
Top of LSCCC (d = 616 m)	1.85	1.22	1.03	1.00	1.00
Bottom of LSCCC (d = 643 m)	1.86	1.20	1.02	1.00	1.00

USCCC = upper Salado compacted clay column; LSCCC = lower Salado compacted clay column.

Asphalt is used as a shaft seal material from the Rustler/Salado interface to the top of the upper concrete component (depths between 256 and 293 m). A minimum elastic modulus of 0 GPa was assumed for asphalt, corresponding to its unsolidified stiffness.

Using the results shown in Figures D-19 through D-23, the normalized DRZ radii surrounding the asphalt seal are summarized in Table D-21 at the top and bottom of the column at times 0, 10, 25, 50, and 100 years after emplacement.

Table D-21. Normalized DRZ Radius—Asphalt

Depth	**Time After Emplacement (yrs)**				
	0	10	25	50	100
Top (d = 256 m)	1.61	1.61	1.60	1.59	1.58
Bottom (d = 293 m)	1.65	1.65	1.64	1.63	1.62

D5.2.2 Salado Anhydrite Beds

The material behavior of the interbeds within the Salado Formation is assumed to be elastic (time-invariant); in contrast, the salt creeps (time-dependent). Therefore the interbeds will tend to inhibit creep closure of the shaft. In addition, the salt creep that does occur will tend to increase the potential for fracturing within the interbeds because of shear tractions that develop along the interface. The thickness of the interbeds relative to the thickness of the salt above and below the interbeds determines which of the two behaviors will dominate. That is, the thicker the interbeds, the less salt creep will occur; and the thicker the salt bed layer, the greater the potential for fracturing the interbeds.

Objective

The objective of this calculation is to determine the extent of the DRZ within the Salado anhydrite and polyhalite interbeds as a result of the creep of the surrounding salt. The definition of the DRZ within these interbeds was used in the fluid-flow consolidations reported in Appendix C.

Problem Description

The problem description and assumptions used in performing this calculation are the same as those presented in Section D4.1.2. The marker bed locations relative to the concrete seal components are shown in Figures D-7 and D-9. The deformational and strength properties of the anhydrite and polyhalite materials are given in Table D-15.

Results

The results are summarized in Figures D-24 and D-25, which show a calculated factor of safety against failure for the various anhydrite and polyhalite layers as a function of radial distance from the shaft after the shaft has been left open for 50 years.

For all interbeds, the factor of safety increases as the distance from the shaft wall increases. Further, with the exception of MB117, the factor of safety is greater than one (no DRZ) for all interbeds. For MB117, the failure (DRZ) is localized to within 1 m of the shaft wall.

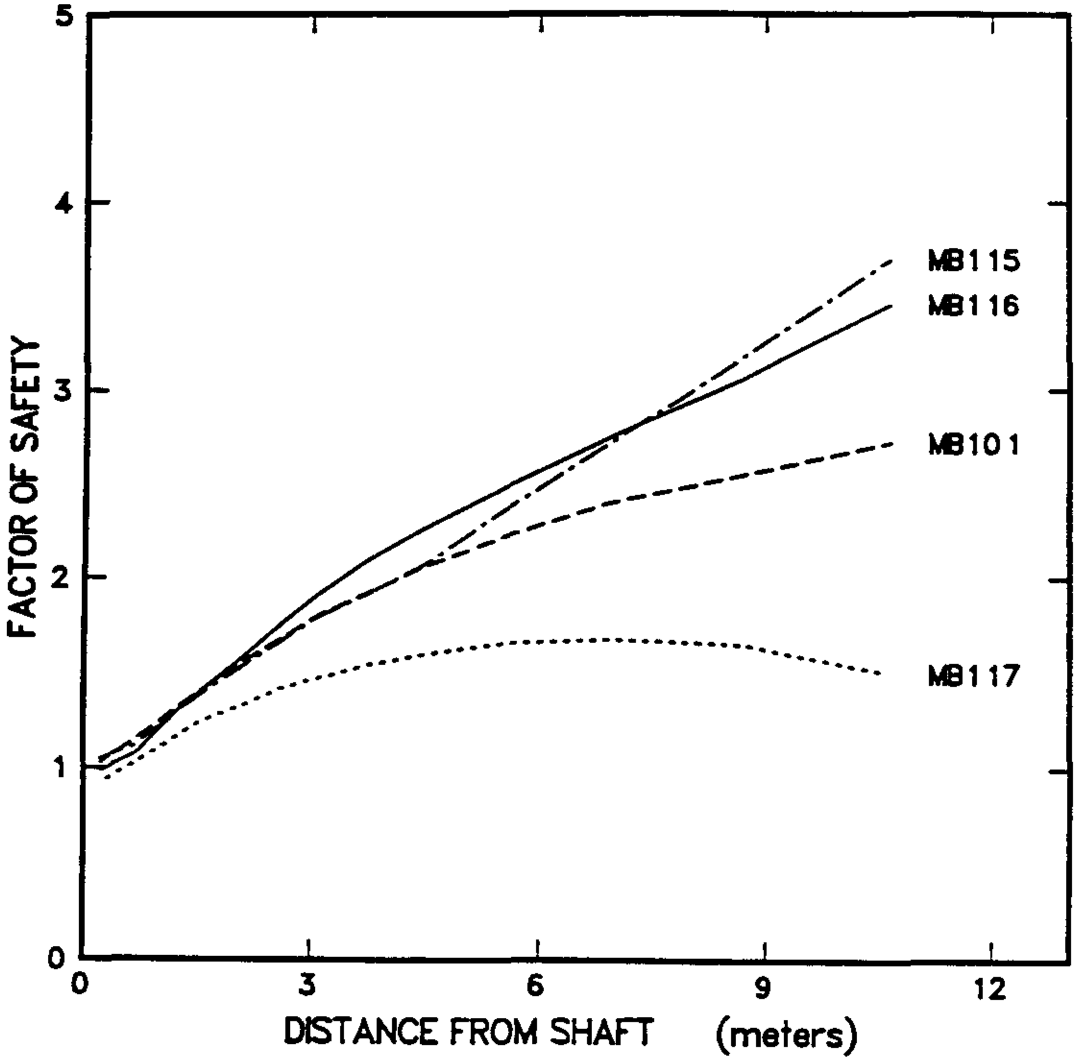

Figure D-24. Factor of safety in polyhalite beds at 50 years.

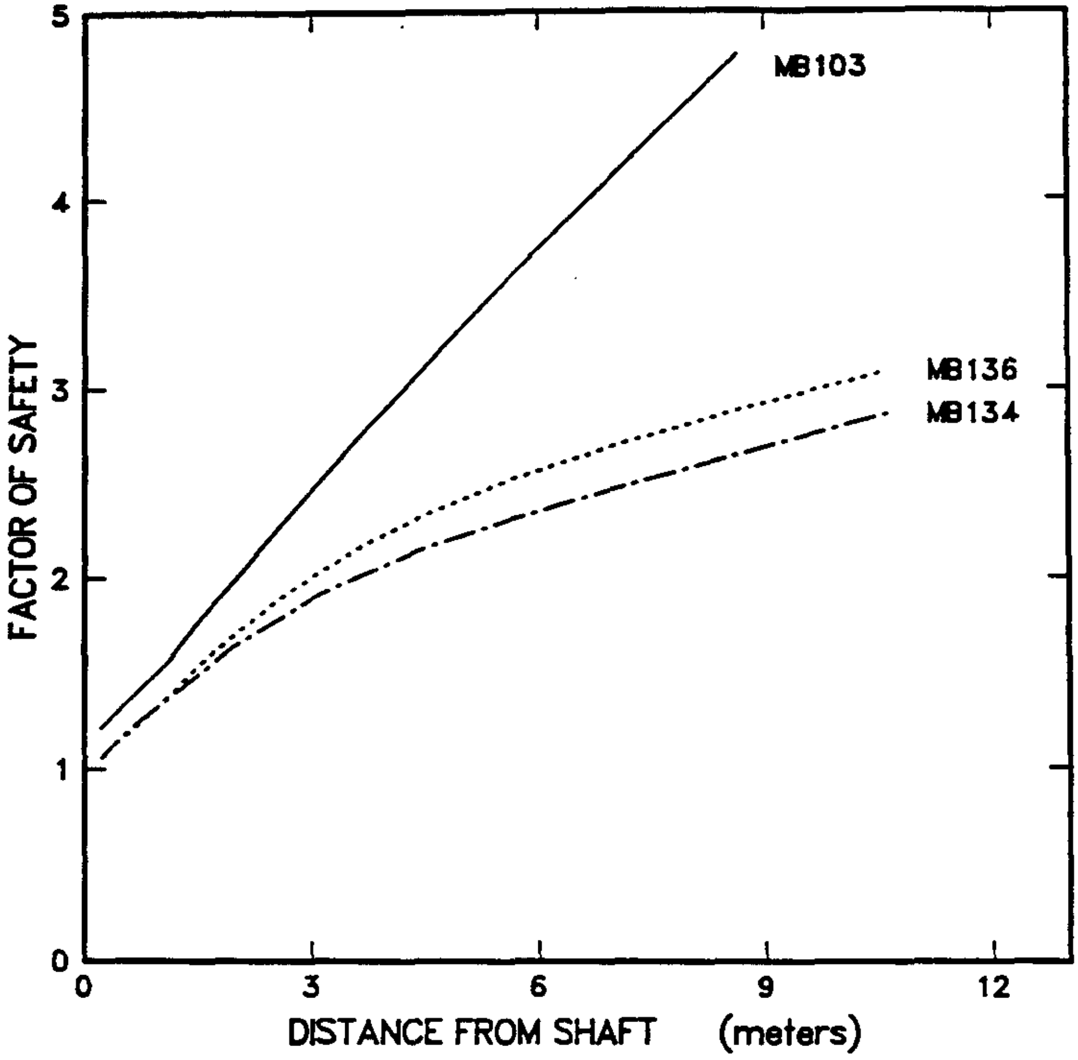

Figure D-25. Factor of safety in anhydrite beds at 50 years.

D5.2.3 Near Surface and Rustler Formations

The DRZ around a circular opening (such as a shaft) was estimated using analytical means. The extent of the DRZ in the formations above the Salado was calculated based on two criteria for rock failure. The shaft excavation superimposes an increment of damage or disturbance on any natural preexisting disturbance in the host rock. In the near-surface and Rustler formations at the WIPP, the development of the DRZ is assumed to be time-invariant; rock behavior is observed to be elastic.

Objective

The objective of this calculation is to determine the extent of the DRZ surrounding the shafts in the near-surface and Rustler formations. The rock types that compose these formations are anhydrite, dolomite, and mudstone and exhibit time-invariant behavior.

Problem Description

The rock surrounding the shafts can be divided into two regions: the DRZ region in which the rock fails (plastic region) and a region that behaves elastically. The geometry of the regions is defined as:

$$\begin{aligned} &\text{DRZ region:} \quad a \le r \le R \\ &\text{Elastic region:} \quad R \le r \le \infty \end{aligned} \qquad \text{(D-62)}$$

where a is the shaft radius and R is the radius to the interface between the plastic and elastic regions. The radius R can be calculated so that the radial stress distribution is continuous across the interface and satisfies the boundary conditions at the shaft wall and the far field. Similarly, stress distributions in the plastic zone are assumed to just satisfy the failure criterion.

The Coulomb failure criterion accounts for the beneficial effect of confinement and says failures occur whenever:

$$\begin{aligned} &\sigma_1 - \sigma_3 \ge C_0 + \sigma_3(\tan\beta - 1) \\ &\tan\beta = \frac{1+\sin\phi}{1-\sin\phi} \end{aligned} \qquad \text{(D-63)}$$

where ϕ is the angle of internal friction (Table D-16). The radius to the elastic/plastic interface based on the Coulomb failure criterion (Ladanyi, 1974) is:

$$\text{Coulomb:} \quad R/a = \left[\frac{P_0 + T_0 - mC_0}{T_0}\right]^{1/(\tan\beta - 1)} \qquad \text{(D-64)}$$

where:

P_0 = far-field stress magnitude

T_0 = tensile strength = $S_0 / \tan\phi$ (Table D-15)

C_0 = cohesion (Table D-15).

Because of scale effects, rock is seldom as strong in situ as laboratory strength tests indicate. This scale effect is shown, for example, by Goodman (1980), who suggests a factor of safety (strength reduction factor) of five for foundation designs. The in situ strength of the rock was determined by reducing the matrix strength (based on a literature survey of laboratory tested strengths) by a factor ranging from three to five. To span the uncertainty in the horizontal stress magnitude, the in situ (far-field) stress was taken to be a multiple of between one to two times the vertical stress. The intermediate value for each parameter was used as the likely parameter value for southeastern New Mexico. These parameters should result in a conservative estimate of the DRZ within these formations.

Results

The results of this calculation are shown in Figure D-26, which shows the radial extent of the DRZ as a function of depth. These results indicate that the DRZ is not present at depths less than 50 m and for the depth interval from 165 m to 213 m (principally, an anhydrite and dolomite interval). For the mudstones between 50 and 165 m and between 223 and 260 m, the radial extent of the DRZ increases with depth, reaching a maximum of 2.6 shaft radii at a depth of 260 m. The results of this analysis were used to define the initial conditions to the fluid-flow calculations predicted in Section 8.

D6. OTHER ANALYSES

This section discusses two supplementary analyses performed to support the shaft seal design: (1) the DRZ created by asphalt waterstops and (2) potential benefits from shaft station backfilling.

D6.1 Asphalt Waterstops

The DRZ is potentially a major contributor to fluid flows past a shaft seal, regardless of which seal materials are emplaced within the shaft. Therefore, to increase the confidence in the overall shaft seal system, low permeability layers (termed radial waterstops) intersect the DRZ surrounding the shaft to impede fluid flow. These waterstops are emplaced to alter the flow direction either inward toward the shaft seal or outward toward the intact salt. The waterstop effectively blocks the full cross section of the shaft and DRZ using a virtually impermeable material (asphalt). The waterstop is thin so that its height is small relative to its width (radius); a small ratio between height and width will concentrate the new DRZ at the edge of the waterstop. The extent of the new DRZ is small, so the area for fluid leakage past the waterstop is also small.

Objectives

The objectives of this calculation were (1) to estimate the additional damage introduced by excavating the radial slot in the shaft wall and (2) to analyze the potential for healing this induced DRZ.

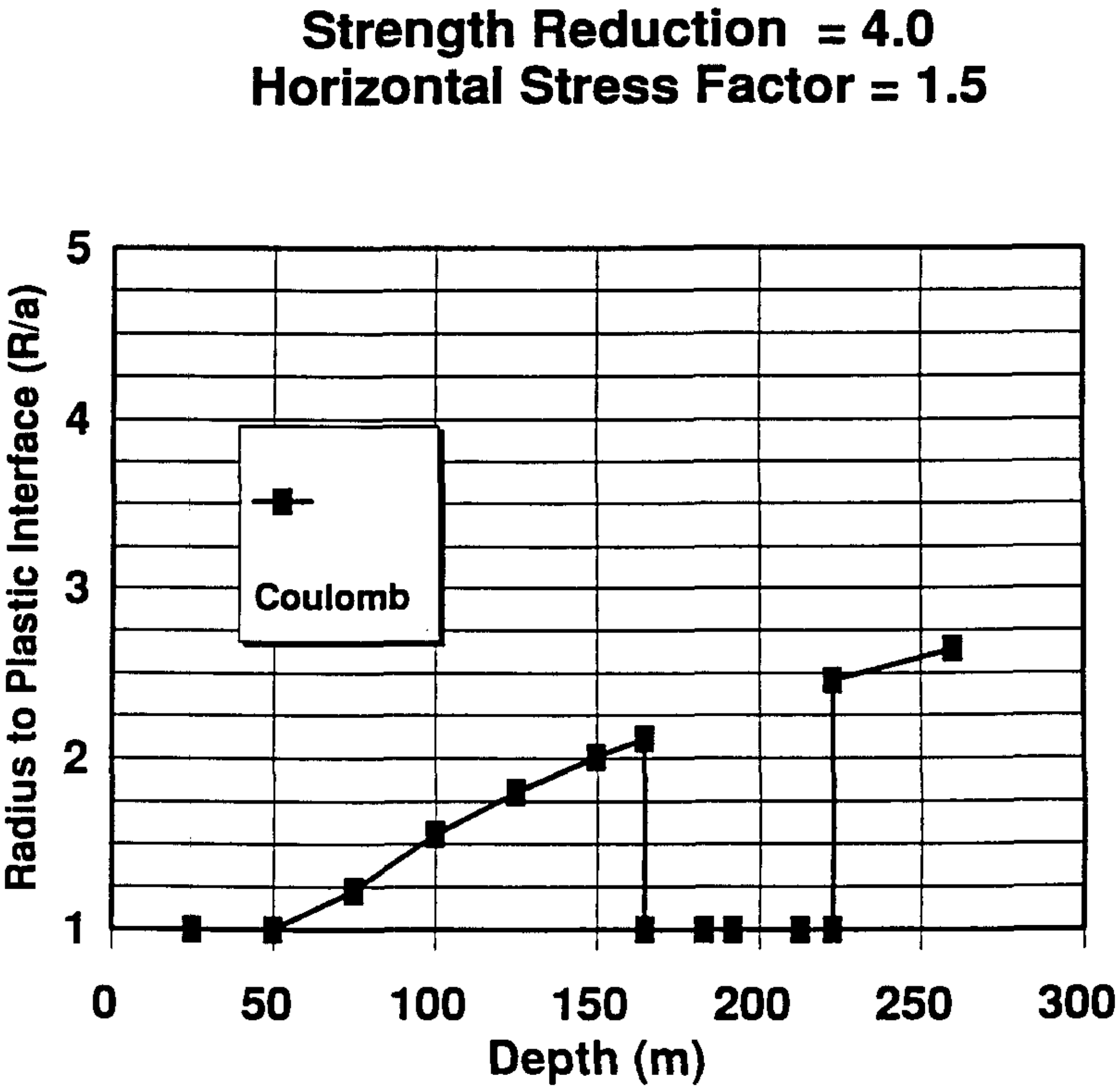

Figure D-26. Normalized DRZ radius for strength reduction factor of 4 and horizontal stress factor of 1.5.

Problem Description

The problem description and assumptions used in performing this calculation are the same as those presented in Section 4.1.2. The damage-stress criterion was used to indicate the spatial extent of the DRZ; i.e., zones with positive damage stress were assumed to be damaged and zones with negative damage stress were assumed to be either undamaged or healed. The rate of healing was assumed to be instantaneous; i.e., zones where the damage stress changed from positive to negative were assumed to be healed immediately.

Results

The results from analysis of the lower concrete component waterstop are presented here; the structural behavior of the other two waterstops is similar. Figures D-27, D-28, and D-29 show contours of damage stress surrounding the lower concrete component waterstop just before excavation of the waterstop, immediately after excavation, and 20 years after emplacement of the asphalt and concrete seals. Figure D-27 indicates that the DRZ before excavating the waterstop is contained spatially within the salt to a radial distance of less than one shaft radius (about 3 m). Figure D-28 indicates that the DRZ extends radially to approximately 1.4 shaft radii (4.3 m) into the salt as a result of the waterstop excavation. This extension of the DRZ is localized within the span of the concrete seals and approaches the waterstop kerf edge. The results shown in Figure D-29 indicate that the DRZ has reduced substantially in size as a result of emplacement of the concrete and asphalt seals and 20 years creep of the surrounding salt. After 20 years, the spatial extent of the DRZ is localized near the asphalt/concrete interface, extending spatially into the salt a distance of less than 2 m. For input to the fluid-flow calculations, a time of 2 years was estimated for the asphalt waterstop to become effective in terms of sealing off flow through the DRZ.

D6.2 Shaft Pillar Backfilling

The underground portion of the WIPP is quite small when compared to most salt and potash mines. Nonetheless, subsidence will occur as the underground openings close because of creep in the salt. The amount of subsidence depends on the volume of space remaining in the repository at the time of closure. The volume of space (void) will consist of empty access drifts, backfilled entries, and filled waste rooms. The waste rooms are expected to have a 63.8% porosity after accounting for the voids in the waste containers, voids between containers, and headspace in the room (Callahan and DeVries, 1991). Similarly, backfilled entries are expected to retain a porosity of about 40% following mechanical placement of salt backfill (backfill fractional density of 0.6). Subsidence of the ground around the shafts could conceivably disturb the shaft seals. Backfilling the entries in the shaft pillar would reduce the eventual subsidence.

Objective

The objective of this calculation was to assess the benefits of backfilling the shaft pillar in terms of reducing the subsidence of the shaft seal and therefore decreasing the potential for differential settlement within the seal.

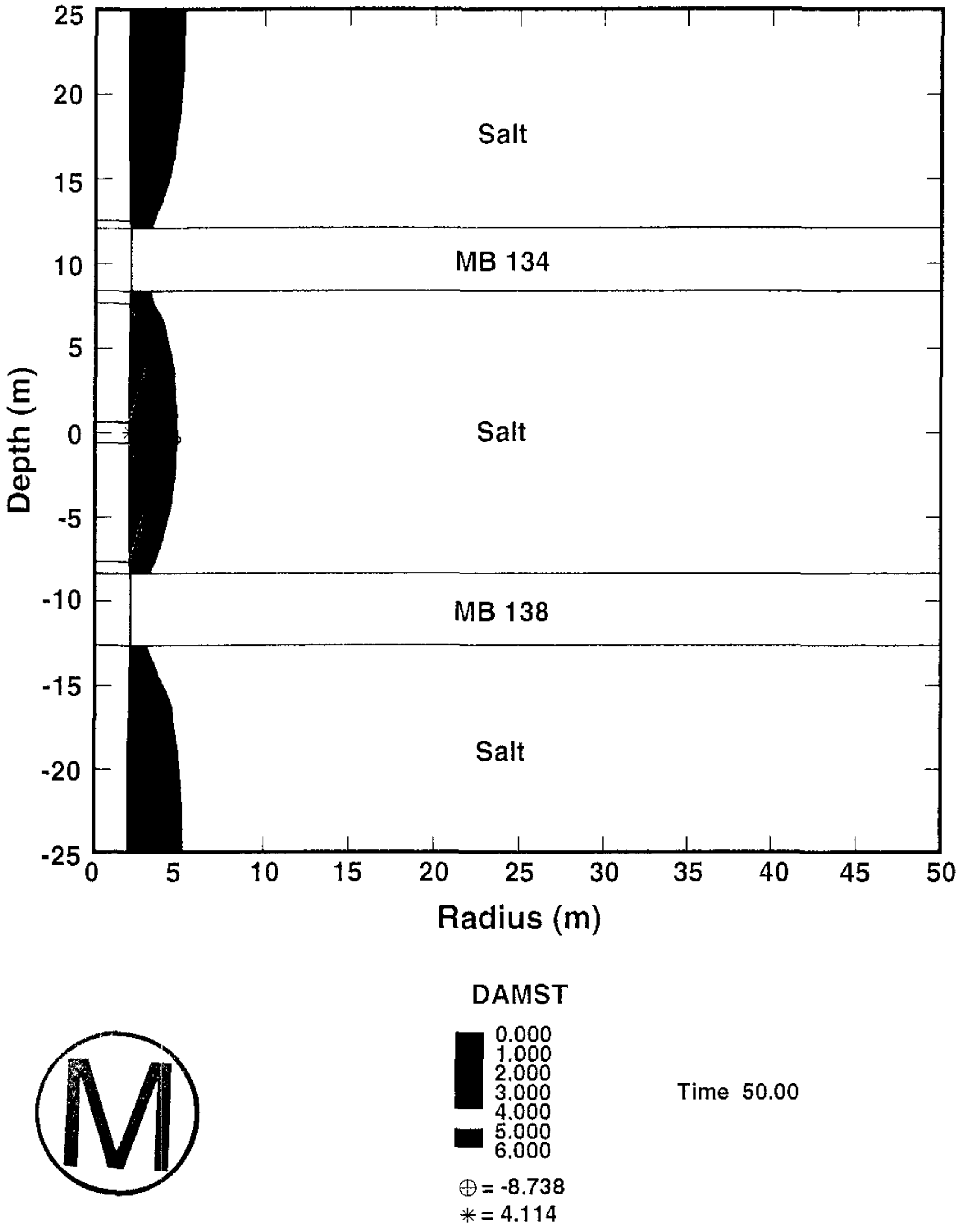

Figure D-27. Salt DRZ around the lower shaft seal at 50 years (prior to seal construction).

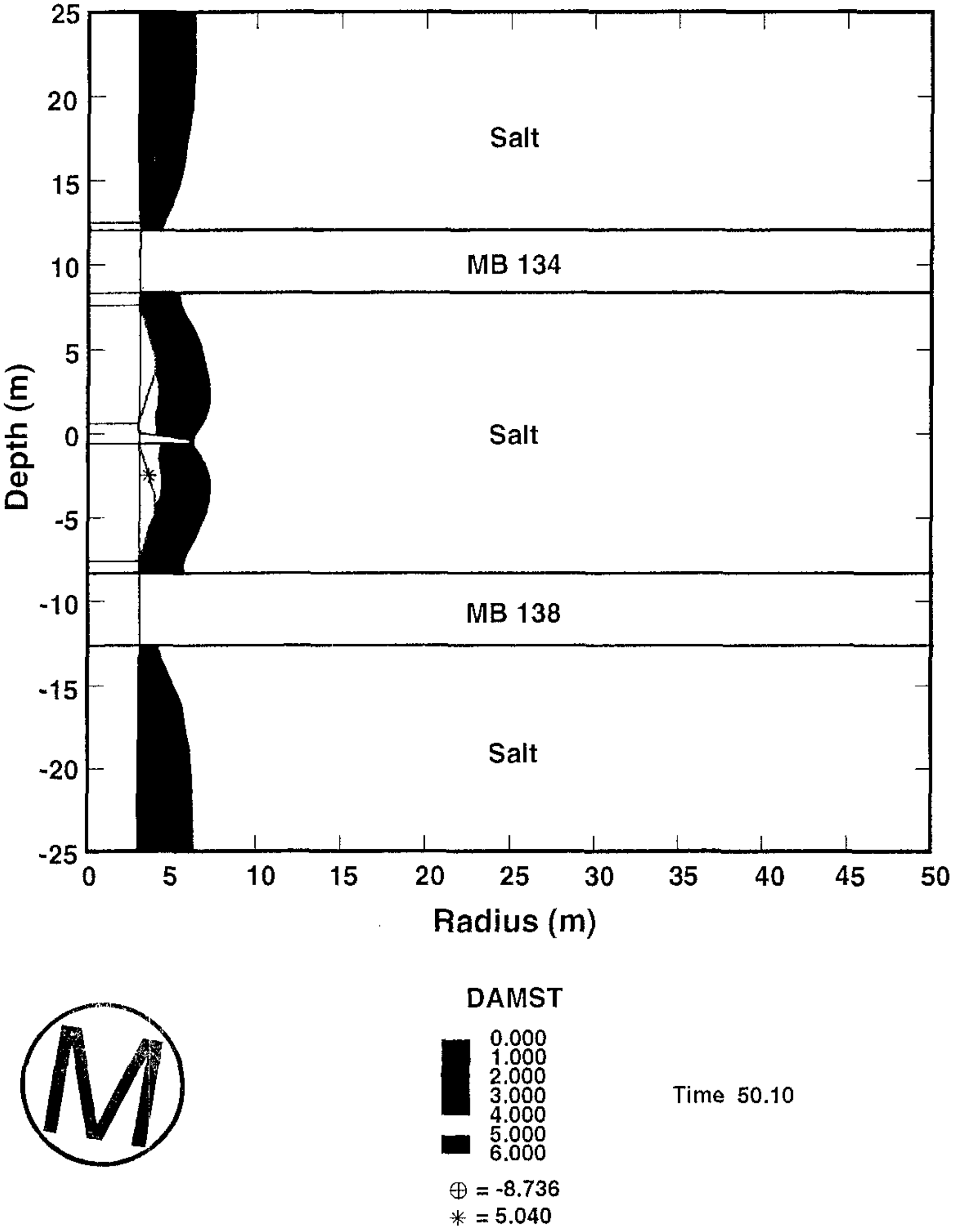

Figure D-28. Salt DRZ around the lower shaft seal at 50.1 years (after excavations but before seal construction).

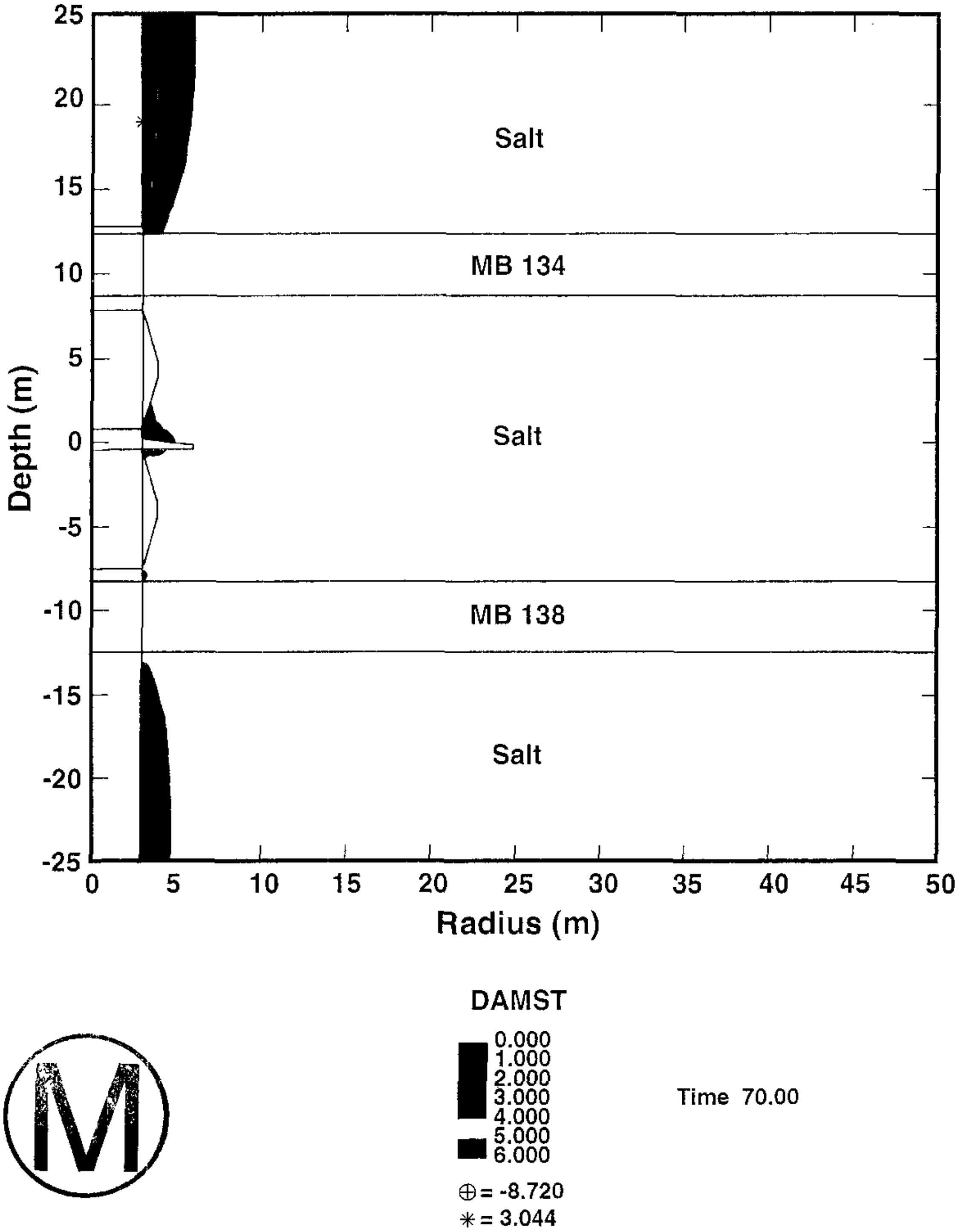

Figure D-29. Salt DRZ around the lower shaft seal at 20 years after seal construction.

Problem Description

The subsidence analysis for this calculation was performed using the computer program SALT_SUBSID, which is distributed by the Solution Mining Research Institute (Nieland, 1991). Mathematically, the numerical model is represented by:

$$S(x,y)=\sum_{j} F\left(x_{j},y_{j},D,A_{j},V_{j}\right) \tag{D-65}$$

where S is the ultimate subsidence at the x, y coordinates of a point on the surface after total closure of the underground openings. The function $F\ (x_j, y_j, D, A, V_j)$ describes the spatial variation of ultimate subsidence for individual mining areas with centers at x_j, y_j, at depth D, of rectangular area A_j, and volume V_j. The spatial function, F, is based on the displacement discontinuity solution for the surface displacement after the closure of a rectangular prismatic opening in an elastic half space. The theoretical basis for the function was obtained from papers by Davis (1983).

The primary input to SALT_SUBSID is the underground opening geometries. The coordinates of the entries and rooms were taken from an AutoCad rendering of the WIPP site. The mining blocks used as input to the analysis are shown in Figure D-30. (The representation is sufficiently accurate for purposes of this calculation but not accurate to the extent that the individual coordinates can be relied on for any other purposes.)

Eight panels of waste rooms were represented in the subsidence model. The height of the waste rooms was set to 8.29 ft based on an excavated height of 13 ft and a filled waste-room porosity of 63.8%. The waste rooms are close enough to affect the surface subsidence at the shaft collars; they probably are not close enough to affect subsurface subsidence at the shaft seal locations.

Two backfilled areas were considered: backfilled areas of either 200 or 300-ft radius around each of the four shafts. To account for backfilling, the entry height was adjusted for any portion of the entries within the circular area around each shaft. The adjusted height was 4.33 ft based on an assumed backfill porosity of 30% and a nominal 1-ft headspace for the originally 12-ft-tall entries. For each scenario, the ultimate subsidence was calculated. This subsidence results from total closure of the shaft pillar workings.

Results

The ultimate subsidence was calculated for the three scenarios: no backfill in the shaft area, 61-m (200-ft) radius backfilled areas, and 91-m (300-ft) radius backfilled areas around the shafts. Over the shaft area, the ultimate surface subsidence is about 0.15 m (0.5 ft) or less depending on the backfill situation. Figure D-31 shows profiles of the ultimate subsidence over the shaft area; the profile is north-to-south, centered on the salt-handling shaft. The ultimate surface subsidence in the shaft area is reduced from 0.15 m (0.5 ft) for the no backfill condition to 0.13 m (0.44 ft) and 0.12 m (0.41 ft) by backfilling to 61 m and 91 m radii, respectively. As a matter of interest, the maximum subsidence for WIPP is centered over the waste panel area with a magnitude of 0.26 m (0.85 ft). The restriction in subsidence is not considered to be enough that it warrants backfilling the shaft pillar area.

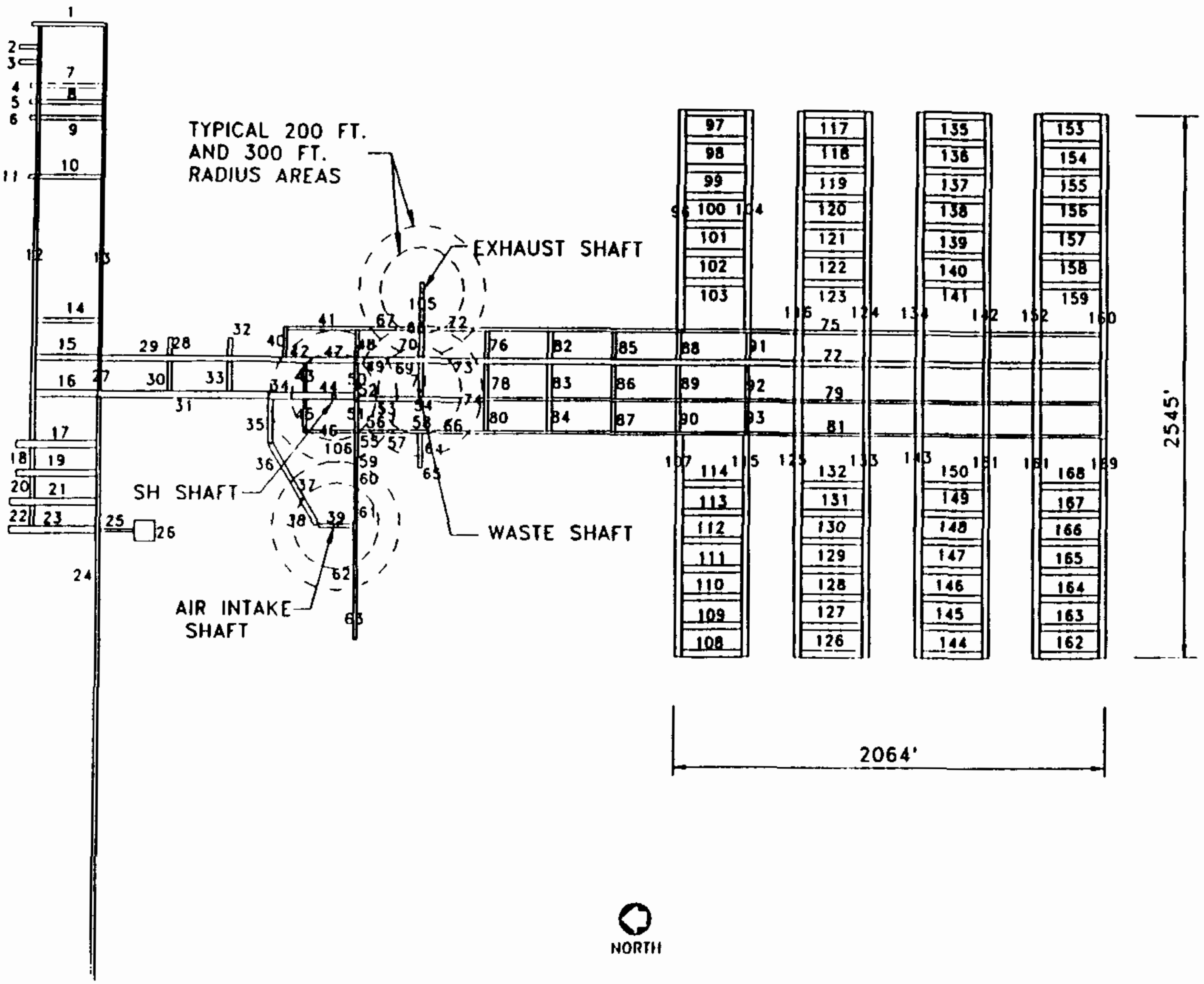

Figure D-30. Mining blocks used to represent WIPP underground workings.

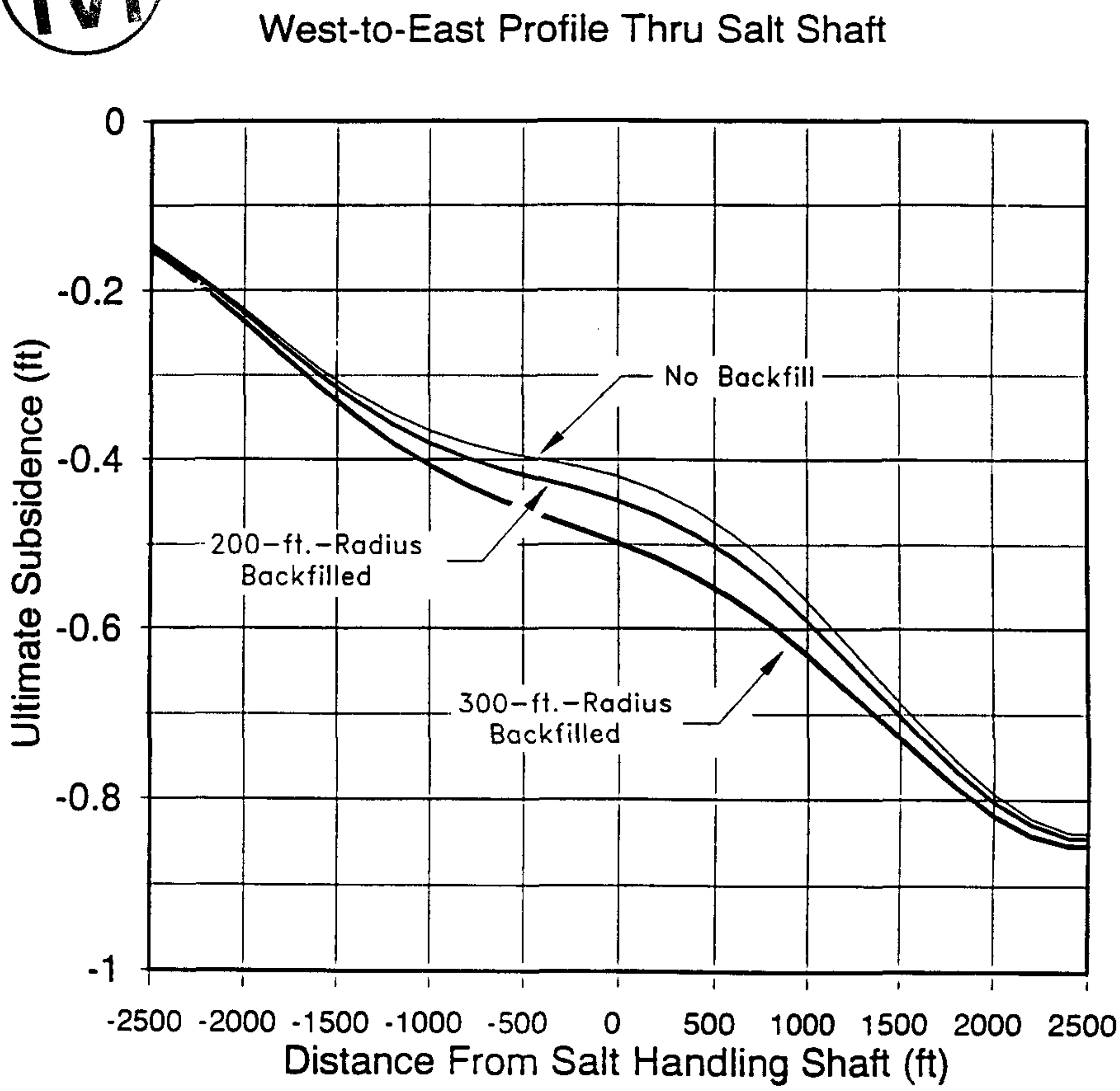

Figure D-31. Surface subsidence profiles over shaft area.

D7. REFERENCES

Andersen, P.J., M.E. Andersen, and D. Whiting. 1992. *A Guide to Evaluating Thermal Effects in Concrete Pavements.* SHRP-C/FR-92-101. Washington, DC: Strategic Highway Research Program, National Research Council.

ASTM D 4311 - 83 (R 1990). "Standard Practice for Determining Asphalt Volume Correction to a Base Temperature (R 1990)," *Annual Book of ASTM Standards, Volume 04.03, Road and Paving Materials; Pavement Management Technologies*. Philadelphia, PA: American Society for Testing and Materials. (Available from American Society for Testing and Materials, 1916 Race Street, Philadelphia, PA 19103-1187, 215/299-5400.)

Brodsky, N.S. 1990. *Crack Closure and Healing Studies in WIPP Salt Using Compressional Wave Velocity and Attenuation Measurements: Test Methods and Results*. SAND90-7076. Albuquerque, NM: Sandia National Laboratories. (Copy on file in the Sandia WIPP Central Files, Sandia National Laboratories, Albuquerque, NM [SWCF] as WPO25755.)

Brodsky, N.S., and D.E. Munson. 1994. "Thermomechanical Damage Recovery Parameters for Rocksalt From the Waste Isolation Pilot Plant, " *Rock Mechanics, Models and Measurements, Challenges from Industry: Proceedings of the 1st North American Rock Mechanics Symposium, University of Texas at Austin, Austin, TX, June 1-3, 1994*. Eds. P.P. Nelson and S.E. Laubach. Brookfield, VT: A.A. Balkema. 731-738. (Copy on file in the SWCF as WPO27175.)

Callahan, G.D. 1994. *SPECTROM-32: A Finite Element Thermomechanical Stress Analysis Program Version 4.06*. Topical Report RSI-0531. Rapid City, SD: RE/SPEC Inc. (Copy on file in the SWCF as WPO36814.)

Callahan, G.D., and K.L. DeVries. 1991. *Analyses of Backfilled Transuranic Wastes Disposal Rooms*. SAND91-7052. Albuquerque, NM: Sandia National Laboratories. (Copy on file in the SWCF as WPO23990.)

Callahan, G.D., M.C. Loken, L.L. Van Sambeek, R. Chen, T.W. Pfeifle, J.D. Nieland, and F.D. Hansen. 1995a. *Evaluation of Potential Crushed-Salt Constitutive Models*. SAND95-2143. Albuquerque, NM: Sandia National Laboratories. (Copy on file in the SWCF as WPO31068.)

Callahan, G.D., M.C. Loken, L.D. Hurtado, and F.D. Hansen. 1996. "Evaluation of Constitutive Models for Crushed Salt," *4th International Conference on the Mechanical Behavior of Salt, Montreal, Quebec, June 17-18, 1996*. SAND96-0791C. Albuquerque, NM: Sandia National Laboratories. (Copy on file in the SWCF as WPO36449.)

Chan, K.S. 1993. "Time Dependent Interface of Bed Separation Fracture Process in Bedded Natural Salt Deposits," *Monthly Technical Report No. FY 93-6*. Prepared by Southwest Research Institute, San Antonio, TX for Sandia National Laboratories, Albuquerque, NM. (Copy on file in SWCF as WPO21030.)

Chan, K.S. 1994a. "Further Development of Fracture Constitutive Model for Rock Salt," *Monthly Technical Report No. FY 93-12*. Prepared by Southwest Research Institute, San Antonio, TX, for Sandia National Laboratories, Albuquerque, NM, January 15, 1993[sic]. (Copy on file in the SWCF as WPO21086.)

Chan, K.S. 1994b. "Further Development of Fracture Constitutive Model for Rock Salt," *Monthly Technical Report No. FY 94-1*. Prepared by Southwest Research Institute, San Antonio, TX, for Sandia National Laboratories, Albuquerque, NM, February 14, 1993[sic]. (Copy on file in the SWCF as WPO21087.)

Chan, K.S., S.R. Bodner, A.F. Fossum, and D.E. Munson. 1992. "A Constitutive Model for Inelastic Flow and Damage Evolution in Solids Under Triaxial Compression," *Mechanics of Materials*. Vol. 14, no. 1, 1-14. (Copy on file in the SWCF as WPO29289.)

Chan, K.S., S.R. Bodner, A.F. Fossum, and D.E. Munson. 1995a. "Constitutive Representation of Damage Healing in WIPP Salt," *Rock Mechanics, Proceedings of the 35th U.S. Symposium, University of Nevada, Reno, NV, June 5-7, 1995*. Eds. J.J.K. Daemen and R.A. Schultz. Brookfield, VT: A.A. Balkema. 485-490. (Copy on file in the SWCF as WPO23774.)

Chan, K.S., D.E. Munson, A.F. Fossum, and S.R. Bodner. 1995b. "Inelastic Flow Behavior of Argillaceous Salt," *International Journal of Damage Mechanics*. SAND94-3017J. Albuquerque, NM: Sandia National Laboratories. (Copy on file in the SWCF as WPO22199.)

Costin, L.S., and W.R. Wawersik. 1980. *Creep Healing of Fractures in Rock Salt*. SAND80-0392. Albuquerque, NM: Sandia National Laboratories. (Copy on file in the SWCF as WPO26748.)

Dale, T., and L.D. Hurtado. 1996. "WIPP Air-Intake Shaft Disturbed-Rock Zone Study," *4th International Conference on the Mechanical Behavior of Salt, Montreal, Quebec, June 17-18, 1996*. SAND96-1327C. Albuquerque, NM: Sandia National Laboratories. (Copy on file in the SWCF.)

Davis, P.M. 1983. "Surface Deformation Associated With a Dipping Hydrofracture," *Journal of Geophysical Research*. Vol. 88, no. B7, 5826-5834. (Copy on file in the SWCF.)

DOE (U.S. Department of Energy). 1995. *Waste Isolation Pilot Plant Sealing System Design Report*. DOE/WIPP-95-3117. Carlsbad, NM: U.S. Department of Energy, Waste Isolation Pilot Plant. (Copy on file in the SWCF as WPO29062.)

Goodman, R.E. 1980. *Introduction to Rock Mechanics*. New York, NY: John Wiley & Sons. 85-88, 310-311. (Copy on file in the SWCF as microfilm NNA.910315.0132.)

Knowles, M.K., D. Borns, J. Fredrich, D. Holcomb, R. Price, D. Zeuch, T. Dale, and R.S. Van Pelt. 1996. "Testing the Disturbed Zone Around a Rigid Inclusion in Salt," *4th Conference on the Mechanical Behavior of Salt, Montreal, Quebec, June 17-18, 1996*. SAND95-1151C. Albuquerque, NM: Sandia National Laboratories. (Copy on file in the SWCF.)

Krieg, R.D. 1984. *Reference Stratigraphy and Rock Properties for the Waste Isolation Pilot Plant (WIPP) Project*. SAND83-1908. Albuquerque, NM: Sandia National Laboratories. (Copy on file in the SWCF as WPO24519.)

Ladanyi, B. 1974. "Use of the Long-Term Strength Concept in the Determination of Ground Pressure on Tunnel Linings," *Advances in Rock Mechanics, Proceedings of the Third Congress of the International Society for Rock Mechanics, Denver, CO, September 1-7, 1974*. Washington, DC: National Academy of Sciences. Vol. 2, pt. B, 1150–1156. (Copy on file in the SWCF.)

Lambe, T.W., and R.V. Whitman. 1969. *Soil Mechanics*. New York, NY: John Wiley & Sons. (Copy on file in the SNL Technical Library.)

Morgan, H.S., M. Wallner, and D.E. Munson. 1987. *Results of an International Parallel Calculations Exercise Comparing Creep Responses Predicted with Three Computer Codes for Two Excavations in Rock Salt*. SAND87-2125. Albuquerque, NM: Sandia National Laboratories. (Copy on file in the SWCF as WPO24110.)

Munson, D.E., A.F. Fossum, and P.E. Senseny. 1989. *Advances in Resolution of Discrepancies Between Predicted and Measured In Situ WIPP Room Closures*. SAND88-2948. Albuquerque, NM: Sandia National Laboratories. (Copy on file in the SWCF as WPO27882.)

Nieland, J.D. 1991. "SALT_SUBSID: A PC-Based Subsidence Model, User's Manual." Topical Report RSI-0389. Prepared for the Solution Mining Research Institute, Woodstock, IL. Rapid City, SD: RE/SPEC Inc. (Copy on file in the SWCF.)

Pfeifle, T.W., and N.S. Brodsky. 1991. *Swelling Pressure, Water Uptake, and Permeability of 70/30 Crushed Salt/Bentonite*. SAND91-7070. Albuquerque, NM: Sandia National Laboratories. (Copy on file in the SWCF as WPO25438.)

Sass, J.H., A.H. Lachenbruch, R.J. Munroe, G.W. Greene, and T.H. Moses, Jr. 1971. "Heat Flow in the Western United States," *Journal of Geophysical Research*. Vol. 76, no. 26, 6376-6413. (Copy on file in the SWCF.)

Silling, S.A. 1983. *Final Technical Position on Documentation of Computer Codes for High-Level Waste Management*. NUREG-0856. Washington, D.C.: Division of Waste Management, Office of Nuclear Material Safety and Safeguards, U.S. Nuclear Regulatory Commission. (Copy on file in the SWCF.)

Sjaardema, G.D., and R. D. Krieg. 1987. *A Constitutive Model for the Consolidation of WIPP Crushed Salt and Its Use in Analyses of Backfilled Shaft and Drift Configurations*. SAND87-1977. Albuquerque, NM: Sandia National Laboratories. (Copy on file in the SWCF as WPO27693.)

Svalstad, D.K. 1989. *Documentation of SPECTROM-41: A Finite Element Heat Transfer Analysis Program; Revision 0*. DOE/CH/10378-1, RSI-0266. Prepared by RE/SPEC Inc., Rapid City, SD. Argonne, IL: U.S. Department of Energy, Chicago Operations Office. (Copy available from National Technical Information Service, 5285 Port Royal Road, Springfield, VA, 22161, 703/487-4650. Order number: DE90000683/XAB.)

Van Sambeek, L.L. 1986. "Creep of Rock Salt Under Inhomogeneous Stress Conditions." Ph.D. dissertation. Golden, CO: Colorado School of Mines. (Dissertation available from Colorado School of Mines Library, Golden, CO.)

Van Sambeek, L.L., D.D. Luo, M.S. Lin, W. Ostrowski, and D. Oyenuga. 1993a. *Seal Design Alternatives Study*. SAND92-7340. Albuquerque, NM: Sandia National Laboratories. (Copy on file in the SWCF as WPO23445.)

Van Sambeek, L.L., J.L. Ratigan, and F.D. Hansen. 1993b. "Dilatancy of Rock Salt in Laboratory Tests," *International Journal of Rock Mechanics and Mining Sciences & Geomechanics Abstracts, Rock Mechanics in the 1990s, 34th U.S. Symposium on Rock Mechanics, University of Wisconsin, Madison, WI,* June *27-30, 1993.* Vol. 30, no. 7, 735-738. (Copy on file in the SWCF.)

Wakeley, L.D., J.J. Ernzen, B.D. Neeley, and F.D. Hansen. 1994. *Salado Mass Concrete: Mixture Development and Preliminary Characterization.* SAND93-7066. Albuquerque, NM: Sandia National Laboratories. (Copy on file in the SWCF as WPO10671.)

Yoder, E.J., and M.W. Witczak. 1975. *Principles of Pavement Design*. 2nd ed. New York, NY: John Wiley & Sons.

WIPP
UC721 Distribution List

Federal Agencies

US Department of Energy (4)
Office of Civilian Radioactive Waste Mgmt.
Attn: Deputy Director, RW-2
Acting Director, RW-10
Office of Human Resources & Admin.
Director, RW-30
Office of Program Mgmt. & Integ.
Director, RW-40
Office of Waste Accept., Stor., & Tran.
Forrestal Building
Washington, DC 20585

Attn: Project Director (2)
Yucca Mountain Site Characterization Office
Director, RW-3
Office of Quality Assurance
101 Convention Center Drive, Suite #P-110
Las Vegas, NV 89109

US Department of Energy
Albuquerque Operations Office
Attn: National Atomic Museum Library
P.O. Box 5400
Albuquerque, NM 87185-5400

US Department of Energy
Research & Waste Management Division
Attn: Director
P.O. Box E
Oak Ridge, TN 37831

US Department of Energy (8)
Carlsbad Area Office
Attn: G. Dials
D. Galbraith (3)
M. Matthews
M. McFadden
R. Lark
J. A. Mewhinney
P.O. Box 3090
Carlsbad, NM 88221-3090

US Department of Energy
Office of Environmental Restoration and Waste Management
Attn: J. Lytle, EM-30
Forrestal Building
Washington, DC 20585-0002

US Department of Energy (3)
Office of Environmental Restoration and Waste Management
Attn: M. Frei, EM-34, Trevion II
Washington, DC 20585-0002

US Department of Energy
Office of Environmental Restoration and Waste Management
Attn: S. Schneider, EM-342, Trevion II
Washington, DC 20585-0002

US Department of Energy (2)
Office of Environment, Safety & Health
Attn: C. Borgstrom, EH-25
R. Pelletier, EH-231
Washington, DC 20585

US Department of Energy (2)
Idaho Operations Office
Fuel Processing & Waste Mgmt. Division
785 DOE Place
Idaho Falls, ID 83402

US Environmental Protection Agency (2)
Radiation Protection Programs
Attn: M. Oge
ANR-460
Washington, DC 20460

Boards

Defense Nuclear Facilities Safety Board
Attn: D. Winters
625 Indiana Ave. NW, Suite 700
Washington, DC 20004

Nuclear Waste Technical Review Board (2)
Attn: Chairman
S. J. S. Parry
1100 Wilson Blvd., Suite 910
Arlington, VA 22209-2297

State Agencies

Attorney General of New Mexico
P.O. Drawer 1508
Santa Fe, NM 87504-1508

Environmental Evaluation Group (3)
Attn: Library
7007 Wyoming NE, Suite F-2
Albuquerque, NM 87109

Metropolitan Water District of Southern Calif.
Attn: J. Narvaiz
P.O. Box 54153
Los Angeles, CA 90071-3123

NM Energy, Minerals, and Natural
Resources Department
Attn: Library
2040 S. Pacheco
Santa Fe, NM 87505

NM Environment Department (3)
Secretary of the Environment
Attn: Mark Weidler
1190 St. Francis Drive
Santa Fe, NM 87503-0968

NM Bureau of Mines & Mineral Resources
Socorro, NM 87801

NM Environment Department
WIPP Project Site
Attn: P. McCasland
P.O. Box 3090
Carlsbad, NM 88221

Laboratories/Corporations

Battelle Pacific Northwest Laboratories (2)
Attn: R. E. Westerman
R. Romine, MS P8-38
P.O. Box 999
900 Battelle Blvd.
Richland, WA 99352

Brookhaven National Laboratory
Attn: P. D. Moskowitz
Environmental & Waste Technology
Center
Building 830
Upton, NY 11973

Harnischfeger Corp.
Phonex Engineering Services
Attn: R. Luebke
2969 S. Chase Avenue
Milwaukee, WI 53207-6408

Ian Clelland
6656 N. Amdahl Dr.
Tucson, AZ 85704

INTERA, Inc.
Attn: G. A. Freeze
1650 University Blvd. NE, Suite 300
Albuquerque, NM 87102

INTERA, Inc. (6)
Attn: J. F. Pickens
V. Kelley
M. Reeves
W. Statham
J. Beach
D. Fryar
INTERA WIPP Library
6850 Austin Center Blvd., Suite 300
Austin, TX 78731

INTERA, Inc.
Attn: J. Lee, YMP PA Dept.
1261 Town Center Drive
Las Vegas, NV 89134

INTERA, Inc.
Attn: W. Stensrud
P.O. Box 2123
Carlsbad, NM 88221

Istasca Consulting Group, Inc.
Attn: John Tinucci
Thresher Square East
708 South Third Street, Suite 310
Minneapolis, MI 55415

Los Alamos National Laboratory
Attn: B. Erdal, INC-12
P.O. Box 1663
Los Alamos, NM 87544

Morton International, Morton Salt
Attn: H. W. Diamond
Morton International Building
100 N. Riverside Plaza,
Randolph Street at the River
Chicago, IL 60606-1597

Parsons Brinckerhoff Energy Services, Inc.
Attn: W. S. Roman
One Penn Plaza
New York, NY 10119

Parsons Brinckerhoff Energy Services, Inc. (2)
Attn: B. W. Lawerance
C. D. Mann
M. S. Lin
303 Second Street
Suite 850 North
San Francisco, CA 94107

Parsons Brinckerhoff International, Inc.
Attn: Mary Ann Novak
700 11th Street, NW, Suite 710
Washington, DC 20001

Phillips Mining, Geotechnical & Grouting
Attn: Stephen Phillips
8640 North Glenhurst Place
Tucson, AZ 85704

RE/SPEC, Inc. (5)
Attn: L. Van Sambeek (3)
G. Callahan
M. Loken
J. Ratigan
T. Pfeifle
3824 Jet Drive
P.O. Box 725
Rapid City, SD 57709

RE/SPEC, Inc
Attn: Angus Robb
4775 Indian School NE, Suite 300
Albuquerque, NM 87110-3927

Science Applications International Corp.
Attn: W. Thompson
15000 W. 6th Avenue, Suite 202
Golden, CO 80401

Tech Reps, Inc. (3)
Attn: J. Chapman (1)
L. Robledo (2)
5000 Marble NE, Suite 222
Albuquerque, NM 87110

Westinghouse Electric Corporation (5)
Attn: Library
J. Epstein
J. Lee
B. A. Howard
R. Kehrman
P.O. Box 2078
Carlsbad, NM 88221

S. Cohen & Associates
Attn: Bill Thurber
1355 Beverly Road
McLean, VA 22101

National Academy of Sciences, WIPP Panel

Howard Adler
Oxyrase, Incorporated
7327 Oak Ridge Highway
Knoxville, TN 37931

Bob Andrews
Board of Radioactive Waste Management
GF456
2101 Constitution Ave.
Washington, DC 20418

Rodney C. Ewing
Department of Geology
University of New Mexico
Albuquerque, NM 87131

Charles Fairhurst
Department of Civil
and Mineral Engineering
University of Minnesota
500 Pillsbury Dr. SE
Minneapolis, MN 55455-0220

B. John Garrick
PLG Incorporated
4590 MacArthur Blvd., Suite 400
Newport Beach, CA 92660-2027

Leonard F. Konikow
US Geological Survey
431 National Center
Reston, VA 22092

Carl A. Anderson, Director
Board of Radioactive Waste Management
National Research Council
HA 456
2101 Constitution Ave. NW
Washington, DC 20418

Christopher G. Whipple
ICF Kaiser Engineers
1800 Harrison St., 7th Floor
Oakland, CA 94612-3430

John O. Blomeke
720 Clubhouse Way
Knoxville, TN 37909

Sue B. Clark
University of Georgia
Savannah River Ecology Lab
P.O. Drawer E
Aiken, SC 29802

Konrad B. Krauskopf
Department of Geology
Stanford University
Stanford, CA 94305-2115

Della Roy
Pennsylvania State University
217 Materials Research Lab
Hastings Road
University Park, PA 16802

David A. Waite
CH_2 M Hill
P.O. Box 91500
Bellevue, WA 98009-2050

Thomas A. Zordon
Zordan Associates, Inc.
3807 Edinburg Drive
Murrysville, PA 15668

Universities

Harvey Mudd College
Attn: M. Cardenas
Department of Engineering
Claremont, CA 91711

New Mexico State University
Waste-management Education & Research Corporation.
Attn: R. Bhada
P.O. Box 3001
Las Cruces, NM 88003-8001

University of California
Department of Mechanical and Environmental Engineering
Attn: E. Marschall
University of California
Santa Barbara, CA 93106

University of Nevada-Reno
Department of Mining Engineering
Mackay School of Mines
Attn: J. Daamen
Reno, NV 89557

University of New Mexico
Center for Radioactive Waste Management
Attn: W. Lutze
209 Faris Engineering Building
Albuquerque, NM 87131-1341

University of New Mexico
Department of Civil Engineering
Attn: J. C. Stormont
Albuquerque, NM 87131-1351

University of New Mexico
Geology Department
Attn: Library
141 Northrop Hall
Albuquerque, NM 87131

University of Washington
College of Ocean & Fishery Sciences
Attn: G. R. Heath
583 Henderson Hall, HN-15
Seattle, WA 98195

Libraries

Thomas Brannigan Library
Attn: D. Dresp
106 W. Hadley St.
Las Cruces, NM 88001

Government Publications Department
Zimmerman Library
University of New Mexico
Albuquerque, NM 87131

New Mexico Junior College
Pannell Library
Attn: R. Hill
Lovington Highway
Hobbs, NM 88240

New Mexico State Library
Attn: N. McCallan
325 Don Gaspar
Santa Fe, NM 87503

New Mexico Tech
Martin Speere Memorial Library
Campus Street
Socorro, NM 87810

WIPP Public Reading Room
Carlsbad Public Library
101 S. Halagueno St.
Carlsbad, NM 88220

Foreign Addresses

Atomic Energy Canada Ltd. (5)
Whiteshell Laboratory
Attn: Neil Chandler
Glenn McCrank
B. Goodwin
Malcolm Gray
Maria Onefrei
Pinawa Manitoba, CANADA ROE 1L0

Francois Chenevier (2)
ANDRA
Route de Panorama Robert Schumann
B. P. 38
92266 Fontenay-aux-Roses, Cedex
FRANCE

Claude Sombret
Centre d'Etudes Nucleaires
de la Vallee Rhone
CEN/VALRHO
S.D.H.A. B.P. 171
30205 Bagnols-Sur-Ceze, FRANCE

Commissariat a L'Energie Atomique
Attn: D. Alexandre
Centre d'Etudes de Cadarache
13108 Saint Paul Lez Durance Cedex
FRANCE

Bundesanstalt fur Geowissenschaften und
Rohstoffe (2)
Attn: M. Langer
M. Wallner
Postfach 510 153
D-30631 Hannover, GERMANY

Bundesministerium fur Forschung und
Technologie
Postfach 200 706
5300 Bonn 2, GERMANY

Forschungszentrum Karlsruhe GmbH
Institut für Nukleare Entsorgungstechnik
Attn: E. Korthaus
Postfach 3640, D-76021 Karlsruhe
Bundesrepublic Deutchland
GERMANY

Gesellschaft fur Anlagen und Reaktorsicherheit
(GRS)
Attn: B. Baltes
Schwertnergasse 1
D-50667 Cologne, GERMANY

Grundbau Und Felsbau GmbH
Attn: W. Wittke
Henricistraße 50
52072 Aachen, GERMANY

Institut Für Gebirgsmechanik
Attn: W. Minkley
Friederikenstraße 60
04279 Leipzig, GERMANY

Institut Für Tieflagerung
Attn: K. Kuhn
Theodor-Heuss-Strasse 4
D-3300 Braunschweig, GERMANY
Shingo Tashiro
Japan Atomic Energy Research Institute
Tokai-Mura, Ibaraki-Ken, 319-11
JAPAN

Netherlands Energy Research Foundation ECN
Attn: J. Prij
3 Westerduinweg
P.O. Box 1
1755 ZG Petten
THE NETHERLANDS

Universiteit Utrecht
Department of Geology (HPT-lab)
Attn: C. J. Spiers
PO Box 80021
NL-3508 TA Utrech
Budapestlaan 4
THE NETHERLANDS

Svensk Karnbransleforsorjning AB
Attn: F. Karlsson
Project KBS (Karnbranslesakerhet)
Box 5864
S-102 48 Stockholm
SWEDEN

Nationale Genossenschaft fur die Lagerung
Radioaktiver Abfalle (2)
Attn: S. Vomvoris
P. Zuidema
Hardstrasse 73
CH-5430 Wettingen
SWITZERLAND

AEA Technology
Attn: J. H. Rees
D5W/29 Culham Laboratory
Abington, Oxfordshire OX14 3DB
UNITED KINGDOM

AEA Technology
Attn: W. R. Rodwell
044/A31 Winfrith Technical Centre
Dorchester, Dorset DT2 8DH
UNITED KINGDOM

AEA Technology
Attn: J. E. Tinson
B4244 Harwell Laboratory
Didcot, Oxfordshire OX11 ORA
UNITED KINGDOM

Internal

MS	Org.	
0483	5165	R. E. Stinebaugh
0706	6113	J. K. Linn
1320	6719	E. J. Nowak
1322	6121	J. R. Tillerson (10)
1322	6121	E. H. Ahrens (2)
1322	6121	A. W. Dennis (10)
1322	6121	F. D. Hansen
1322	6121	L. D. Hurtado
1322	6121	M. K. Knowles
1324	6115	P. B. Davies
1325	6852	L. S. Costin
1325	6852	R. E. Finley
1328	6749	D. R. Anderson
1328	6741	H. N. Jow
1328	6849	M. F. Fewell
1328	6849	P. Vaughn
1335	6705	M. Chu
1341	6748	J. T. Holmes
1395	6800	L. Shephard
1395	6707	M. Marietta
1395	6841	V. H. Slaboszewicz
1330	6752	B. J. Pierson (2)
1330	6752	NWM Library (100)
9018	8523-2	Central Technical Files
0899	4414	Technical Library (5)
0619	12630	Review and Approval Desk, For DOE/OSTI (2)